Lawrence Berkeley National Laboratory
Recent Work

Title
ATOMIC STRUCTURE OF THE SILICON/SILICON DIOXIDE INTERFACE

Permalink
https://escholarship.org/uc/item/2x61c2zd

Author
Mazur, J.H.

Publication Date
1985-12-01

eScholarship.org Powered by the California Digital Library
University of California

LBL-20161
c.2

# Lawrence Berkeley Laboratory

UNIVERSITY OF CALIFORNIA

RECEIVED
LAWRENCE
BERKELEY LABORATORY

AUG 12 1986

LIBRARY AND
DOCUMENTS SECTION

## Materials & Molecular Research Division

# ATOMIC STRUCTURE OF THE SILICON/SILICON DIOXIDE INTERFACE

J.H. Mazur
(Ph.D. Thesis)

December 1985

TWO-WEEK LOAN COPY

*This is a Library Circulating Copy which may be borrowed for two weeks.*

Prepared for the U.S. Department of Energy under Contract DE-AC03-76SF00098

LBL-20161
c.2

**DISCLAIMER**

This document was prepared as an account of work sponsored by the United States Government. While this document is believed to contain correct information, neither the United States Government nor any agency thereof, nor the Regents of the University of California, nor any of their employees, makes any warranty, express or implied, or assumes any legal responsibility for the accuracy, completeness, or usefulness of any information, apparatus, product, or process disclosed, or represents that its use would not infringe privately owned rights. Reference herein to any specific commercial product, process, or service by its trade name, trademark, manufacturer, or otherwise, does not necessarily constitute or imply its endorsement, recommendation, or favoring by the United States Government or any agency thereof, or the Regents of the University of California. The views and opinions of authors expressed herein do not necessarily state or reflect those of the United States Government or any agency thereof or the Regents of the University of California.

# ATOMIC STRUCTURE OF THE SILICON/SILICON DIOXIDE INTERFACE

Jerzy Henryk Mazur

Materials and Molecular Research Division
Lawrence Berkeley Laboratory
and
Department of Materials Science
and Mineral Engineering
University of California
Berkeley, CA 94720

This work was supported by the Director, Office of Energy Research, Office of Basic Energy Science, Materials Science Division of the U.S. Department of Energy under Contract No. DE-AC03-76SF00098.

TABLE OF CONTENTS

Page

Preface . . . . . . . . . . . . . . . . . . . . . . . . . . . vii

Abstract. . . . . . . . . . . . . . . . . . . . . . . . . . . ix

1. Introduction. . . . . . . . . . . . . . . . . . . . . . . . 1

1.1 The Technological Importance of the Si-$SiO_2$ System . . . 1

References - Chapter 1. . . . . . . . . . . . . . . . . . . . 6

2. The Structure of $SiO_2$ . . . . . . . . . . . . . . . . . . 8

2.1 Phases of Silica . . . . . . . . . . . . . . . . . . . . 8

2.2 Models of Amorphous $SiO_2$ . . . . . . . . . . . . . . . . 17

References - Chapter 2. . . . . . . . . . . . . . . . . . . . 20

3. Models of the Si-$SiO_2$ Interface . . . . . . . . . . . . . . 23

3.1 Models of the Si-$SiO_2$ Interface Derived from XPS Studies . . . . . . . . . . . . . . . . . . 23

3.2 Models of the Si-$SiO_2$ Interface Derived from RBS-Ion Channeling Studies. . . . . . . . . . . . 27

3.3 Models of the Si-$SiO_2$ Interface Derived on the Basis of EPR Studies. . . . . . . . . . . . . . 29

3.4 Models of the Si-$SiO_2$ Region Derived from Ellipsometry Experiments . . . . . . . . . . . . . . . 33

3.5 Auger Electron Spectroscopy Studies of the Si-$SiO_2$ Interface. . . . . . . . . . . . . . . . . . . 35

3.6 The Structure of the Si-$SiO_2$ Interface as Determined from Low Energy Electron Diffraction, and the Surface Charge Mobility at High Inversion. . . . . . . 36

References - Chapter 3. . . . . . . . . . . . . . . . . . . . 38

Page

4. Experimental Techniques . . . . . . . . . . . . . . . . . . . . . 45

4.1 Transmission Electron Microscopy . . . . . . . . . . . . . 45

4.2 TEM Image Formation. . . . . . . . . . . . . . . . . . . . 45

4.3 The Relationship Between the High Resolution Image and the Specimen Structure . . . . . . . . . . . 48

4.4 Optical Diffraction. . . . . . . . . . . . . . . . . . . . 58

References - Chapter 4. . . . . . . . . . . . . . . . . . . . 60

5. Material. . . . . . . . . . . . . . . . . . . . . . . . . . . 62

5.1 Choice of Material . . . . . . . . . . . . . . . . . . . . 62

5.2 Wafer Cleaning Procedures and Oxidation. . . . . . . . . 62

5.3 TEM Specimen Preparation . . . . . . . . . . . . . . . . . 64

6. The Atomic Structure of Si-$SiO_2$ Interfaces: Results and Interpretation. . . . . . . . . . . . . . . . . . . . 67

6.1 Oxidation of Singular (111) Si Surfaces. . . . . . . . . 71

6.2 Oxidation of Vicinal (111)2°[$11\bar{2}$] Si Surfaces. . . . . . 79

6.3 Oxidation of Vicinal (111)3°[$1\bar{1}0$] Si Surfaces. . . . . . 81

6.4 Oxidation of Exact (100) and Vicinal (100)2°[011] Si Surfaces . . . . . . . . . . . . . . . 90

6.4.1 Oxidation of (100) Si Surfaces at Room Temperatures: Native Oxide on (100) Oxide Surfaces. . . . . . . . . . . . . . . . . 90

6.4.2 Oxidation of Exact (100) Si Surfaces. . . . . . . 94

6.4.3 Oxidation of (100)2°[011] Si Surfaces . . . . . . 97

6.5 Summary of Experimental Results. . . . . . . . . . . . . 101

References - Chapter 6. . . . . . . . . . . . . . . . . . . . 103

Page

7. The Proposed Model of Atomic Structure of the Silicon-Silicon Dioxide Interface . . . . . . . . . . . . . . . 105

7.1 Modeling the $SiO_2$ Network Topology Near the Interface. . . . . . . . . . . . . . . . . . . . . . . 105

7.1.1 Topology of the First Monolayer of the $Si-SiO_2$ Network Near the {111} $Si-SiO_2$ Interface . . . . . . . . . . . . . . . . . . . . 105

7.1.2 Topology of the First Monolayer of the $Si-SiO_2$ Network Near the {100} $Si-SiO_2$ Interface . . . . . . . . . . . . . . . . . . . . 110

7.2 The Consistency of the Proposed Atomistic Modes of the $Si-SiO_2$ Interfaces with Other Experimental Observations . . . . . . . . . . . . . . . . . . . . . . . 123

References - Chapter 7. . . . . . . . . . . . . . . . . . . . . . 126

8. Conclusions and Suggestions for Future Work . . . . . . . . . 127

8.1 Conclusions. . . . . . . . . . . . . . . . . . . . . . . . 127

8.2 Future Work. . . . . . . . . . . . . . . . . . . . . . . . 132

Acknowledgments . . . . . . . . . . . . . . . . . . . . . . . . . 134

# PREFACE

The objectives of this work are to establish a model of the atomic structure of the silicon-silicon dioxide interface using a direct imaging technique of high-resolution electron microscopy (HREM), and to determine the oxidation mechanism from the silicon-silicon dioxide interface morphology. The thesis is organized into eight chapters.

Chapter 1 introduces the subject of the Si-$SiO_2$ interface by stressing the importance of the Si-$SiO_2$ system in the fabrication of electronic devices and by discussing the orientation and, therefore, structure-related properties of the Si-$SiO_2$ system. In the second chapter the structure of the $SiO_2$ phases is described. This description is followed in Chapter 3 by a review of the models of the structure and chemistry of the Si-$SiO_2$ interface obtained from different techniques. Chapters 4 and 5 describe experimental techniques and procedures used in this research. The results of the experiments and their interpretations are described in Chapter 6. Chapter 7 relates this model to those discussed in Chapter 3. Chapter 8 contains the conclusions of this thesis and suggestions for further work.

# ATOMIC STRUCTURE OF THE SILICON/SILICON DIOXIDE INTERFACE

Jerzy Henryk Mazur

Materials and Molecular Research Division
Lawrence Berkeley Laboratory
and
Department of Materials Science
and Mineral Engineering
University of California
Berkeley, CA 94720

## Abstract

The atomic structure of the Si-$SiO_2$ interfaces obtained by thermal oxidation of singular and vicinal surfaces of silicon in dry $O_2$ at temperatures above 960°C has been studied in cross-section by high resolution electron microscopy (HREM). The interface between the silicon substrate and amorphous $SiO_2$ was very abrupt and flat over the entire area observed. Detailed analysis of oxidized singular (111) Si surfaces revealed the existence of steps one {111} interplanar distance (0.314 nm) high. The width of the terraces between positive and negative steps varied and was dependent upon defocus which indicates that these steps probably did not extend through the whole TEM specimen thickness (less than 20 nm). Dry oxidation of vicinal (111) 3° $[1\bar{1}0]$ Si surfaces resulted in an interface which can be described by atomically flat terraces about 6 nm wide with ledges 0.314 nm high, and all of the same sign. For less inclined vicinal (111) 2° $[11\bar{2}]$ Si surfaces ledges of both signs were observed. The observations of the Si-$SiO_2$ interface structure resulting from oxidation of exact (100) and (100) 2° [011] Si surfaces at the present level of resolution can be interpreted in terms of (100) terraces

separated by ledges up to about one Si unit cell high, or alternatively as small {111} facets protruding into the $SiO_2$ (this could suggest that the {100} Si-$SiO_2$ interface is non-singular). These observations suggest a terrace-ledge-kink model for the Si-$SiO_2$ interface structure and a ledge mechanism for high temperature oxidation similar to that for evaporation.

The structure of the Si-$SiO_2$ interface suggests a very abrupt Si crystal to amorphous $SiO_2$ transition but requires the existence of Si atoms in incompletely oxidized states $Si^{1+}$, $Si^{2+}$, $Si^{3+}$ (bonded to 1, 2, 3 oxygen atoms) at oxidized Si surfaces for all orientations, in agreement with XPS results. Constructed atomistic models of the interfaces suggest that ratios of the $Si^{1+}$:$Si^{2+}$:$Si^{3+}$ can vary depending on details of interface morphology for a given Si substrate orientation, and therefore might be affected by the oxidation kinetics. In this model, dangling bonds normal to (111) terraces are present on singular and vicinal (111) surfaces. The dangling bonds on a (100) substrate are located in a different "topological" environment corresponding to models of $P_{b0}$ and $P_{b1}$ EPR centers.

It is suggested that further studies of silicon oxidation combining HREM, XPS and EPR performed on the same specimen could more narrowly restrict the number of possible atomistic models of Si-$SiO_2$ interfaces.

# 1. INTRODUCTION

## 1.1 The Technological Importance of the Si-$SiO_2$ System

Thermally-grown $SiO_2$ films on silicon are the subject of considerable interest because of their application in the production of bipolar and metal-oxide-semiconductor (MOS) electronic devices [1.1-1.10]. These $SiO_2$ films are used to passivate active device regions and junctions, to insulate field regions and to provide isolation between active components. However, the most important application of thermally-grown $SiO_2$ is as a gate dielectric in MOS devices. Some of these functions of thermally-grown $SiO_2$ on Si are schematically illustrated in Fig. 1.1, which shows two complementary MOS electronic devices. Thermally-grown oxides are also used during processing as a barrier against dopant diffusion.

This variety of applications results from very good stability of the thermally-grown $SiO_2$ on Si, its good adhesion to the Si substrate and very good electronic properties: high breakdown voltage and low density of electronic defects in the oxide and at the Si-$SiO_2$ interface. These electronic defects (mobile ionic charges, oxide trapped charges, oxide fixed charges, interface trapped charges and interface states) are located in the bulk oxide or near the Si-$SiO_2$ interface as is shown in Fig. 1.2.

The oxide fixed charges and interface states are inherent to the oxidation process and cannot be eliminated by any known process. These defects, located in the interface transition layer of $SiO_x$ which is about 50 Å thick (Fig. 1.2), and at the interface, e.g.

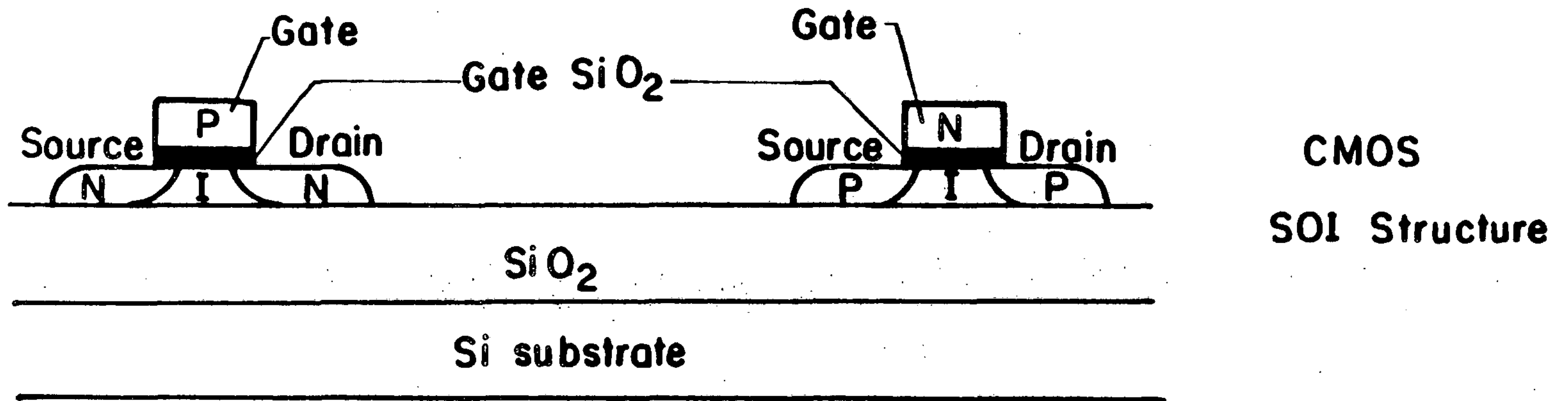


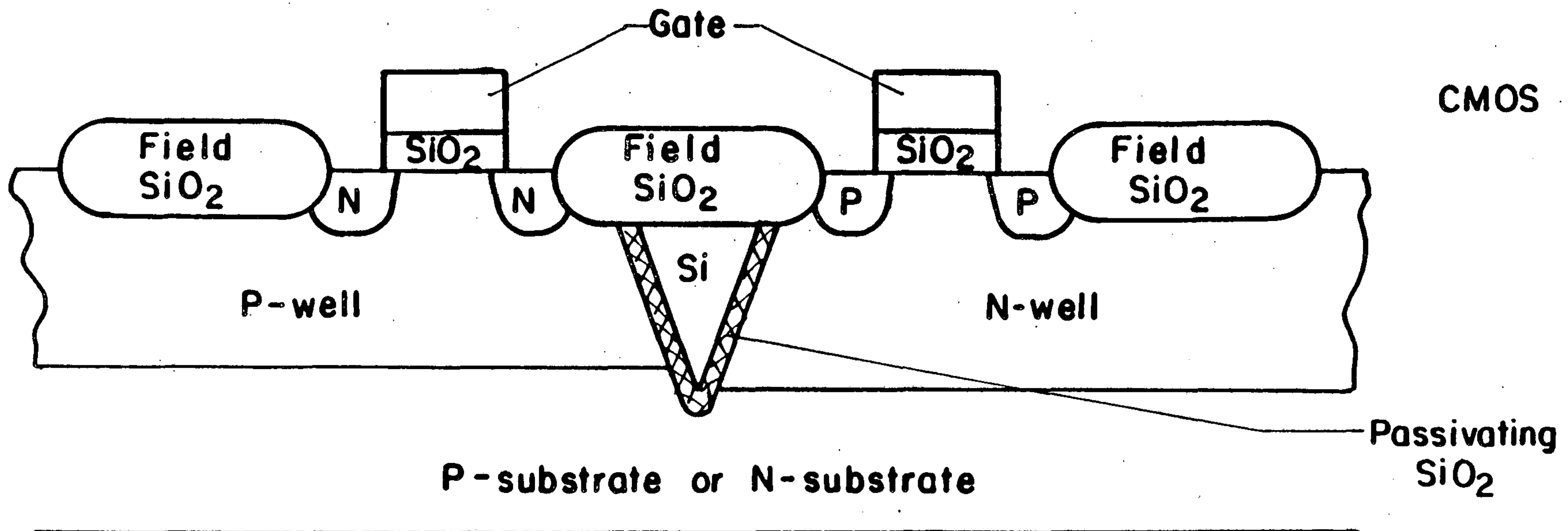


XBL 8411-6093

Fig. 1.1. Some of the functions that thermal $SiO_2$ films perform in contemporary MOS devices: gate oxides, passivating oxides, field oxides, insulators in semiconductor on insulator (SOI) structures.

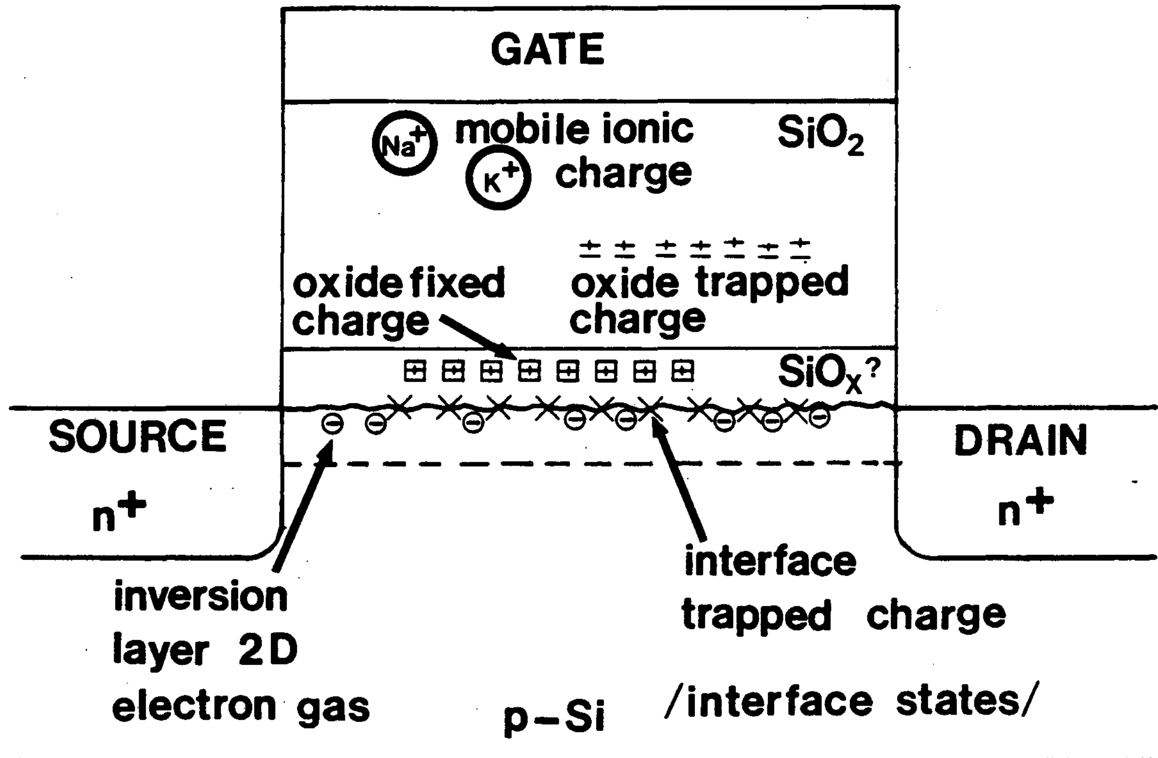


XBL 859-3823

Fig. 1.2. Location of charges in a MOS structure: oxide fixed charges and interface trapped charges and states are inherent to the oxidation mechanism, whereas mobile ionic charges ($Na^+$, $K^+$ $Li^+$ and possibly $H^+$) and oxide fixed charges can be avoided to a large extent by elimination of contamination and radiation sources. Density of charges in the Si surface layer is controlled by the Si surface potential, while the mobility of 2D electron (hole) gas in strong inversion depends on the surface roughness.

oxide fixed charges and charges trapped on the interface traps (states), influence the operation of MOS electronic devices because they can interact with the mobile charges in the inversion layer. The density of the oxide fixed charges and interfacial states is smaller for {100} than {111} Si substrates oxidized under the same conditions. The nature of the oxide fixed charges is still not completely understood. Their origin has been associated with the excess of Si in the "nonstoichiometric" region near the interface [1.11], or with positively charged oxygen vacancies [$SiO_3$] in $SiO_2$ [1.12]. The positively charged vacancy model is supported by studies [1.13] which show that annealing at low oxygen partial pressure results in an increased density of the oxide charges.

Another type of electronic defect is interface traps. These are electronic energy levels (or states) located at the interface and they are frequently associated with incomplete bonding structures, impurities and various bond-breaking processes. These states can trap or release electrons and holes from the Si surface layer depending upon the Si surface potential (resulting in interface trapped charges as shown in Fig. 1.2). The intrinsic states are those which are thought to originate from structural defects inherent in the interface region of $SiO_x$ between amorphous $SiO_2$ and crystalline Si but not impurities. They are dependent on orientation, heat treatment temperature and atmosphere in a different way from oxide fixed charges. In particular, interface trapped charge density can be greatly reduced by low temperature (<500°C) hydrogen annealing. The density of these interface

states in the Si-$SiO_2$ interface region depends on the Si surface orientation.

For high gate fields resulting in the formation of an inversion layer (e.g. a channel near the Si-$SiO_2$ interface containing the bulk minority charges as a dominant charge species) the surface mobility is diminished by the scattering of carriers which results from the variation in surface potential associated with surface roughness [1.14-1.20]. Lower mobility results in a slower operation speed of electronic devices.

The mobile charges are associated with contamination during processing while oxide trapped charges are associated mainly with exposure to different forms of radiations. Both types of charges can be greatly reduced by prudent processing practices.

The detrimental effects of oxidation-induced electronic defects at the Si-$SiO_2$ interface and the interface morphology increase as the lateral dimensions of the electronic devices are reduced (i.e., in very large scale integration technology) from a few μm to a few hundreds of nm. This imposes vertical reduction of the oxide thickness. For lateral device dimensions of 100 nm, for example, the thickness of the gate oxides is expected to be about 4 nm [1.21]. Such dimensions require very strict control of the oxide thickness and uniformity.

## REFERENCES - CHAPTER 1


1.1 S.M. Sze, "Physics of Semiconductor Devices," 2nd edition, J. Wiley & Sons, New York, 1981.

1.2 S.M. Sze, Ed., "VLSI Technology," McGraw-Hill Book Company, New York, 1983.

1.3 E.H. Nicollian, J.R. Brews, "MOS (Metal-Oxide-Semiconductor) Physics and Technology," J. Wiley & Sons, New York, 1982.

1.4 R.A. Colclaser, "Microelectronics: Processing and Device Design," J. Wiley & Sons, New York, 1980.

1.5 R.S. Muller, T.I. Kamins, "Device Electronics for Integrated Circuits," J. Wiley & Sons, New York, 1977.

1.6 A.S. Grove, "Physics and Technology of Semiconductor Devices," J. Wiley & Sons, New York, 1967.

1.7 J.D. Meindel, et al., "Computer-Aided Engineering of Semiconductor Integrated Circuits," Integrated Circuits Laboratory, Stanford University, Report TRDXG501 ICL 17-78 (1980).

1.8 J.D. Plummer, et al., "Computer-Aided Design of Integrated Circuit Fabrication Processes for VLSI Devices," Integrated Circuits Laboratory, Stanford University, Report TRDXG501-81 ICL 17-79 (1981).

1.9 J.D. Plummer, et al., "Computer-Aided Design of Integrated Circuit Fabrication Processes for VLSI Devices," Integrated Circuits Laboratory, Stanford University, Report TRDXG501-82 ICL 17-79 (1982).

1.10 J.D. Plummer, et al., "Computer-Aided Design of Integrated Circuit Fabrication Processes for VLSI Devices," Integrated Circuits Laboratory, Stanford University, Report TRDXG501-83 ICL 17-79 (1983).

1.11 B.E. Deal, M. Sklar, A.S. Grove, E.H. Snow, J. Electrochem. Soc., 114, 266 (1967).

1.12 R.B. Laughlin, J.D. Joannopoulos, D.J. Chadi, in: "The Physics of $SiO_2$ and Its Interfaces," S.T. Pantelides, Ed., Pergamon Press, New York, 1978, p. 321.

1.13 F.M. Fowkes, D.W. Hess, Appl. Phys. Lett. 22, 377 (1973).

1.14 Y.C. Cheng, E.A. Sullivan, Surface Sci. 34, 717 (1973).

1.15 Y.C. Cheng, E.A. Sullivan, J. Appl. Phys. 44, 923 (1973).

1.16 Y.C. Cheng, Japan. J. Appl. Phys. Suppl. 2, Pt. 2, p. 363 (1974).

1.17 C.T. Sah, T.H. Ning, L.L. Tschopp, Surf. Sci. 32, 561 (1972).

1.18 S.C. Sun, J.D. Plummer, IEEE J. Solid-State Circuits, SC-12, 562 (1980).

1.19 S.M. Goodnick, R.G. Gann, D.K. Ferry, C.W. Wilmsen, O.L. Krivanek, Surf. Sci. 113, 233 (1982).

1.20 S.M. Goodnick, R.G. Gann, J.R. Sites, D.K. Ferry, C.W. Wilmsen, D. Fathy, O.L. Krivanek, J. Vac. Sci. Technol. B1, 803 (1983).

1.21 P. Solomon in "Physics of VLSI," AIP Conference Proceedings No. 122, J. Knights, Ed. (1984).

# 2. THE STRUCTURE OF $SiO_2$

## 2.1 Phases of Silica

Unlike silicon (space group F d3m) which is observed in only the diamond cubic form with lattice parameter $a_o = 5.428Å$, $SiO_2$ exists in many structural forms (polymorphs). Obviously at a fixed temperature and pressure only one $SiO_2$ polymorph can be thermodynamically stable. The pressure-temperature phase diagram [2.1.1] shown in Fig. 2.1.1 indicates stability ranges of different phases of silica, while Table I gives their structural parameters and some other physical properties. Co-existence of different polymorphs outside their stability limits results from some particularly sluggish polymorphic transformations [2.1.2]. The rate of these transformations can be inhibited by certain impurity atoms acting as stabilizers. In addition, certain cations listed in Table II are known to be catalysts for the formation of specific $SiO_2$ phases. Silica has crystalline as well as amorphous/vitreous (glass) polymorphs. The differences in the free energy of formation of different crystalline and amorphous polymorphs are very small [2.1.3] over a large range of temperatures (Fig. 2.1.2).

X-ray diffraction analysis of different polymorphs has determined that the basic structural unit of $SiO_2$ consists of [$SiO_4$] tetrahedra (shown in Fig. 2.1.3) of approximately the same size (Table I), with 4:2 coordination (each Si has four O nearest neighbors while each O has two Si nearest neighbors) with the only exception being the 6:3 coordination of stishovite. Silica can be thought of as a crystalline

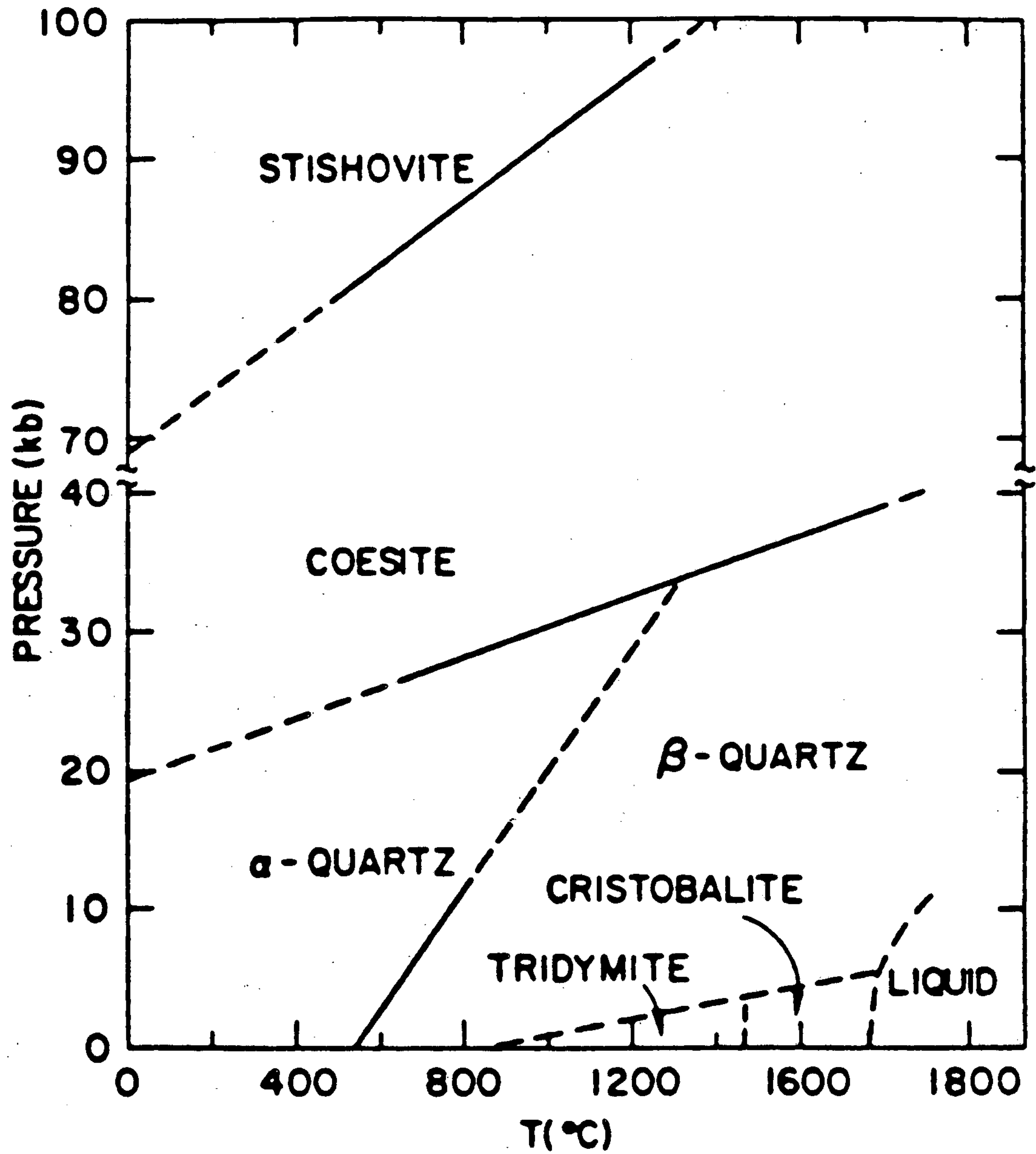


XBL 858-3557

Fig. 2.1.1. Stability ranges of different polymorphs of $SiO_2$ (from [2.1.1]).

Table I. Material parameters of the various forms of $SiO_2$ ($Z_c$ coordination number, N-number of $|SiO_4|$ tetrahedra in the ring, $T_{\alpha\to\beta}$ transisition temperature from one to another phase, $\rho$ density, $d_{Si-O}$ bond length, $d_{O-O}$ oxygen-oxygen distance, $\phi$ Si-O-Si bond angle, n refractive index, $\epsilon_1(0)$ electronic dielectric constant, $E_g$ energy gap, $H_f$ enthalpy of formation). From 1, 2, 3, 4, 5, 6 and references therein.

| Allotropic Form | Space Group† | Symmetry*/ Occurrence Frequency** | $Z_c$ (N) | $T_{\alpha\to\beta}$ (°C) | $\rho$ (g/cm³) | Lattice Parameter (Å) | c/a | $d_{Si-O}$ (Å) | $d_{O-O}$ | $\phi$ | n | $\epsilon_1(0)$ | $E_g$ (ev) | $H_f$ (298°K) (kcal/mole) |
|---|---|---|---|---|---|---|---|---|---|---|---|---|---|---|
| α-quartz | P3₂21(L)<br>P3₁21(R) | hex (c) | 4(6) | ≧ 573 | 2.65 | a = 4.9138<br>c = 5.4052<br>(T = 25°C) | 1.100 | 1.60 to 1.61 | 2.60 to 2.67 | 144° | 1.549 | 2.40 | 9.0 | 217.7 |
| β-quartz | P6₂22(L)<br>P6₄22(R) | hex (c) | 4(6) | — | 2.49 | a = 5.038<br>c = 5.460<br>(T = 600°C) | 1.084 | 1.63 | 2.60 | 144° ? | 1.530 | 2.34 | — | — |
| α-cristobalite | P4₁2₁(L)<br>P4₃2₁(R) | tetr (c) | 4(6) | ≦ 270 | 2.33 | a = 4.971<br>c = 6.918<br>(T = 25°C) | 1.392 | 1.59 ?<br>(1.60 to 1.61) | 2.58 to 2.63 | 147° | 1.487 | 2.21 | — | 217.1 |
| β-cristobalite | Fd3m | cub (c) | 4(6) | — | 2.2 | a = 7.1297<br>(T = 300°C) | — | 1.55 | 2.53 | <148°> | 1.473 | 2.17 | — | 216.417 |
| coesite | C 2/C | mon (r)<br>(hex) | (7,8,9)<br>4(4)<br>(4-6-8-9) | — | 3.01<br>(2.91)<br>(2.87 natural) | a = 7.173<br>b = 12.328<br>c = 7.175<br>β = 120°<br>(T = 20°C) | (1.393) | 1.60 to 1.63 | 2.60 to 2.67 | 120°<br>(139°) | 1.600 | 2.56 | 8.9 | — |
| keatite | P4₁2₁2(L)<br>P4₃2₁2(R) | tetr (r) | 4(5,7,8) | — | 2.50 | a = 7.46<br>c = 8.61<br>(T = 20°C) | 1.154 | 1.57 to 1.61 | — | — | 1.519<br>(1.513) | 2.31<br>(2.29) | — | — |
| stishovite | P4₂/mnm | tetr (r) | 6 | — | 4.35<br>(4.28)<br>(4.03 natural) | a = 4.1790<br>c = 2.6649<br>(T = 20°C) | 0.638 | 1.77 ? | — | — | 1.830 | 3.35 | 8.4 | — |
| vitreous silica | — | amor (c) | 4<br>(3 to 9) | — | 2.20 | — | — | 1.61 ?<br>(1.60) | 2.63 ? | <144°> | <1.464> | <2.14> | ~9.0 | — |
| melanophlogite | — | cub (r) | 4 | — | ≈2.05<br>(1.99) | a = 13.402 | — | — | — | — | 1.425 | 2.03 | — | — |
| fibrous silica | — | orth (r) | 4 ? | — | 1.96 to 1.98 | a = 4.72<br>b = 8.36<br>c = 5.16<br>(T = 20°C) | — | — | — | — | — | — | — | — |
| silica film | — | hex (r) | 4 | — | — | a = 5.07<br>c = ?<br>(T = 20°C) | — | — | — | — | — | — | — | — |
| $SiO_x$ | — | amor (c)<br>cub (r)<br>(x = 1) | 4 ?<br>4 ? | — | 2.13<br>(2.14) | a = 5.16<br>(T = 20°C) | — | — | — | — | n(x):<br>1.90 to 1.94 | $\epsilon_1$(x):<br>3.61 to 3.76 | — | — |

*hex: hexagonal, mon: monoclinic, orth: orthorhombic, tetr: tetragonal, cub: cubic, amor: amorphous.

**c: common form, r: rare form.

†(L), (R) indicates left or right enantiomorph of $SiO_2$.


References:

1. Landolt-Börstein, Neue Serie, ed. K.-H Hellwege, vol. 7, Springer-Verlag, Berlin/Heidelberg/New York 1975 p. 255
2. S.T. Pantelides, W.A. Harrison, Phys. Rev. B. *13*, 2667 (1976)
3. K. Hübner, Phys. Status Solidi (a) *40*, 487 (1976)
4. E. Görlich, Ceramics International *8*, 3 (1982)
5. JANAF Thermochemical Tables, NSRDS-NBS 37, (1971)
6. F.J. Grunthaner, P.J. Grunthaner, R.P. Vasquez, B.F. Lewis, J. Maserjian, A. Madhukar, Phys. Rev. Lett. 43, 1683 (1979)

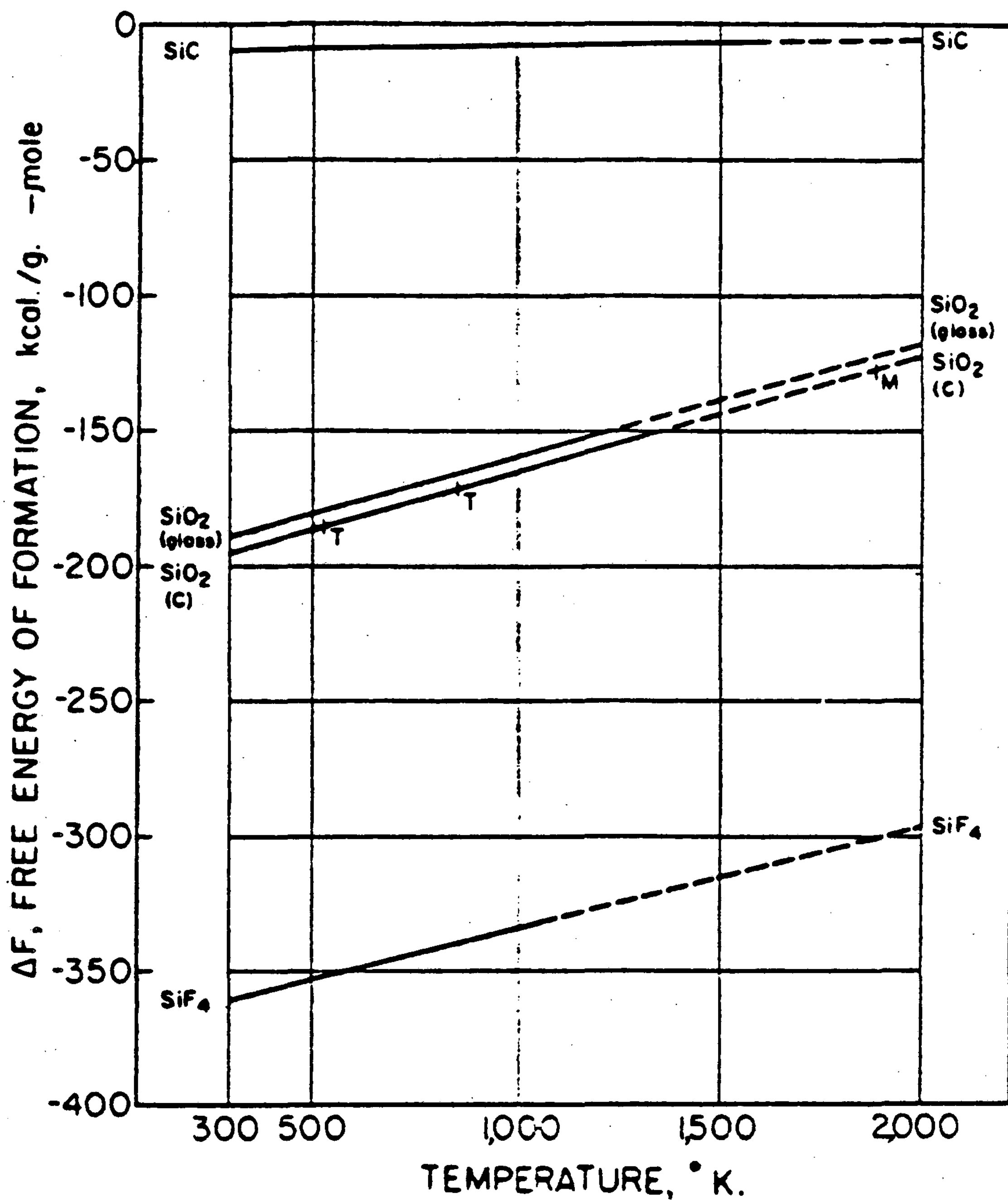


XBL 858-3701

Fig. 2.1.2. Free energy of formation, ΔF, as a function of temperature for vitreous and crystalline $SiO_2$ (from C.E. Wicks et al. [2.1.3]). Note that there is a small difference in the ΔF values for both forms.

**Table II. Effects of various cations in catalysing silica.**

| Cation | Ionic radius $r_c$ | $a = (r_c + r_a)$ | Effects |
|---|---|---|---|
| $K^+$ | 1·33 Å | 2·73 Å | Tridymite-forming catalysts |
| $Na^+$ | 0·95 | 2·35 | |
| $Li^+$ | 0·60 | 2·00 | Cristobalite-forming catalysts |
| $Ba^{2+}$ | 1·35 | 2·75 | |
| $Ca^{2+}$ | 0·99 | 2·39 | |
| $Fe^{2+}$ | 0·76 | 2·16 | |
| $Mg^{2+}$ | 0·65 | 2·05 | |
| $Be^{2+}$ | 0·31 | 1·71 | Quartz-forming catalysts |
| $Al^{3+}$ | 0·50 | 1·90 | |
| $Ti^{4+}$ | 0·68 | 1·08 | |

$r_c$ = cation radius.

$r_a$ = anion radius.

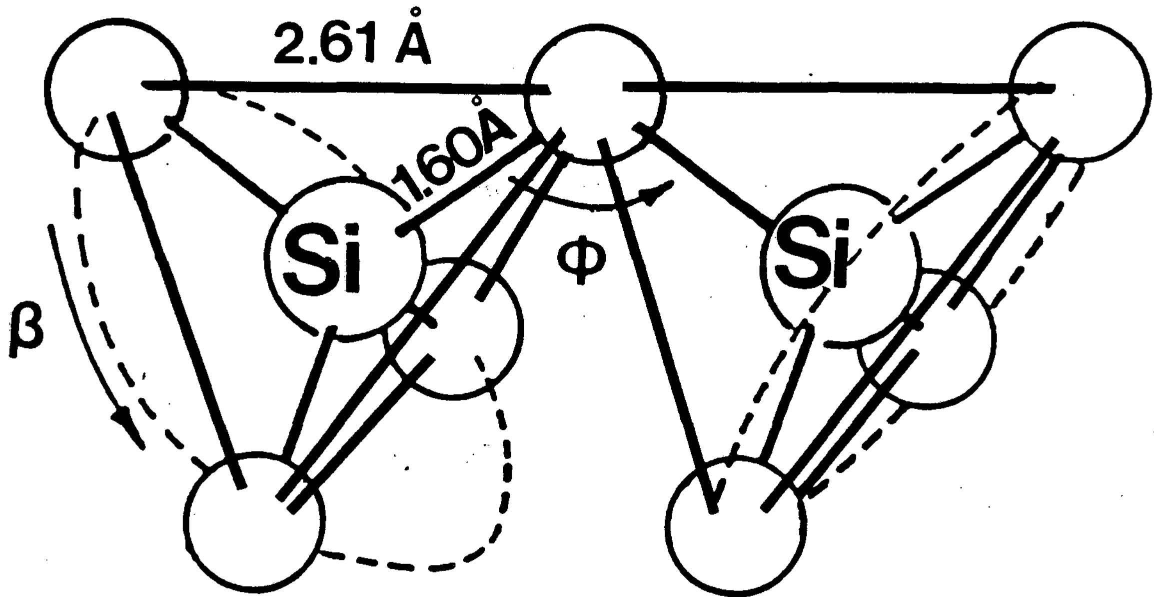


XBL 858-3558

Fig. 2.1.3. Two [$SiO_4$] tetrahedra joined by a bridging oxygen atom. The distance between oxygen atoms in the same tetrahedra is 0.261 nm and the Si-O bond length is 0.160 nm; $\phi$ indicates the Si-O-Si bridging angle; $\beta$ is a free rotation angle.

polymer consisting of [$SiO_4$] tetrahedra playing the role of monomers.

"Polymerization" is accomplished through Si-O-Si "oxygen bridges" in which an oxygen atom is common to two silica tetrahedra (Fig. 2.1.3). The interconnected [$SiO_4$] tetrahedra form a silica network. Different polymorphs differ only by the distribution of the bridging angles $\phi$ and the number N of silica tetrahedra in N membered rings (see Table I). The network of polymorphs consists of 6 membered rings in the case of quartz, tridymite and cristobalite, 5-7-8 membered rings in keatite, 4-6-8-9 membered rings in coesite, and 4-5-6-7-8 in noncrystalline amorphous $SiO_2$ [2.1.4-2.1.9]. Grunthaner et al. [2.1.8] also suggested the existence of 3 membered rings in silica near the Si-$SiO_2$ interface. The presence of such multiple-membered rings results in the relatively open structure of the $SiO_2$ networks. Variation in distribution of the Si-O-Si bridging angle $\phi$ between different $SiO_2$ polymorphs is relatively small. This is illustrated in Fig. 2.1.4 showing the comparison between the distribution of $\phi$ for vitreous $SiO_2$ and cristobalite as determined from x-ray diffraction experiments [2.1.10]. The above examples suggest that variations between the $SiO_2$ polymorphs are conformational in nature, that is, significant changes in long range order (LRO) are associated with a little change in the energy content. The changes in the LRO are associated with substantial changes in the density of polymorphs (17 percent difference between quartz and amorphous $SiO_2$). This is also seen by observing the dependence of average refractive index on density (Fig. 2.1.5).

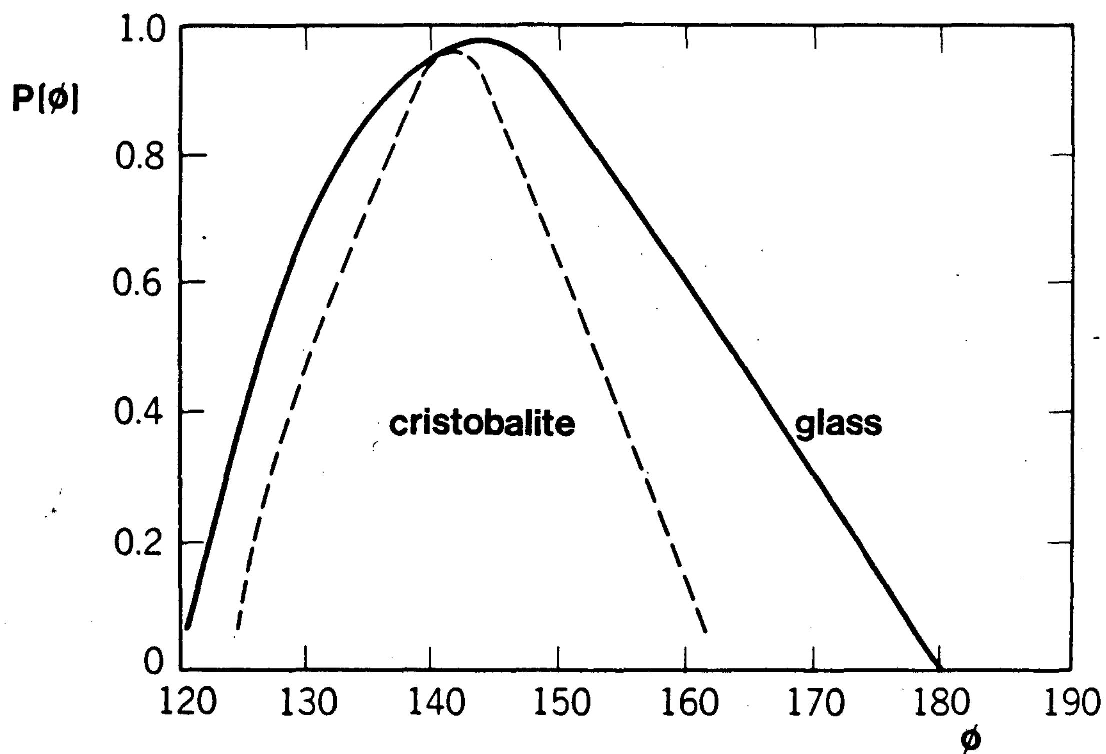


XBL 845-1872

Fig. 2.1.4. Comparison of the distribution of Si-O-Si bridging angles in cristobalite (crystalline) and amorphous forms of silica (from R.L. Mozzi, Sc.D. thesis, MIT, 1967).

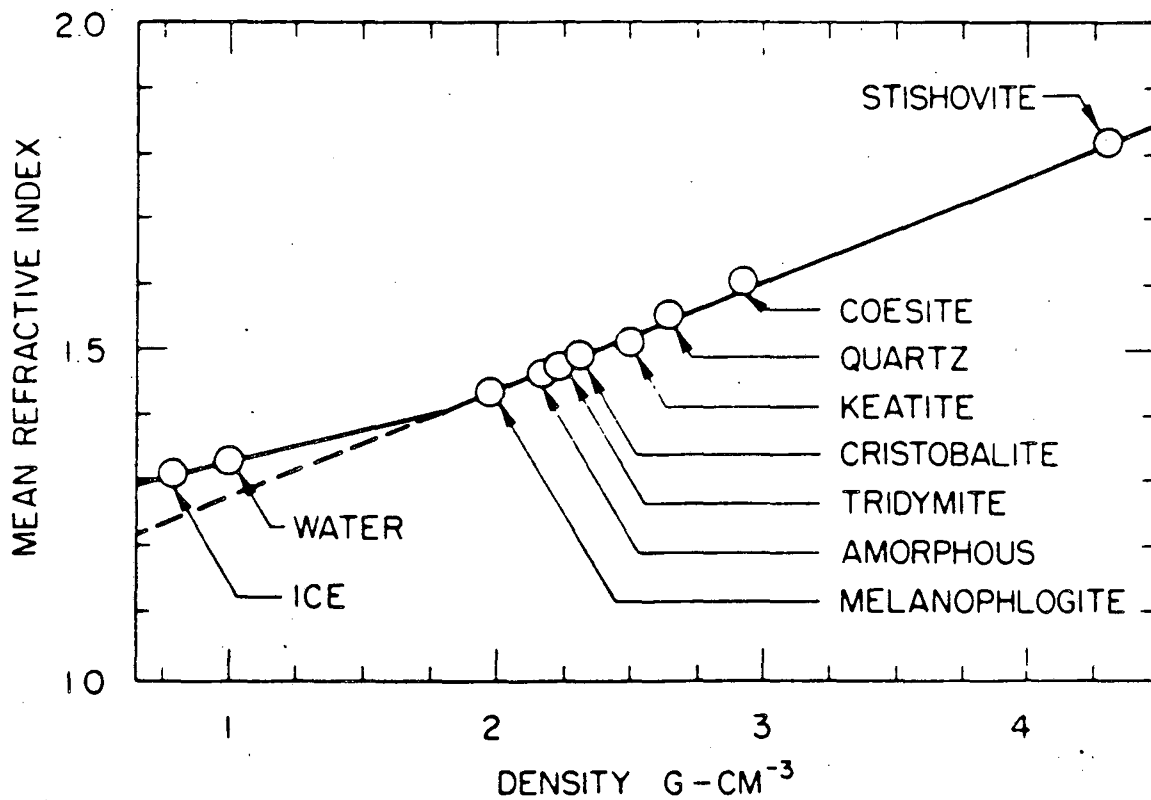


XBL 858-3554

Fig. 2.1.5. The mean refractive index, n, as a function of the density of different $SiO_2$ polymorphs (from Iler [2.1.11]).

## 2.2 Models of Amorphous $SiO_2$

The structure of noncrystalline $SiO_2$ has been of considerable interest because it relates to properties of glass (vitreous) $SiO_2$ and $SiO_2$ layers formed during thermal oxidation of single crystal silicon. Investigations of the structure of amorphous materials by x-ray, electron, neutron diffraction and other techniques (for example IR spectroscopy) have resulted in various structural models, differing in the amount of disorder they permit. These models can be divided into three broad groups by their degree of randomness.

The microcrystallite model, based upon connected microcrystallites, is attributed to Porai-Koshitz [2.2.1]. This model has been used for interpretation of diffraction results [2.2.2, 2.2.3, 2.2.4], IR results [2.2.5], and electron microscopy investigation [2.2.6, 2.2.7, 2.2.8, 2.2.9]. According to this model, the broad diffraction peak is in part due to the small crystal size (about 20 Å diameter) and also due to the structure of crystalline boundaries. Intercrystalline coordination is important because of the relatively large ratio of surface to intracrystalline [$SiO_4$] tetrahedral units in such models.

The ordered regions ("crystallites") were reported to consist of β-quartz, β-cristobalite or tridymite depending upon the study, due possibly to the different methods of vitreous silica preparation. Interestingly, despite the structural similarity between fused silica and thermally-grown $SiO_2$ films on silicon, different crystallization behavior was reported. Fused silica was always observed to crystallize as cristobalite while thermally-grown silica was observed to crystallize as cristobalite, quartz or tridymite [2.2.10, 2.2.11].

Revesz [2.2.12] suggested that the microcrystalline tridymite structure of thermally-grown $SiO_2$ on silicon results in the formation of ordered regions with large channels. The structure of the channels was suggested by Revesz to be substrate-orientation dependent and would therefore influence oxygen species transport during thermal oxidation of silicon. Existence of voids in the silica was suggested in the TEM work of Irene, et al. [2.1.12]. The suggested size of the pores was 5.0 nm or less. However it has not been substantiated by careful TEM experiments.

The continuous random network model (CRN) permits all possible local arrangements of [$SiO_4$] tetrahedra. It does not contain any regular building blocks. The model was first proposed by Zacharisen [2.2.13], and constructed by Evans and King [2.2.14] and Bell and Dean [2.2.15] for $SiO_2$. Several CRN models were also built for amorphous tetrahedrally coordinated monatomic materials [2.2.16, 2.2.17, 2.2.18, 2.2.19] as well as for amorphous As [2.2.20]. The CRN model can be easily extended in all directions, without introducing any dangling bonds. Attempts to connect two general mutually-orientated microcrystallites, or a network to a crystal face, without large bond distortion and dangling bond generation have been, to a large extent, unsuccessful. Only a few special mutual arrangements of two crystallites could be easily connected to each other by a distorted layer. Such grain boundary layers then have a significant regularity.

The amorphic model has characteristics common to both the microcrystalline and the CRN models. The structure is built up from well-defined elements of which the principal one is called an amorphon

or vitron (the pentagonal dodecahedron). The constituent elements are non-crystallographic. The model cannot be constructed without accommodating strain and developing defects. Four amorpha form the basic tetrahedron subunit. Tetrahedral stacking is non-spacefilling and limits the number of tetrahedral subunits to less than 20. Such a "microcrystal" can only be connected to any other one with the help of the connecting layer, thus making this model intermediate between the microcrystallite and CRN models. The first such model was proposed for $SiO_2$ by Tilton [2.2.21].

At this point the CRN model appears to be the most probable one for $SiO_2$ thermally grown on silicon, and is suggested in the present study. Although crystallites have been observed in some reported research they have resulted from the unintended introduction of a cation catalyst during processing [2.2.22], and are therefore, not pertinent to this work.

REFERENCES - CHAPTER 2


2.1.1 F.R. Boyd, J.L. England, J. Geophys. Res. 65, 749 (1960).

2.1.2 W.D. Kingery, H.K. Bowen, D.R. Uhlman, "Introduction to Ceramics," 2nd edition, J. Wiley & Sons, New York (1975), p. 83.

2.1.3 C.E. Wicks, F.E. Block, "Thermodynamic properties of 65 elements--their oxides, halides, carbides, and nitrides," Bulletin 605, Bureau of Mines, U.S. Government Printing Office, Washington (1963).

2.1.4 E. Gorlich, Ceramics International, 8, 3 (1982).

2.1.5 K. Hubner, Phys. Status Solidi (a) 40, 133 (1977), 40, 487 (1977), 42, 501 (1977).

2.1.6 K. Hubner, A. Lehman, Phys. Status Solidi (a) 46, 451 (1978).

2.1.7 F.J. Grunthaner, P.J. Grunthaner, R.P. Vasquez, B.F. Lewis, J. Maserjin, A. Madhukar, Phys. Rev. Lett. 43, 1683 (1979).

2.1.8 F.J. Grunthaner, J. Maserjian, in "The Physics of $SiO_2$ and its Interfaces," S.T. Pantelides, Ed. (Pergamon Press, New York, 1978), p. 389.

2.1.9 R.N. Naucho, A. Madhukar, ibid., p. 60.

2.1.10 R.L. Mozzi, B.E. Warren, J. Appl. Crystallogr. 2, 164 (1969).

2.1.11 R.K. Iler, "The Chemistry of Silica," J. Wiley & Sons, New York (1979), p. 19.

2.1.12 E.A. Irene, J. Electrochem. Soc. 125, 1708 (1978).

2.2.1 E.A. Porai-Koshitz, Glastech. Ber. 32, 450 (1959).

2.2.2 J.H. Konnert, J. Karl, G.A. Ferguson, Science 179, 177 (1973).

2.2.3 A.H. Narten, J. Chem. Phys. 56, 1905 (1972).

2.2.4 R.L. Mozzi, B.E. Warren, J. Appl. Cryst. 2, 164 (1969).

2.2.5 E. Gorlich, K. Blaszczak, G. Siemienska, J. Mat. Sci. 9, 1926 (1974).

2.2.6 M.L. Rudee, Phys. Stat. Sol. (b) 46, K1 (1971).

2.2.7 M.L. Rudee, A. Howie, Phil. Mag. 25, 1001 (1972).

2.2.8 A. Howie, O.L. Krivanek, M.L. Rudee, Phil. Mag. 27, 235 (1973).

2.2.9 J. Bando, K. Ishizuka, J. Non-Cryst. Solids 33, 375 (1979).

2.2.10 A.A. Konova, M.G. Michaiov, Phys. Stat. Sol. (a) 50, 627 (1978).

2.2.11 A. Barna, M. Nemeth-Sallay, I.C. Szep, P.I. Dienko, V.G. Litovchenko, P.I. Marchenko, G.F. Romanova, Thin Solid Films, 55, 355 (1978).

2.2.12 A.G. Revesz, Phys. Stat. Sol. (a)57, 235 (1980).

2.2.13 W. Zacharisen, J. Am. Chem. Soc. 54, 3841 (1932).

2.2.14 D.L. Evans, S.V. King, Nature 212, 1353 (1966).

2.2.15 R.J. Bell, P. Dean, Nature 212, 1354 (1966), Phil. Mag. 25, 235 (1973).

2.2.16 O.L. Krivanek, PhD. thesis, University of Cambridge, Trinity College (1975).

2.2.17 N.J. Shevchik, Phys. Stat. Sol. (b) 58, 111 (1973).

2.2.18 P. Steinhardt, R. Alben, D. Weaire 15, 199 (1974).

2.2.19 G.A.N. Connell, R.J. Tempkin, AIP Conf. Proceedings 20, 192 (1974).

2.2.20 G.N. Greaves, E.A. Davis, Phil. Mag. 29, 1201 (1974).

2.2.21 L.W. Tilton, J. Res. Nat. Bur. Stand. 59, 139 (1957).

2.2.22 F. Ponce, private communication.

# 3. MODELS OF THE $Si-SiO_2$ INTERFACE

Different models of the interface structure have been proposed, based mainly upon the ability of a particular technique to probe some property of the interface. Some of the techniques used to study the $Si-SiO_2$ interface include x-ray photoelectron spectroscopy (XPS), Rutherford back scattering (RBS) ion channeling spectroscopy, ellipsometry, Auger electron spectroscopy, secondary ion mass spectroscopy (SIMS), electron paramagnetic resonance (EPR), surface mobility measurements in the inversion layers, current-voltage measurements, transmission electron microscopy, and low energy electron diffraction (LEED) combined with oxide etching.

So far most of the experimental data have been obtained in studies using only one technique. Therefore many models of the $Si-SiO_2$ interface structure could only be qualitatively compared. Some of the most commonly accepted models of the $Si-SiO_2$ region, based on interpretation of data obtained from some of these experiments, will be discussed in the following sections.

## 3.1 Models of the $Si-SiO_2$ Interface Derived from XPS Studies.

The x-ray photoemission technique [3.1.1] is particularly well suited for the analysis of the structural chemistry of thin layer films grown or deposited onto a dissimilar substrate. Analysis of the kinetic energy spectrum of the emitted photoelectrons gives chemical information through measurement of the peak positions. The intensity of the peak is related to the number of probed atoms, the photoioniza-tion cross-section for the atomic core level studied, the x-ray energy

utilized, the inelastic mean free path for the observed electrons, the x-ray flux, and instrumental factors. Only electrons which do not undergo energy losses contribute to peak intensities, and therefore attenuation of XPS signals can be treated as a simple exponential function of the inelastic mean free path ($\lambda$) and the layer thickness. This technique provides a means to monitor the uniformity of consecutive layers when combined with etching techniques [3.1.2, 3.1.3, 3.1.4], and therefore is useful in the determination of the chemistry and structure of the Si-$SiO_2$ interface.

Early interpretations of XPS (ESCA) studies of the Si-$SiO_2$ interface suggested the existence of transition layers 1.5-2.0 nm thick with stoichiometry changing from SiO close to the silicon, to $SiO_2$ in the rest of the film [3.1.4-3.1.10]. The width of the transition layer in these studies was independent of oxidation processing conditions, oxidant, oxidizing ambient, oxide thickness or high temperature annealing, and was narrower for {100} than {111} Si substrates. In another study [3.1.11-3.1.12] a 0.2-0.3 nm layer of SiO was found at the Si-$SiO_2$ interface. This transition region was considered to be a first monolayer of Si substrate in contact with $SiO_2$ film. Grunthaner et al. [3.1.3, 3.1.4, 3.1.13] proposed the model shown in Fig. 3.1, with a stoichiometric $SiO_2$ amorphous film extending up to the interface, and the transition from Si to $SiO_2$ occurring in a region 0.3-0.7 nm wide. This transition region consisted of Si atoms in incompletely oxidized states $Si^{1+}$, $Si^{2+}$, $Si^{3+}$ (bonded to 1, 2, 3 oxygen atoms respectively) with the ratios

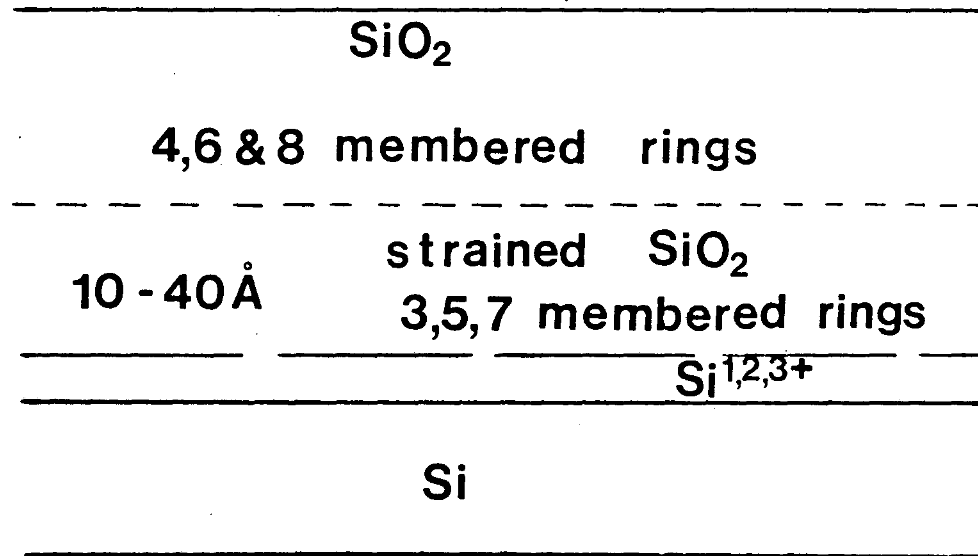


XPS, Grunthaner et. al./1977-84/

Fig. 3.1. Schematic representation of the Si-$SiO_2$ transition layer derived from XPS studies.

varying for different Si surfaces [3.1.3, 3.1.4, 3.1.12, 3.1.13-3.1.17]. There are considerable differences in the estimated ratios of Si atoms in incompletely oxidized states present at the interface. Grunthaner et al. [3.1.3] estimated that the ratio of $Si^{3+}:Si^{2+}:Si^{1+}$ was 2:3:2 respectively for (100) oxidized wafers; Bianconi et al. [3.1.17] suggested the existence of incompletely oxidized Si states without specifying the ratio; Hollinger et al. [3.1.18] estimated approximately the same ratio of incompletely oxidized states for {111} and {100} oxidized Si surfaces, equal to 0.4:0.3:0.3. In other studies Hecht et al. [3.1.15] concluded that the $Si^{1+}$ and $Si^{2+}$ states were localized at the Si-$SiO_2$ interface. The $Si^{3+}$ state extended into first 20 Å of the $SiO_2$, and this was attributed to the existence of two $Si^{3+}$ states, one localized at the interface and one due to Si-H bonding in the oxide. These authors found orientation dependence of the suboxide distribution, with greater $Si^{1+}:Si^{2+}$ and $Si^{3+}:Si^{2+}$ ratios for oxidized {111} Si than for oxidized {100} Si. In addition they observed more $Si^{1+}$ and $Si^{2+}$ states and fewer $Si^{3+}$ states after post-oxidation anneal. However they did not observe any changes in sub-oxides distribution for dry or steam oxidation. The 1.0-4.0 nm wide layer next to the interface consisted of a strained $SiO_2$. A similar conclusion was reached by Hollinger [3.1.16] from his XPS, UPS and Auger investigations of the interface. The topology of the network in this layer near the Si-$SiO_2$ interface was described as consisting of 3, 5, and 7 membered [$SiO_4$] tetrahedra rings and was different from

that of bulk (further away from the silicon) $SiO_2$ consisting of 4, 6, and 8 membered rings.

3.2 Models of the $Si-SiO_2$ Interface Derived from RBS-Ion Channeling Studies.

Rutherford backscattering-ion channeling techniques can provide information about the magnitude of the displacement of atoms from their lattice position near the surface [3.2.1, 3.2.2], as well as about the number of atoms displaced.

Recently both conventional (backscattering) and thin crystal (transmission) scattering geometries with the grazing angle detector arrangement were used to study the stoichiometry and the $Si-SiO_2$ interface disorder [3.2.3-3.2.10]. The experiments involved a series of thermally-grown oxides on differently-oriented Si substrates 0.4 to 7.0 nm thick in which changes in stoichiometry as a function of oxide thickness could be monitored.

The plot of Si vs. oxygen areal densities for a range of oxide thicknesses did not extrapolate to zero oxide coverage. The difference between the extrapolated (oxide-covered) Si surface peak for zero oxide coverage and the calculated value for a bulk-like Si surface structure was interpreted as an excess of Si atoms at the interface which could amount to 1.6 to 2.1 monolayers depending on Si substrate orientation. These results are summarized in Table III. This excess of Si atoms at the interface was interpreted as consisting of either two monolayers of Si in disregistry with the bulk (e.g. reconstructed Si) or a thin region about 0.5 nm or less of nonstoichiometric oxide.

Table III. Comparison of Si surface peaks on clean and oxide covered surfaces.

| Substrate surface/ Channeling direction and ion energy | Clean Si surface[b] [monolayer[a]] | Oxide[c] [monolayer] | Bulk-like surface[d] [monolayer] | ΔSi[e] [monolayer] |
|---|---|---|---|---|
| Si(001)/<001> 0.8 MeV | 14.6 (2 x 1)[1] | 13.3[3] | 11.2 | 2.1 |
| Si(011)/<011> 0.8 MeV | | 0.0[4] | 6.7 | 2.3 |
| Si(111)/<111> 1.0 MeV | 12.0 (7 x 7)[2] | 11.6[5] | 10.0 | 1.6 |
| Si(111)/<001> 1.0 MeV | 9.4 (7 x 7)[2] | 8.2[5] | 6.1 | 2.1 |

a) One monolayer corresponds to : Si(001) $6.8 \times 10^{14} cm^{-2}$; Si(011), $9.6 \times 10^{14} cm^{-2}$; Si(111), $7.8 \times 10^{14} cm^{-2}$

b) Si surface peaks measured on clean reconstructed surfaces (source indicated in parentheses)

[1] L.C. Feldman, P.J. Silverman, I. Stensgaard, Nucl. Instrum. Methods 168, 589 (1980)

[2] R.J. Culbertson, L.C. Feldman, P.J. Silverman, Phys. Rev. Lett. 45, 2043 (1980).

c) Si surface peak extrapolated to zero oxide coverage:

[3] T.E. Jackman, J.R. MacDonald, L.C. Feldman, P.J. Silverman, I. Stensgaard, Surf. Sci. 100, 35 (1980)

[4] L.C. Feldman, I. Stensgaard, P.J. Silverman, T.E. Jackman in Proc. Int. Conference on "Physics of $SiO_2$ and Its Interfaces," S.T. Pantelides, Ed. Pergamon Press, Oxford (1978), p. 344.

[5] R. Haight, W.M. Gibson, T. Narusawa, L.C. Feldman, J. Vac. Science Technol. 18, 1973 (1982).

d) The calculated value for bulk-like (unreconstructed) surface structure.

e) ΔSi, the difference between the extrapolated (oxide covered) surface peak and the calculated value.

The schematic representation of this model of the $Si-SiO_2$ interface is shown in Fig. 3.2.

3.3 Models of the $Si-SiO_2$ Interface Derived on the Basis of EPR Studies.

The electron paramagnetic resonance (EPR) technique was used to study the $Si-SiO_2$ interfaces obtained by thermal oxidation of {100} [3.3.1-3.3.8], {111} [3.3.5-3.3.15] and {110} [3.3.8] Si surfaces. This technique is sensitive to atoms or clusters of atoms with unpaired electron spin or spins, which are characterized by the gyromagnetic tensor g. The symmetry of this tensor depends upon the local crystal environment of the electron spin. Interaction of the EPR center with the external magnetic field as well as with the magnetic moments of electron or nuclear spins in its neighborhood allows measurement of the density of such defects, as well as determination of the gyromagnetic tensor symmetry. Characteristic EPR $P_b$ centers were found at the $Si-SiO_2$ interfaces by determination of their density as a function of decreasing oxide thickness upon using decremental etching [3.3.4, 3.3.5]. These centers were found to be distinct from those of bulk Si and $SiO_2$ and were found to be dependent on surface crystallography. In the case of the (111) oxidized Si surface one EPR $P_{bo}$ center was observed. This center had axial symmetry of the g tensor with its axis along [111] direction normal to the oxidized surface and it has been identified with the unbound orbital (dangling bond) •Si≡ normal to the (111) interface plane [3.3.5, 3.3.6]. Two $P_b$ EPR centers were found at the (100) $Si-SiO_2$ interfaces, one corresponding to the $P_{bo}$ (•Si≡) center on (100) Si and the other, the $P_{b1}$

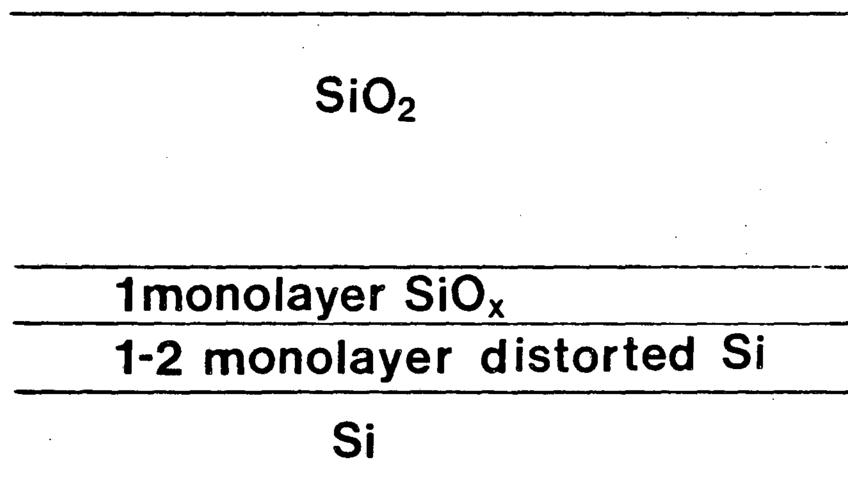


Fig. 3.2. Schematic representation of the Si-$SiO_2$ interface region derived from RBS-ion channeling studies.

center, tentatively associated with the $Si-SiO_2$ [3.3.5, 3.3.6]. In the case of oxidized (110) Si surfaces only $P_{bo}$ centers were found at the interface. These investigations led to the models of $Si-SiO_2$ interfaces shown in Fig. 3.3, which illustrates how these EPR centers are related to the interface crystallography, and suggests that they are associated with the advancing oxidation front [3.3.5-3.3.8]. These EPR centers have been found to correlate with the electronic defects characteristic of the $Si-SiO_2$ interface, namely interface states. The ratio of $P_b$ centers observed on {100} and {111} oxidized Si surfaces was similar to the ratio of interface states and approximately equal to 1:3 [3.3.6]. The density of $P_b$ centers increased in irradiated MOS structures in the same manner as density of interface states, further confirming the association of at least some interfacial states with dangling bonds at the $Si-SiO_2$ interface (•Si ≡ EPR centers) [3.3.12, 3.3.15].

Recently, attempts have been made to estimate the distance between the dangling bonds at the {111} $Si-SiO_2$ interface [3.3.16, 3.3.17]. These first analyses of the data suggested distribution of the dangling bonds with enhanced separation, about 4 nm from one another, on the atomically flat {111} interface. This separation of the dangling bonds was tentatively interpreted as a result of relaxation of the strain at the $Si-SiO_2$ boundary. However lack of dipolar broadening of the EPR absorption line, which formed the basis for these conclusions, could alternatively be attributed to the existence of numerous steps laterally separated by distances in the range of 10 Å.

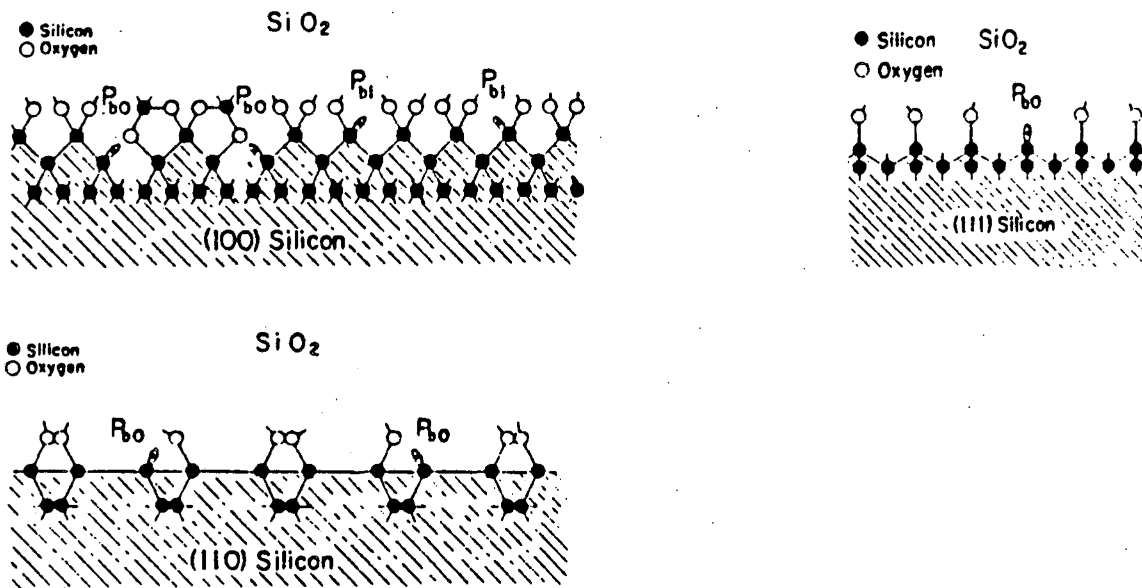


XBL 858-3585

Fig. 3.3. The models of the Si-$SiO_2$ interface derived from EPR observations (from Poindexter et al. [3.3.8]).

a) $P_{b0}$ and $P_{b1}$ EPR centers at a (100) oxidized Si surface.

b) A $P_{b0}$ center at a (111) oxidized surface.

c) $P_{b0}$ centers at a (110) oxidized surface.

3.4 Models of the Si-$SiO_2$ Region Derived from Ellipsometry Experiments

The ellipsometry technique [3.4.1] has been used for determining the oxide thickness and refractive indices of the oxide film and of a possible transition layer at the Si-$SiO_2$ interface. This technique measures the state of polarization of linearly polarized light after reflection from the specimen [3.4.2-3.4.8]. In the ellipsometry experiment two parameters, the change in relative phase of the incident and reflected beams $\Delta$, and the arctangent of the amplitude ratio change for incident and reflected beams $\psi$, are related to the ellipsometer angle measurement. The value of these parameters is a function of the thickness and the number of layers present, the indices of refraction of the layers and the substrate itself, the wavelength of light used and the incidence angle of the beam upon the specimen [3.4.1]. The data analysis assumes homogeneous layers described by the same index of refraction terminating abruptly at the interfaces.

A simple model assuming one $SiO_2$ layer of the same refractive index was used in the first ellipsometric studies of the silicon oxide on silicon [3.4.2-3.4.5]. Studies by Taft et al. [3.4.6] included in the analysis both $\Delta$ and $\psi$ an effect of birefringence caused by strain in the oxide. This effect was found to have little influence on the calculated refractive index for oxide thinner than 150 nm; however, it had pronounced influence for increased oxide thicknesses. These authors found that introduction of a thin intermediate layer allowed them to measure the thickness of the oxide layers over the range from 30.0-700.0 nm using the same refractive index for oxide, equal to 1.4626 ± .001 at $\lambda$ = 546.1 nm.

The choice of one homogeneous interlayer imposed limits on its thickness depending upon the refractive index chosen (e.g., 0.6 nm if n = 2.1-3.0 or 1.0 nm if n = 1.7). The estimated excess of Si in the intermediate layer was given as 2 x $10^{15}$ atoms $cm^{-2}$ or two extra layers of Si atoms in the transition region.

Similar conclusions have been obtained from spectroscopic ellipsometry studies [3.4.7] of the Si-$SiO_2$ interfaces formed on {111}, {100} and {110} Si surfaces. A transition layer 0.7 ± 0.2 nm wide with average stoichiometry $SiO_{0.4\pm0.2}$ was found at the Si-$SiO_2$ interface. The analysis included determination of the optical response function for the case of crystalline Si and $SiO_2$ as well as for the chemical or physical mixture of average composition $Si_x(SiO_2)_{1-x}$. The fit to the ellipsometric data was found to be better, especially for thicker oxides, when an intermediate layer 6.6 ± 0.9 Å thick, consisting of a chemical mixture $Si_x(SiO_2)_{1-x}$ was included in the Si-$SiO_2$ model, although a physical mixture (which could represent microroughness at the interface) could not be definitely excluded. The refractive index of this layer, 3.2 ± 0.5, was comparable to that estimated by Taft et al. [3.4.6].

The possible explanation of the transition layers consisting of physically mixed Si and $SiO_2$ in the form of Si surface roughness was suggested by Mazur et al. [3.4.8] on the basis of high resolution electron microscopy determination of the Si-$SiO_2$ structure which was found to be rough on a scale corresponding to the interlayer thickness. Estimates of the excess of Si atoms due to interface morphology

in the interface region was of the order of $10^{15}$ atoms $cm^{-2}$. Therefore although the transition between Si-$SiO_2$ was abrupt on an atomic scale, it could be considered as a physical mixture or possibly chemical mixture from the point of view of the optical response function. Preliminary work on the influence of surface roughness indicates that the layer containing the roughness could be described by the average refractive index of the surface and the film [3.4.9, 3.4.10]. The refractive index of the layer was found to be dependent upon details of the morphology at the interface [3.4.9]. These results support the suggestion made by Mazur et al. [3.4.8] concerning the interface transition layer.

### 3.5 Auger Electron Spectroscopy Studies of the Si-$SiO_2$ Interface

A considerable number of studies of the Si-$SiO_2$ interface have been performed using Auger spectroscopy [3.5.1-3.5.10]. In these experiments sputtering was used to profile the oxide and Si-$SiO_2$ region. The earliest work [3.5.1, 3.5.2] suggested a model of the Si-$SiO_2$ interface described by a natural interface roughness and inclusions of Si in the oxide close to the interface. The width of the transition layer for oxide grown at 1200°C in dry $O_2$ on (100) Si was estimated to be about 35 Å thick. This model was inconsistent with TEM observations [3.5.10, 3.5.11], and was subsequently revised to include advances in understanding of possible artifacts due to nonuniform sputter profiling [3.5.5, 3.5.7-3.5.9]. The revised model describes interface morphology as consisting of long range (about 20 μm period) undulations with an amplitude of about 1 nm. The

transition $SiO_x$ layer was postulated to exist after identification of an intermediate state of Si [3.5.7]. The model of the interface does not provide any new information compared with those already discussed.

### 3.6 The Structure of the Si-$SiO_2$ Interface as Determined from Low Energy Electron Diffraction, and the Surface Charge Mobility at High Inversion

Charge mobility in the high inversion mode of a MOSFET [3.6.1] is an important parameter which determines the operational speed of these devices. High electric field between the metal gate and a substrate confines charges close to the Si-$SiO_2$ interface. Under these circumstances, the charges flowing between the source and a drain (see Fig. 1.1.2) experience scattering due to the fluctuations of potential resulting from the interface roughness [3.6.2-3.6.8].

The theory of surface roughness scattering at the Si-$SiO_2$ interface [3.6.7] explicitly included surface roughness parameters: correlation length (an average half period of undulation) and asperity (an average amplitude). Using mobility data, Cheng and Sullivan [3.6.2] estimated the surface roughness parameters: correlation length $L = 2.36$ nm and asperity $\Delta = 0.35$ nm. These parameters were found to be similar to those obtained from direct experimental observation of Si-$SiO_2$ interface cross-sections by transmission electron microscopy [3.6.9, 3.6.10]. Due to the fact that the high resolution TEM image is a projection of the potential along the electron beam, roughness parameters could be underestimated and morphology might be

more complicated than that observed in the HREM image. This is suggested in this work and earlier by Mazur et al. [3.6.10] for (100) Si oxidized surfaces. More recent experiments involving direct correlation of the roughness parameters obtained from mobility measurements and high resolution electron microscopy [3.6.11, 3.6.12] (performed on the same specimens) seems to indicate that this is indeed the case.

The mobility of the charges in the inversion layers has been correlated with the determination of surface roughness from spot-profile analysis of low energy electron diffraction (SPA-LEED) combined with etching of the oxide [3.6.13-3.6.16]. In these studies the following conclusions have been reached:

a) The steps at the Si-$SiO_2$ interface were randomly distributed. The step-atom density was obtained from model calculations of the measured spot broadening of LEED.

b) The roughness was found to decrease in the case of the low oxidation rates observed for thick oxide and dry $O_2$ atmosphere as well as some nitrogen anneals.

c) Strong correlation was reported between Hall mobility and atomic roughness at high inversion which was observed even at room temperature.

d) Correlation between the atomic roughness and interface state density was observed even after postmetalization-annealing.

e) Surface states were preferentially associated with the creation of dangling bonds at the kink or edge atoms, while oxide fixed charges were associated with ionized atoms located at the steps or kinks.

REFERENCES - CHAPTER 3


3.1.1 K. Sigbahn, C. Nordling, A. Fehlman, R. Nordberg, K. Hamrin, J. Hedman, G. Johnsson, T. Bergman, S-E. Karlsson, I. Lindberg, "ESCA - Atomic Molecular and Solid State Structure Studied by Means of Electron Spectroscopy," Almquist and Wiksells, Uppsala (1967).

3.1.2 R.P. Vasquez, F.J. Grunthaner, Surface Sci. 99, 681 (1980).

3.1.3 F.J. Grunthaner, P.J. Grunthaner, R.P. Vasquez, B.P. Lewis, J. Maserjian, J. Vac. Sci. Technol. 16, 1443 (1979).

3.1.4 F.J. Grunthaner, J. Maserjian, in "The Physics of $SiO_2$ and Its Interfaces," S.T. Pantelides, Ed., Pergamon Press, New York, 1978, p. 389.

3.1.5 R.A. Clarke, R.L. Tapping, M.A. Hopper, L. Young, J. Electrochem. Soc. 122, 1347 (1975).

3.1.6 S.I. Raider, R. Flitsch, J. Vac. Sci. Technol. 13, 58 (1976).

3.1.7 R. Flitsch, S.I. Raider, J. Vac. Sci. Technol. 12, 301 (1975).

3.1.8 S.I Raider, R. Flitsch, IBM J. Develop. 22, 294 (1978).

3.1.9 S.I. Raider, R. Flitsch, in "The Physics of $SiO_2$ and Its Interfaces," S.T. Pantelides, Ed., Pergamon Press, New York, 1978, p. 384.

3.1.10 T. Hattori, T. Nashina, ibid., p. 379.

3.1.11 A. Ishizaka, S. Iwata, Y. Kamigaki, Surface Sci. 84, 355 (1979).

3.1.12 A. Ishizaka, S. Iwata, Appl. Phys. Lett. 36, 71 (1980).

3.1.13 F.J. Grunthaner, J. Maserjian, IEEE Trans. Nucl. Sci. NS-24, 2108 (1977).

3.1.14 T. Hattori, T. Suzuki, Appl. Phys. Lett. 43, 470 (1983).

3.1.15 M.H. Hecht, P.J. Grunthaner, F.J. Grunthaner, in Proceedings of International Conference on Physics of Semiconductors, Aug. 6-10, 1984, San Francisco, California, to be published in J. Vac. Sci. Technol.

3.1.16 G. Hollinger, F.J. Himpsel, Appl. Phys. Lett. 44, 93 (1984).

3.1.17 A. Bianconi, R.S. Bauer, Surface Sci. 99, 76 (1980).

3.1.18 G. Hollinger, Applications of Surf. Sci. 8, 318 (1981).

3.1.19 F.J. Grunthaner, P.J. Grunthaner, R.P. Vasquez, B.F. Lewis, J. Maserjian, A. Madhukar, Phys. Rev. Lett. 43, 1683 (1979).

3.2.1 L.C. Feldman, J.W. Mayer, S.T. Picraux, "Materials Analysis by Ion Channeling - Submicron Crystallography," Academic Press, New York, 1982.

3.2.2 B.K. Chu, J.W. Mayer, M.-A. Nicolet, "Backscattering Spectrometry," Academic Press, New York, 1978.

3.2.3 N.W. Cheung, Ph.D. thesis, California Institute of Technology (1980).

3.2.4 N.W. Cheung, L.C. Feldman, P.J. Silverman, I. Stensgaard, Appl. Phys. Lett. 35, 859 (1979).

3.2.5 L.C. Feldman, P.J. Silverman, J.S. Williams, T.J. Jackman, I. Stensgaard, Phys. Rev. Lett. 41, 1396 (1978).

3.2.6 T.E. Jackman, J.R. MacDonald, L.C. Feldman, P.J. Silverman, I. Stensgaard, Surf. Sci. 100, 35 (1980).

3.2.7 L.C. Feldman, I. Stensgaard, P.J. Silverman, T.J. Jackman, in "The Physics of $SiO_2$ and Its Interfaces," S.T. Pantelides, Ed., Pergamon Press, 1978, p. 344.

3.2.8 R.J. Culbertson, L.C. Feldman, P.J. Silverman, Phys. Dev. Lett. 45, 2043 (1980).

3.2.9 R. Haight, W.M. Gibson, T. Narusawa, L.C. Feldman, J. Vac. Sci. Technol. 18, 1973 (1982).

3.2.10 L.C. Feldman, P.J. Silverman, I. Stensgaard, Nucl. Instrum. Methods 168, 589 (1980).

3.3.1. Y. Nishi, Jap. J. Appl. Phys. 10, 52 (1971); ibid, 5, 333 (1965).

3.3.2. A.G. Revesz, B. Goldstein, Surface Sci. 14, 361 (1969).

3.3.3. A. Stesmans, J. Braet, J. Witters, R.F. Dekersmaecker, Surface Sci. 141, 255 (1984).

3.3.4. P.J. Caplan, J.N. Helbert, B.E. Wagner, E.H. Poindexter, Surface Sci. 54 33 (1976).

3.3.5. P.J. Caplan, E.H. Poindexter, B.E. Deal, R.R. Razouk, J. Appl. Phys. 50, 5847 (1979); in "The Physics of MOS Insulators," Eds. G. Lucovsky, S.T. Pantelides, F.L. Galeener, Pergamon Press, New York (1980), p. 306.

3.3.6. E.H. Poindexter, P.J. Caplan, B.E. Deal, R.R. Razauk, J. Appl. Phys. 52, 879 (1981).

3.3.7. E.H. Poindexter, P.J. Caplan, Progress in Surface Sci. 14, 201 (1983).

3.3.8. E.H. Poindexter, P.J. Caplan, in "Insulating Films on Semiconductors," Eds. M. Schultz, G. Pensl, Springer-Verlag, Berlin (1981), p. 150.

3.3.9. K.L. Brower, Appl. Phys. Lett. 43, 1111 (1983).

3.3.10. K.L. Brower, P.M. Lenahan, P.V. Dressendorfer, Appl. Phys. Lett. 41, 251 (1982).

3.3.11. C. Brunstrom, C. Svensson, Solid State Commun. 37, 399 (1981).

3.3.12. P.M. Lenahan, P.V. Dressendorfer, J. Appl. Phys. 55, 3495 (1984).

3.3.13. P.M. Lenahan, K.L. Brower, P.V. Dressendorfer, W.C. Johnson, IEEE Trans. Nucl. Sci., NS-28, 4105 (1981).

3.3.14. P.M. Lenahan, P.V. Dressendorfer, Appl. Phys. Lett. 41, 542 (1982).

3.3.15. P.M. Lenahan, P.V. Dressendorfer, Appl. Phys. Lett. 44, 96 (1984).

3.3.16. K.L. Brower, Appl. Phys. Lett.

3.3.17. K.L. Brower, private communication.

3.4.1 R.M.A. Azzam, N.M. Bashara, "Ellipsometry and Polarized Light," North-Holland, Amsterdam, 1976.

3.4.2 R.J. Archer, J. Electrochem. Soc., 104, 613 (1957).

3.4.3 R.J. Archer, J. Opt. Soc. Am. 52, 970 (1962).

3.4.4 Y.J. Van der Meulen, C.H. Osburn, J.F. Ziegler, J. Electrochem. Soc. 120, 284 (1975).

3.4.5 B.H. Claussen, M. Flower, J. Electrochem. Soc. 110, 983 (1963).

3.4.6 E.A. Taft, L.F. Cordes, J. Electrochem. Soc. 126, 131 (1979).

3.4.7 D.E. Aspnes, J.B. Theeten, J. Electrochem. Soc. 127, 1359 (1982).

3.4.8 J.H. Mazur, R. Gronsky, J. Washburn, in Microscopy of Semiconducting Materials, Inst. Phys. Conf. Ser. No. 67: Section 2, p. 77 (1983).

3.4.9 C.A. Fenstermaker, F.L. McCrackin, Surface Sci. 16, 85 (1969).

3.4.10 R.M. Pashley, Surface Sci. 71, 139 (1978).

3.5.1 J.S. Johannessen, W.E. Spicer, Y.E. Strausser, J. Vac. Sci. Technol. 13, 849 (1976).

3.5.2 J.S. Johannessen, W.E. Spicer, Y.E. Strausser, J. Appl. Phys. 47, 3028 (1976).

3.5.3 C.R. Helms, C.M. Garner, J. Miller, I. Lindau, S. Schwarz, W. Spicer, Proceedings of the Seventh International Congress and Third International Conference on Solid Surfaces (Dobrozemsk, Vienna, 1977) vol. 3, p. 2241.

3.5.4 C.R. Helms, W.E. Spicer, N.M. Johnson, Solid State Commun. 25, 673 (1978).

3.5.5 C.R. Helms, N.M. Johnson, S.A. Schwarz, W.E. Spicer, "The Physics of $SiO_2$ and its Interfaces," S.T. Pantelides, Ed., Pergamon Press, New York (1978), p. 363.

3.5.6 J.F. Wager, C.H. Hilmsen, ibid., p. 373.

3.5.7 C.R. Helms, Y.E. Strausser, W.E. Spicer, Appl. Phys. Lett. 33, 767 (1978).

3.5.8 C.R. Helms, N.M. Johnson, S.A. Schwarz, W.E. Spicer, J. Appl. Phys. 50, 7007 (1979).

3.5.9 J.F. Wager, C.W. Wilmsen, J. Appl. Phys. 50, 874 (1979).

3.5.10 O.L. Krivanek, D.C. Tsui, T.T. Sheng, A. Kagmar, in "The Physics of $SiO_2$ and Its Interfaces," S.T. Pantelides, Ed., Pergamon Press, New York (1978), p. 356.

3.5.11 O.L. Krivanek, J.M. Mazur, Appl. Phys. Lett. 37, 392 (1980).

3.6.1 E.H. Nicolien, J.R. Brews, "MOS (Metal-Oxide-Semiconductor) Physics Technology," J. Wiley & Sons, New York, 1982.

3.6.2 Y.C. Cheng, E.A. Sullivan, Surface Sci. 34, 717 (1973).

3.6.3 Y.C. Cheng, E.A. Sullivan, J. Appl. Phys. 44, 923 (1973).

3.6.4 Y.C. Cheng, Japan J. Appl. Phys. Supl. 2, Pt. 2, p. 363 (1972).

3.6.5 A. Harstein, T.H. Ning, A.B. Fowler, Surface Sci. 58, 178 (1976).

3.6.6 C.T. Sah, T.H. Ning, L.L. Tschopp, Surface Sci. 32, 361 (1972).

3.6.7 R.E. Prange, T.W. Nee, Phys. Rev. 168, 779 (1968).

3.6.8 S.C. Sun, J.D. Plummer, IEEE J. Solid-State Circuits SC-12, 562 (1980).

3.6.9 O.L. Krivanek, J.H. Mazur, Appl. Phys. Lett. 37, 392 (1980).

3.6.10 J.H. Mazur, R. Gronsky, J. Washburn, in Microscopy of Semiconducting Materials, Inst. Phys. Conference Proc. Series 67, 77 (1983).

3.6.11 S.M. Goodnick, R.G. Gunn, J.R. Sites, D.K. Ferry, C.W. Wilmsen, D. Fathy, D.L. Krivanek, J. Vac. Sci. Technol. B1, 803 (1983).

3.6.12 Z. Liliental, O.L. Krivanek, S.M. Goodnick, C.W. Wilmsen, Mat. Res. Symp. Proc. 37, (1985).

3.6.13 P.O. Hahn, M. Henzler, J. Appl. Phys. 52, 4122 (1981).

3.6.14 P.O. Hahn, M. Henzler, in "Insulating Films on Semiconductors," M. Schulz, G. Pens, Eds., Springer-Verlag, Berlin, 1981, p. 26.

3.6.15 P.O. Hahn, M. Henzler, J. Appl. Phys. 54, 6492 (1983).

3.6.16 P.O. Hahn, M. Henzler, J. Vac. Sci. Technol. A2, 574 (1984).

# 4. EXPERIMENTAL TECHNIQUES

## 4.1 Transmission Electron Microscopy

The process of image formation in an electron microscope can be considered as consisting of four stages.

In the first stage, an electron beam (described by a wave function) is formed and focused on a specimen. In the second stage the electron beam (a wave function of electrons) is modified by interaction with the crystal potential of the specimen and can be described by the transmission function $q(x,y)$ at the exit face of the specimen. These modifications can be described by the dynamical theory of electron diffraction [4.1,4.2]. In the third stage, the electron beam (wave) which exits from the specimen is further modified by passing through the imaging system of the electron microscope. The modifications to the electron beam result from aberrations of the lenses and instrumental instabilities and can be described by contrast transfer theory [4.1-4.5]. In the fourth and final stage, the intensity of the electron beam is registered in the electron image (micrograph).

Structure determination from the electron micrograph corresponds to retracing the stages 2, 3, 4 in the opposite direction and finding the (crystal ) potential corresponding to the specimen structure.

## 4.2 TEM Image Formation

The imaging theory used to describe the operation of the microscope originated from the ideas of Abbe, published in 1873, and is reviewed in many excellent texts on optics and transmission

electron microscopy [4.1-4.6]. Figure 4.1A shows a geometric optics ray diagram used to suggest the imaging process according to the Abbe theory. The object described by the transmission function Q(x,y) is illuminated by a parallel beam of radiation, and imaged by a lens with a focal length, f. All radiation scattered at a point A in the specimen plane is brought to focus at point A' in the image plane. The image of the object is inverted and magnified by a factor M (the ratio of distances of the image plane and the specimen plane from the objective lens). The other interesting property of the system is that all radiation scattered through angle $\phi$ is brought to a focus at one point in the back-focal plane. This is equivalent to interference at a point at infinity, and therefore the amplitude distribution corresponds to that of the Fraunhofer diffraction pattern given by the Fourier transform of $Q(\tilde{g}) = F\{q(\tilde{r})\}$ of the transmission function $q(\tilde{r})$, where $\tilde{g} = [u = (\sin\phi_x)/\lambda,\ v = (\sin\phi_y)/\lambda]$ and for small $\phi$ corresponding to $\tilde{g} = [u = \phi/\lambda = x/f\lambda,\ v = \phi/\lambda = y/f\lambda]$. Alternatively, the image formed in the image plane may be considered as an interference pattern of the radiation in the back-focal plane. Because the image plane is effectively at infinity, the amplitude distribution in the image is given by the Fourier transform of the wave amplitude in the back-focal plane. Such a description allows us to account for the imperfection of the lens and its finite aperture in reproducing the object transmission function on the image plane by modification of the amplitude and phase of the distribution in the back-focal plane. These modifications have to be applied to each point on the back-focal plane.

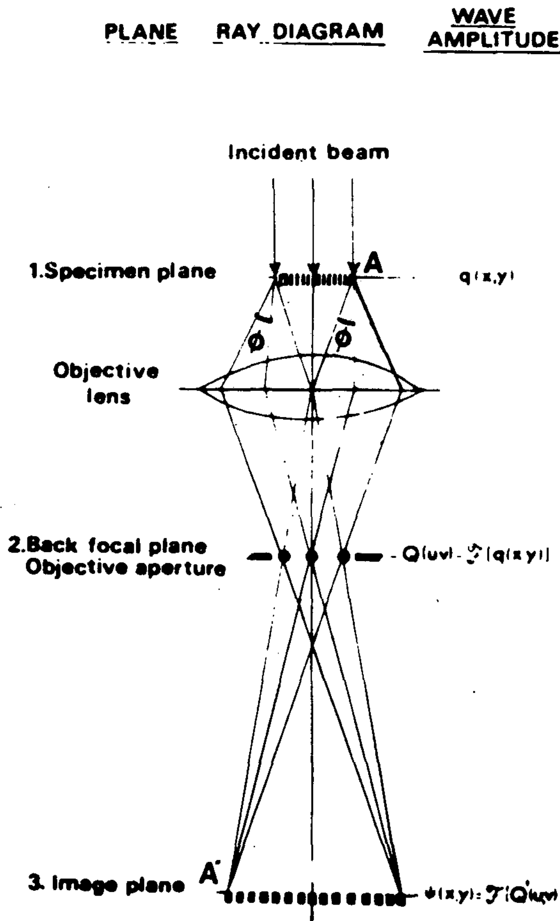


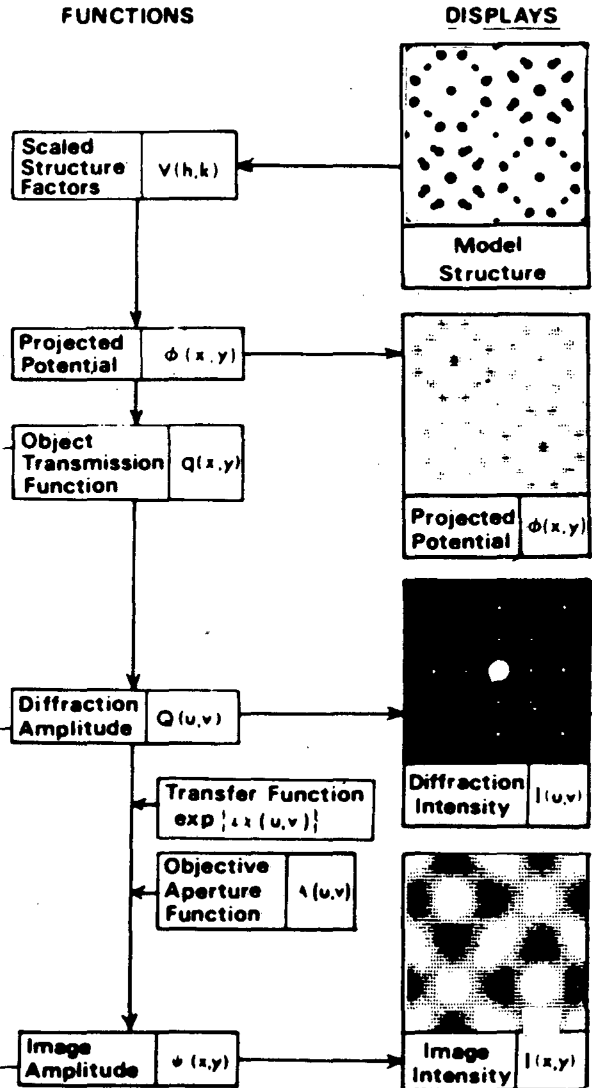


XBL 8312-4698A

Fig. 4.1. a) Schematic representation of the imaging process in the electron microscope;
b) Mathematical description of the computer simulation of the imaging process in the electron microscope.
(Courtesy of M.A. O'Keefe)

This corresponds to direct multiplication of $Q(\underset{\sim}{g})$, the Fourier transformed transmission function $Q(\underset{\sim}{r})$, by the appropriate contrast transfer function $T(\underset{\sim}{g})$ accounting for the modifications due to the finite objective lens aperture size, defocus, aberrations and instabilities of the electron-optical system.

The wave amplitude in the image plane is given by the Fourier transform

$$\psi'(r) = F[Q(\underset{\sim}{g})T(\underset{\sim}{g})] = q(\underset{\sim}{r})*t(\underset{\sim}{r}) \qquad (4.1)$$

where $q(\underset{\sim}{r})*t(\underset{\sim}{r})$ represents a convolution of the object transmission function with a spread function $t(\underset{\sim}{r})$. The intensity registered on the recording medium is proportional to

$$I(\underset{\sim}{r}) = |\psi'(\underset{\sim}{r})|^2 \qquad (4.2)$$

## 4.3 The Relationship Between the High Resolution Image and the Specimen Structure

In order to determine how the high resolution image relates to the structure of the specimen one needs to know how the planar wave amplitude is modified by the specimen, or more precisely, by the potential of the atoms in the specimen. The physical optics formulation [4.1, 4.3] assumes that the incident wave amplitude $\psi_0(x,y)$ is modified by the object transmission function $q(x,y)$ in such a way that the wave amplitude at the exit face of the specimen is given by the equation

$$\psi(x,y) = \psi_0(x,y)\, q(x,y) = Q(\underset{\sim}{r}) \tag{4.3}$$

For a sufficiently thin object, the transmission function represents the change of phase of the electron wave during propagation through a potential field of a specimen and is given by

$$q(\underset{\sim}{r}) = q(x,y) = \exp\{-i\sigma\phi(x,y)\} \tag{4.4}$$

where $\phi(\underset{\sim}{r}) = \phi(x,y) = \int_0^z \phi(x,y,z)\, dz$ is a projected potential of the specimen, $\sigma = \pi/\lambda E_0$ and $E_0$ is the accelerating voltage. For $\sigma\phi(x,y) \ll 1$, the so-called weak phase object approximation (equivalent to the single scattering approximation [4.1]) is valid, with

$$q(x,y) = \exp\{-i\sigma\phi(x,y)\} \approx 1 - i\sigma\phi(x,y) \tag{4.5}$$

For the wave function in the back focal plane this gives

$$\begin{aligned} Q(\underset{\sim}{g}) &= [\delta(\underset{\sim}{g}) - i\sigma\phi(\underset{\sim}{g})]\, T(\underset{\sim}{g}) \\ &= [\delta(\underset{\sim}{g}) - i\sigma(\phi(\underset{\sim}{g})]\, A_{eff}(\underset{\sim}{g})\exp\{-iX(\underset{\sim}{g})\} \end{aligned} \tag{4.6}$$

and for the wave function in the image plane

$$\psi(\underset{\sim}{r}) = [1 - i\sigma\phi(\underset{\sim}{r})] * [c(\underset{\sim}{r}) + is(\underset{\sim}{r})] \tag{4.7}$$

Here $c(\underset{\sim}{r})$ and $s(\underset{\sim}{r})$ are the Fourier transforms of $A_{eff}(\underset{\sim}{g}) \cos X(\underset{\sim}{g})$ and $A_{eff}(\underset{\sim}{g}) \sin X(\underset{\sim}{g})$ respectively. (The function $A_{eff}(\underset{\sim}{g})$ represents an effective aperture function, and will be discussed later.)

Therefore registered intensity after neglecting second order terms in $\sigma\phi(r)$ is as follows

$$I(\underset{\sim}{r}) = 1 + 2\sigma\phi(\underset{\sim}{r}) * s(\underset{\sim}{r}) \tag{4.8}$$

where the second term represents convolution of a projected potential with a smearing function $s(\underset{\sim}{r})$ corresponding to the contrast transfer function $T(\underset{\sim}{g}) = A_{eff}(\underset{\sim}{g}) \sin X(\underset{\sim}{g})$ in the back focal plane of the objective lens. Therefore the image can be considered to be produced by a system with the contrast transfer function

$$T(\underset{\sim}{g}) = A_{eff}(\underset{\sim}{g}) \sin X(\underset{\sim}{g}) \quad . \tag{4.9}$$

The phase distortion function X(g) is given [4.2] by

$$X(\underset{\sim}{g}) = \pi \Delta f g^2 + \pi C_s \lambda^3 g^4/2 \tag{4.10}$$

which takes into account changes of phase due to spherical aberration and defocus of the lens. The function $\sin X(\underset{\sim}{g})$ has an oscillating character and its value varies between -1 and +1. However it exhibits broad passbands or contrast transfer intervals for specific values of focus given by [4.4]

$$\Delta f_n = -[C_s \lambda (8n + 3)/2]^{1/2} \tag{4.11}$$

This is illustrated by curves marked "a" in the Figs. 4.2-4.5, calculated for defocus values +66.0, -66.0, -128.5 and 168.8 nm with the last three values of defocus corresponding to n = 0,1,2 for

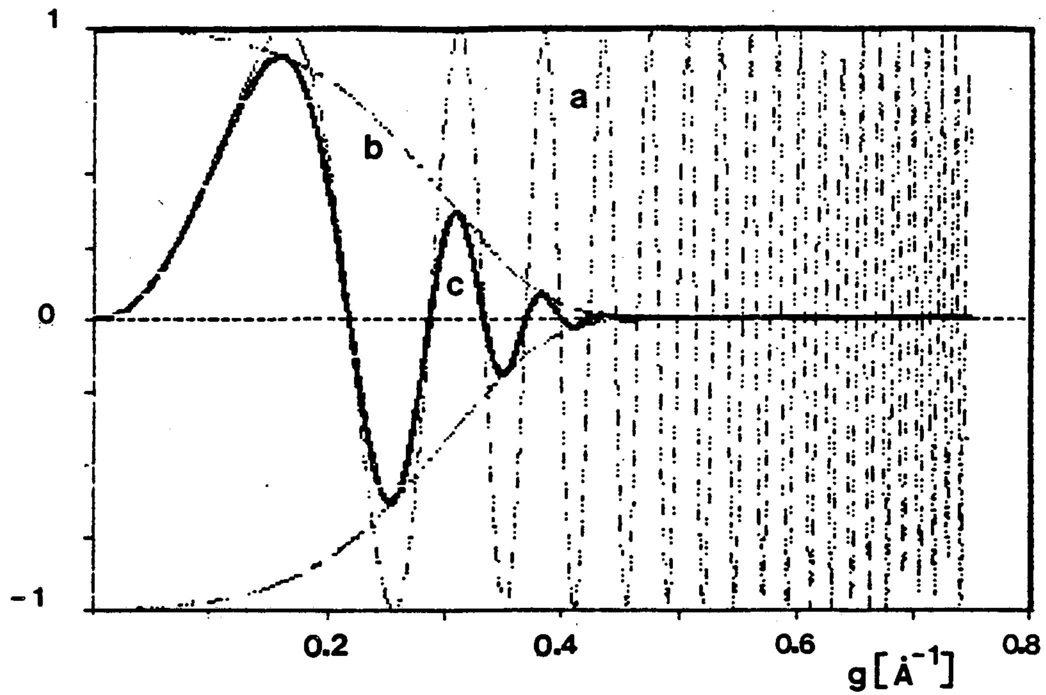


Fig. 4.2. Plot of the (a) $C_t(g)$, (b) $E_t(g)E_s(g)$, and (c) $E_t(g)E_s(g)C_t(g)$ functions for an electron microscope, JEOL 200 CX, with a high resolution pole piece $C_s = 1.2$ mm and for $V_0 = 200$ kV, $\delta = 5.0$ nm, $\alpha = 0.5$ mrad, $\Delta f = 66$ nm.

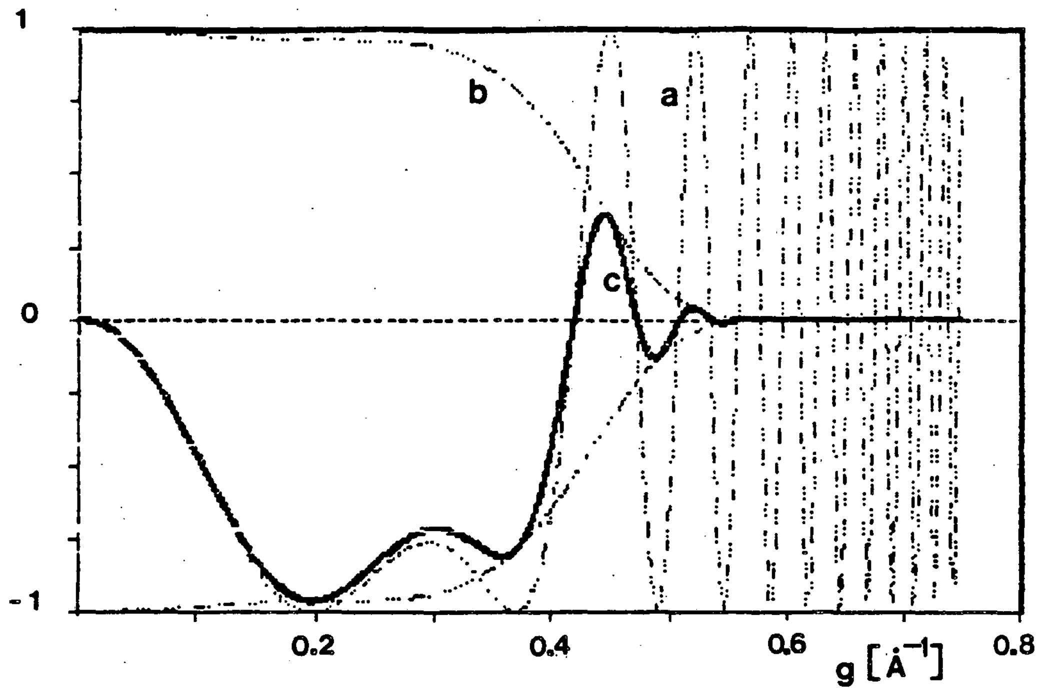


Fig. 4.3. Plot of the (a) $C_t(g)$, (b) $E_t(g)E_s(g)$, and (c) $E_t(g)E_s(g)C_t(g)$ functions for an electron microscope, JEOL 200 CX, with a high resolution pole piece $C_s$ = 1.2 mm and for $V_0$ = 200 kV, $\delta$ = 5.0 nm, $\alpha$ = 0.5 mrad, $\Delta f$ = -66.0 nm (n = 0).

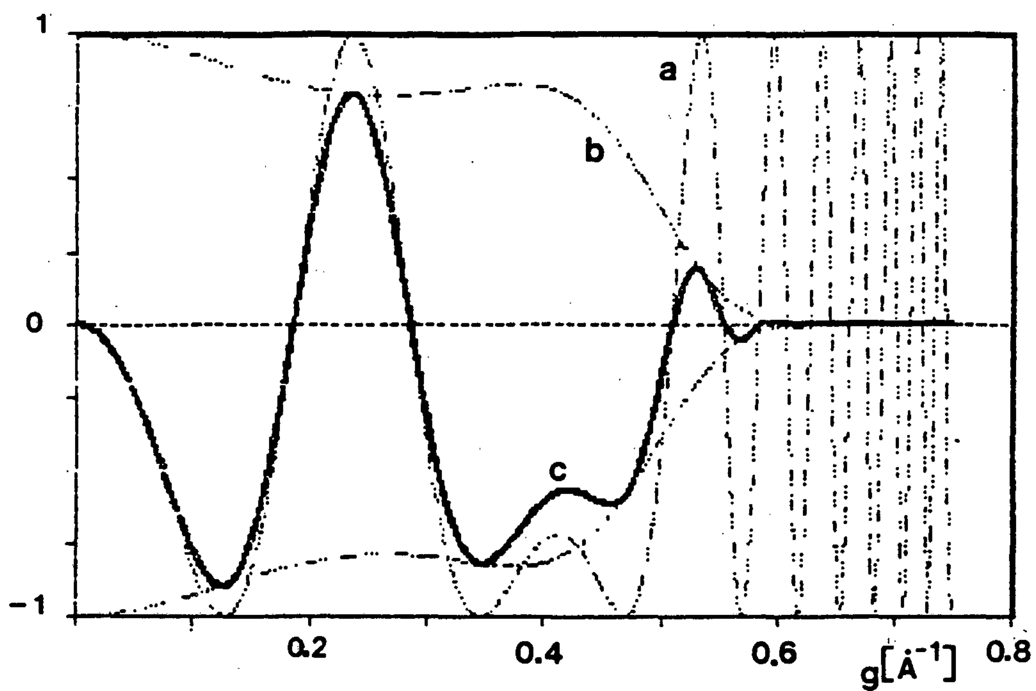


Fig. 4.4. Plot of the (a) $C_t(g)$, (b) $E_t(g)E_s(g)$, and (c) $E_t(g)E_s(g)C_t(g)$ functions for an electron microscope, JEOL 200 CX, with a high resolution pole piece $C_s$ = 1.2 mm and for $V_0$ = 200 kV, $\delta$ = 5.0 nm, $\alpha$ = 0.5 mrad, $\Delta f$ = -128.5 nm (n = 1).

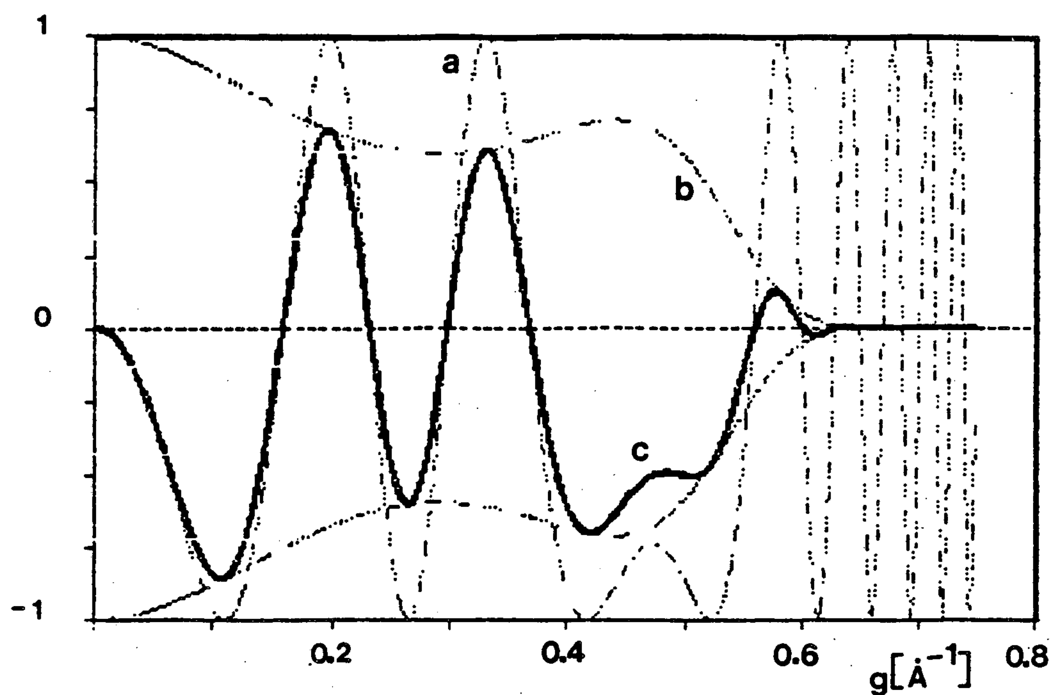


Fig. 4.5. Plot of the (a) $C_t(g)$, (b) $E_t(g)E_s(g)$, and (c) $E_t(g)E_s(g)C_t(g)$ functions for an electron microscope, JEOL 200 CX, with a high resolution pole piece $C_s = 1.2$ mm and for $V_0 = 200$ kV, $\delta = 5.0$ nm, $\alpha = 0.5$ mrad, $\Delta f = -168.8$ nm ($n = 2$).

$C_s$ = 1.2 mm and 200 kV accelerating voltage ($\lambda$ = 0.0025 nm). The width of the passbands, in particular the most important, that obtained for n = 0, the so-called Scherzer focus [4.9], increases as the $(C_s\lambda^3)^{1/4}$ decreases. This is illustrated in Fig. 4.6 for different values of parameters $C_s$,$\lambda$(kV) typical of modern microscopes. The Scherzer focus is the optimal choice of focus needed for straightforward image interpretation in terms of object structure. The first zero of sin $X(\underset{\sim}{g})$ at Scherzer focus, given by

$$d_{Sch} = 0.66\ C_s^{1/4}\lambda^{3/4} \quad , \tag{4.12}$$

defines point-to-point resolution of the electron microscope. The effective aperture function $A_{eff}(\underset{\sim}{g})$ in equation (4.6) can be considered, in the absence of astigmatism for the case of partially coherent illumination [4.4, 4.7, 4.8] as the product

$$A_{eff}(\underset{\sim}{g}) = A(\underset{\sim}{g})\ E_t(\underset{\sim}{g})\ E_s(\underset{\sim}{g}) \tag{4.13}$$

where $A(\underset{\sim}{g})$ is the physical aperture function, equal to 1 inside the aperture ($|\underset{\sim}{g}| = g_{max}$) and zero otherwise. The function $E_t(\underset{\sim}{g})$ is called a temporal envelope and describes the effect of temporal instabilities in the accelerating voltage and objective lens current, as well as the effect of energy distribution of electrons leaving the filament. It is given [4.4, 4.7, 4.8] by

$$E_t(\underset{\sim}{g}) = \exp\{-\pi^2\delta^2\lambda^2 g^4/2\} \tag{4.14}$$

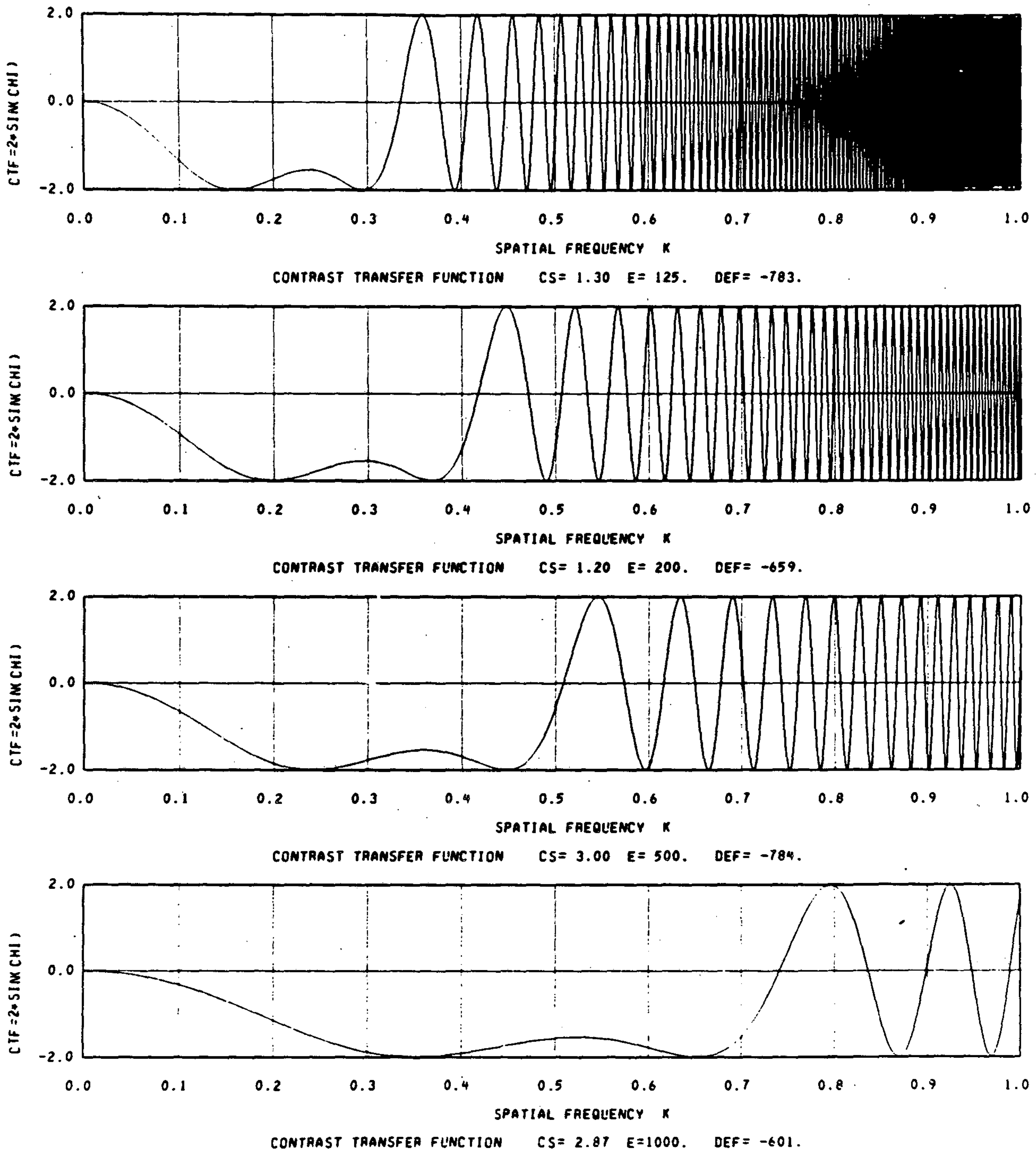


Fig. 4.6. The zeroth passband width of the 2*sin X(g) function at Scherzer focus (n = 0) for different accelerating voltages and spherical aberration coefficients characteristic of modern microscopes.

where

$$\delta = C_c Q = C_c \left[ \frac{\sigma^2(V_0)}{V_0^2} + \frac{4\sigma^2(I_0)}{I_0^2} + \frac{\sigma^2(E_0)}{E_0^2} \right]^{1/2} \tag{4.15}$$

and where $\sigma^2(V_0)$, $\sigma^2(I_0)$ are variances in the statistically independent fluctuations of the high voltage $V_0$ and the objective lens current $I_0$ respectively. The variance $\sigma^2(E_0)$ of the electrons' energy is related to the full width at half maximum height of the energy distribution of electrons leaving the filament and is equal to $\sigma^2(E_0) = \Delta E^2/2.345$. The proportionality factor $C_c$ corresponds to the chromatic aberration coefficient. The third function $E_s(g)$ is called a spatial envelope function and describes the effect of finite illumination aperture with semiangle $\alpha$. For a disc-shaped source with a reasonably sharp tail-off in intensity, this function can be expressed [4.8, 4.9, 4.4] as

$$E_s(\underset{\sim}{g}) = \frac{2J_1\ P(\underset{\sim}{g})}{P(\underset{\sim}{g})} \tag{4.16}$$

with

$$P(\underset{\sim}{g}) = 2\pi\alpha[C_s\lambda^2 g^3 - i\pi\delta^2\lambda g^3 + \Delta fg] \tag{4.17}$$

The effect of $E_t(\underset{\sim}{g})$ and $E_s(\underset{\sim}{g})$ is to dump a phase transfer function $C_t(\underset{\sim}{g}) = \sin X(\underset{\sim}{g})$. Curves marked "b" in Figs. 4.2-4.5 represent the $E_t(\underset{\sim}{g})E_s(\underset{\sim}{g})$ envelope product, while curves "c" represent the influence of envelopes on phase function $C_t(\underset{\sim}{g})$ and demonstrate a strong attenuation of all spatial frequencies especially in the regions of large

slope in $X(\underset{\sim}{g})$ beyond the passbands. This attenuation is a consequence of using a cone of illumination from an incoherent source for the specimen illumination.

The temporal instabilities of the microscope as represented by the temporal envelope $E_t(\underset{\sim}{g})$ determine the information resolution limit which is given by [4.4]

$$d = \left[\frac{\pi\lambda\delta}{2}\right]^{1/2} \tag{4.18}$$

Therefore these envelope functions describe a "soft aperture" the size of which is determined by instabilities of the high voltage, the objective lens current, the energy spread of accelerated electrons and the finite illuminating aperture. The effective aperture $A_{eff}(\underset{\sim}{g})$ therefore determines which part of the Fourier transformed wave amplitude in the back-focal plane will contribute to the image. For the Scherzer focus condition $\sin X(\underset{\sim}{g}) \simeq -1$ within the passband while $\cos X(\underset{\sim}{g}) \simeq 0$ and therefore

$$I(\underset{\sim}{r}) = 1 - 2\sigma\phi(\underset{\sim}{r}) * F\{A_{eff}(\underset{\sim}{g})\} \tag{4.19}$$

This represents a pure phase-contrast image which reflects <u>the projected potential for this focus and sufficiently thin specimens</u>. For these conditions the image appears in the form of dark dots in the region of high potential.

The situation becomes more complicated for thicker specimens especially those containing atoms of medium or high atomic number in which such simple interpretation is not possible. Unfortunately most

TEM specimens belong to this category and contrast from the defects can be understood only if an n-beam dynamical theory is considered. The details of these theories and the methods of computation are considered in a number of references [4.1, 4.4, 4.11-4.16]; however these are beyond the scope of this work.

## 4.4 Optical Diffraction

The assessment of electron-optical parameters of the electron microscope during imaging can be performed by means of optical diffraction of a coherent laser light from the high resolution electron micrograph [4.4, 4.17, 4.18]. The presence of any periodic arrangement of contrast in the image, for example lattice fringes, results in formation of a spot diffraction pattern. The separation D of the diffracted spot from the center of the screen is given by

$$D = \lambda L/d \qquad (4.20)$$

where $\lambda$ is the wavelength of the light, L is the diffraction camera length and d is a modulation period. Therefore periodicities in the optical diffraction pattern are identical to periodicities in the specimen, provided that one-to-one correspondence is preserved between periodicities in the electron micrograph and in the specimen. Because the electron micrograph can be considered as a weak phase object, then an amplitude in the diffraction pattern is given by Fourier transform of Eq. (4.8) as

$$Q(\underset{\sim}{g}) = \delta(\underset{\sim}{g}) - 2\sigma\phi(\underset{\sim}{g})\, A(\underset{\sim}{g}) \sin X(\underset{\sim}{g}) \qquad (4.21)$$

where $\underset{\sim}{g}$ represents a point in the optical diffraction pattern plane. The intensity in the optical diffraction pattern plane is obtained from Eq. (4.21) as:

$$I(\underset{\sim}{g}) = \delta(\underset{\sim}{g}) + 4\sigma^2 \phi^2(\underset{\sim}{g}) \sin^2 \chi(\underset{\sim}{g}) \, A^2(\underset{\sim}{g}) \qquad (4.22)$$

This formula indicates that for an amorphous secimen, containing all possible periodicities, a variety of electron microscope parameters can be determined from the optical micrograph. These include assessment of astigmatism, the spherical aberration coefficient, focus condition, specimen drift, and spatial and temporal coherence and the position of the voltage and current axis [4.4, 4.17]. Therefore we can determine how close to the Scherzer focus the high resolution images were obtained. This is particularly important if direct interpretation of the images in terms of the projected potential is considered. In the present study, optical diffractograms were used for this purpose.

REFERENCES - CHAPTER 4


4.1 J. M. Cowley, "Diffraction Physics," North-Holland/American Elsevier Publishing Company, New York, 1975.

4.2 L. Reimer, "Transmission Electron Microscopy," Springer Series in Optical Sciences vol. 36, Springer-Verlag, Berlin, 1984.

4.3 J. Cowley, in "Introduction to Analytical Electron Microscopy," J. J. Hren, J. I. Goldstein, D. C. Joy, Eds., Plenum Publishing Corporation, New York, 1979.

4.4 J. C. M. Spence, "Experimental High Resolution Electron Microscopy," Clarendon Press, Oxford, 1981.

4.5 K.-J. Hanszen, in Advances in Optical and Electron Microscopy, Vol. 4, R. Barer, V. E. Cosslett, Eds., Academic Press, NY (1971), p. 1.

4.6 M. Born, E. Wolf, "Principles of Optics," 5th edn., Pergamon, New York (1975).

4.7 J. Frank, Optik 38, 519 (1973).

4.8 P.L. Fejes, Acta Cryst. A33, 109 (1977).

4.9 O. Scherzer, J. Appl. Phys. 20, 20 (1949).

4.10 K. Ishizuka, Ultramicroscopy 5, 55 (1980).

4.11 J.M. Cowley, Acta Cryst. A29, 529 (1973).

4.12 P. Goodman, A.F. Moodie, Acta Cryst., A30, 280 (1974).

4.13 P.G. Self, M.A. O'Keefe, P.R. Buseck, A.E.C. Sparago, Ultramicroscopy 11, 35 (1983).

4.14 J.G. Allpress, J.V. Sanders, Acta Cryst. 6, 165 (1973).

4.15 J.G. Allpress, E.A. Hewat, A.F. Moodie, J.V. Sanders, Acta Cryst. A28, 528 (1972).

4.16 D.V. Dyck in "Diffraction and Imaging Techniques in Materials Science," North-Holland, Amsterdam (1978), p. 355.

4.17 O.L. Krivanek, Ph.D. thesis, Cambridge University, 1975.

4.18 R. Gronsky, in Treatise on Materials Science and Technology: Experimental Techniques, 19B, Academic Press, New York (1985), p. 325.

# 5. MATERIAL

## 5.1 Choice of Material

The silicon wafers used in this study were obtained from Czochralski (CZ) grown, p-type boron doped Si ingots. The concentration of boron was $8.0 \times 10^{14}$ to $1.5 \times 10^{15}$ [atoms $cm^{-3}$] corresponding to resistivities of 17 to 7 [$\Omega$ cm] respectively. Wafers with exact (111), (100) and near exact (111)2°[11$\bar{2}$], (111)3°[1$\bar{1}$0], (100)2°[011] Si surfaces were used for oxidation. The convention of Miller indices for surfaces and crystallographic directions used in describing the results is shown in Fig. 5.1. The wafer surfaces had standard finishes typical of the electronics industry.

## 5.2 Wafer Cleaning Procedures and Oxidation

Cleaning procedures before oxidation are very important for the production of very high quality oxide layers used in electronic device processing, and techniques similar to those used industrially were used in this study. They varied depending on the integrated circuits (I.C.) laboratory at which the oxidation was performed.

The University of California, Berkeley (UCB) IC laboratory Si wafer cleaning procedures consisted of the following steps:

1. Boiling in trichloroethelene (TCE)
2. Boiling in acetone
3. Boiling in methanol
4. Rinsing in $H_2SO_4$ : $H_2O_2$ : $H_2O$ (5:1:1)
5. Rinsing in deionized $H_2O$ (D.I. $H_2O$)
6. Native oxide etching in $H_2O$ : HF (20:1)

# Material:

- **Czochralski grown Si, p-type, boron doped, $\rho$ = 3–17 $\Omega$ cm**
- **Orientations:**

**(111) imaged ∥ $[1\bar{1}0]$**

**(111)2° $[11\bar{2}]$ imaged ∥ $[110]$**

**(111)3° $[1\bar{1}0]$ imaged ∥ $[10\bar{1}]$**

**(001) imaged ∥ $[011]$**

**(100)2° $[01\bar{1}]$ imaged ∥ $[0\bar{1}1]$**

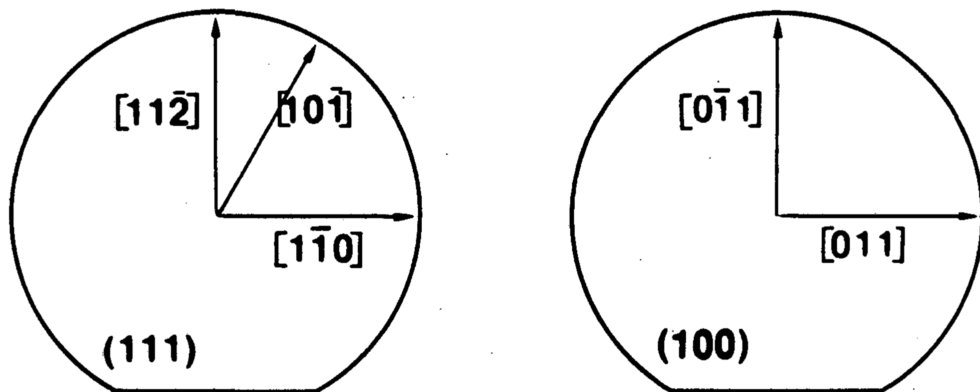


Fig. 5.1. The convention of Miller indices for surfaces and crystallographic direction used in the description of experimental results (Chapter 6).

7. Rinsing in D.I. $H_2O$

8. Blow drying in $N_2$

The Stanford University (SU) Si wafer cleaning procedures before oxidation consisted of the following steps:

1. Rinsing in $H_2O_2$ : $H_2O$ : $NH_4OH$ (5:1:1)
2. Rinsing in D.I. $H_2O$
3. Rinsing in $H_2O_2$ : $H_2O$ : HCl
4. Rinsing in D.I. $H_2O$
5. Native oxide etching $H_2O$ : HF (50:1)
6. Rinsing in D.I. $H_2O$
7. Blow drying in $N_2$

Immediately after cleaning, the Si wafers were transported to oxidation furnaces which were filled with flowing nitrogen (at UCB) or argon (at SU) gas. The wafers reached the oxidation zone of the furnace within 5 minutes of entry to the furnace. The end cap of the furnace was then quickly secured and the ambient gas was switched to dry $O_2$. Oxidation was then performed for the desired time, after which the wafers were removed within 2 minutes and placed into a nitrogen (UCB) or argon (SU) atmosphere.

5.3 TEM Specimen Preparation

The observations of the Si-$SiO_2$ interfaces were performed in cross-section, i.e. with the interfaces observed perpendicular to the thin film plane. The specimens were prepared using the following procedures (shown schematically in Fig. 5.2)

I. Determination of the desired imaging orientation of the cross-sections from back Laue x-ray diffraction.

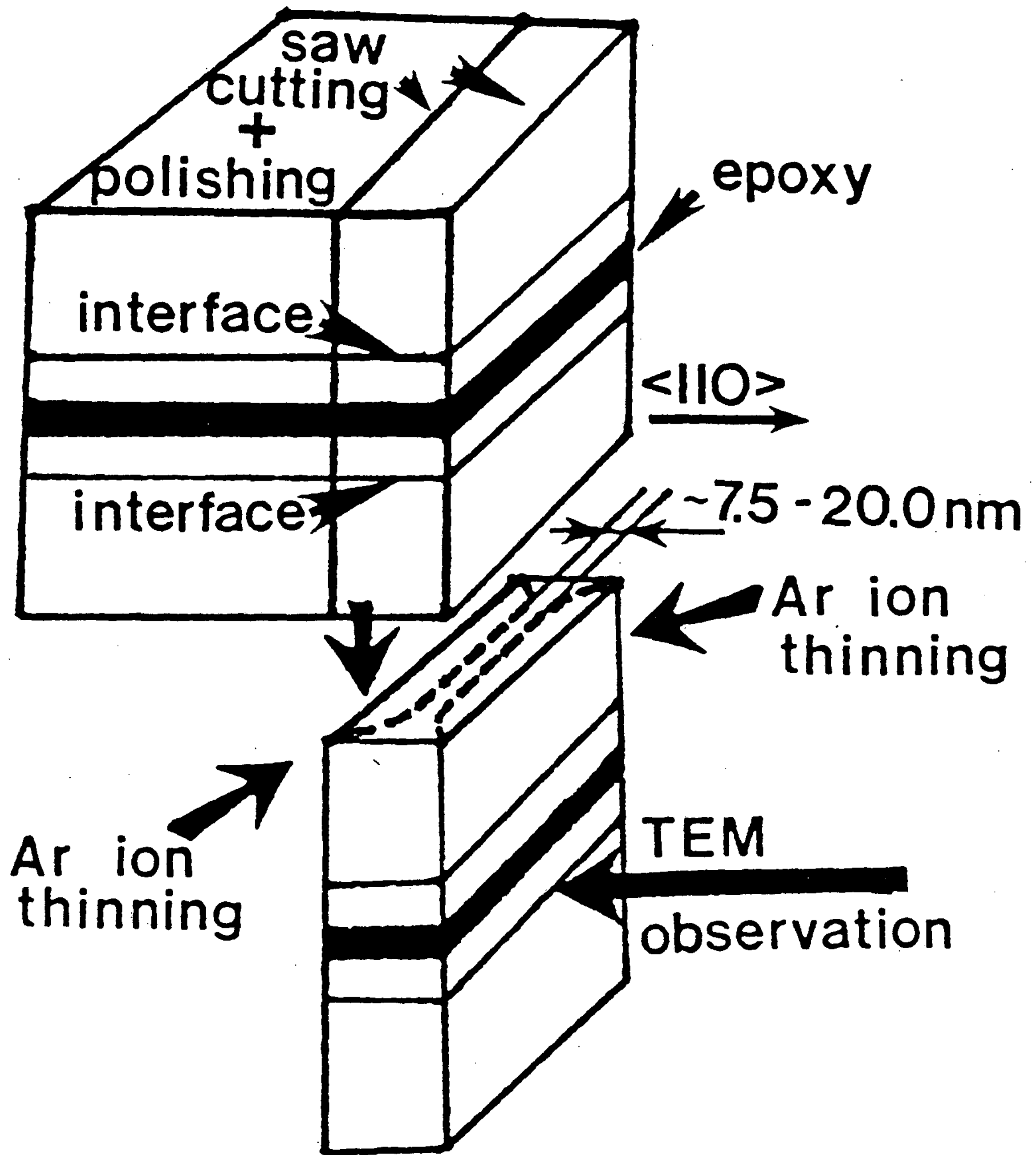


Fig. 5.2. Cross-sectional TEM specimen preparation.

II. Preparation of the sandwiches involving cutting and gluing together (with epoxy) small rectangles of specimens as shown in Fig. 5.2.

III. Slicing of the cross-section sandwiches with a wire or diamond saw.

IV. Grinding of one side of the cross-sections using 400, 600, 1200 grit SiC paper respectively.

V. Polishing of this side using 6, 1 and 1/4 μm diamond paste respectively (or polishing with alumina powder suspended in water).

VI. Repetition of the grinding and polishing on the other cross-section side.

VII. Cleaning of the cross-section to remove resin and other contaminants.

VIII. Argon ion thinning until perforation using a 6 kV beam at 15° incident angle with final thinning at 5 kV.

Consistently good TEM specimens were prepared using the following epoxy glues provided that the manufacturers' recommendations were followed:

M-Bond 610 adhesive (Measurement Group, N.C. 27611)
Epotek 20S conductive epoxy
Epotek 20E conductive epoxy
Araldite (CIBA-Geigy)
Devcon epoxy

During cutting, grinding and polishing, the specimens were fastened to glass plates or discs with an acetone-soluble "Crystal Bond" resin.

# 6. THE ATOMIC STRUCTURE OF $Si-SiO_2$ INTERFACES: EXPERIMENTAL RESULTS AND INTERPRETATION

The studies of the structure of the interface between thermally-grown oxide and silicon using transmission electron microscopy began with a paper reporting observation of the interface in cross-section [6.1.1]. This work demonstrated that at the level of 1 nm resolution the $Si-SiO_2$ interface is planar, and no crystalline Si islands or protrusions were present in thermally-grown $SiO_2$ near the interface. This was an indication that the model of $Si-SiO_2$ interfaces derived from the first Auger experiments discussed in Chapter 3.5 was invalid. Subsequent work [6.1.2] attempted to establish the nature of the transition layer and the interface structure formed by oxidation of (911) Si surfaces. No Si crystalline protrusions have been found. The narrow dark band near the interface interpreted preliminarily as a 1.0 nm $SiO_x$ transition layer was later considered [6.1.3] to be due to usage of a tilted illumination technique. Application of this technique results in other artifacts of imaging besides the presence of the dark band. These include fringes, extending into the oxide, for both 111 and 100 interfaces [6.1.3] as well as increased abruptness of the interface in comparison to axial illumination imaging [6.1.4]. Interpretation of the contrast features as $a_0/4$ = 0.135 nm steps at the interface is, therefore, questionable especially due to the fact that observations were performed on specimens with a thickness of 10.0-40.0 nm, with a microscope of the Siemens 102 type and thus required usage of the first or second passband (n equal to 1

or 2) instead of the directly interpretable zeroth passband at Scherzer focus.

A subsequent study of the ultrathin oxide on {100} Si [6.4.5] was the first in which axial illumination and a high brightness $LaB_6$ source was used for imaging. Figure 6.0.1 shows the abrupt amorphous to crystalline transition with surface roughness parameters: asperity $\Delta$ = 0.2 - 0.4 nm and correlation length L = 1.5 - 3.0 nm. It was suggested that the origin of the larger protrusions into the oxide was associated with the initial surface roughness before oxidation at 500°C at low oxygen partial pressure.

The observations of Pasemann and Pchelyakov [6.1.6] of the interfaces prepared by oxidation of the planar {110} Si TEM specimens thinned to perforation before oxidation shows the existence of {111} terraces and ledges. Unfortunately this study could not be straightforwardly interpreted because a tilted illumination technique was used, and, in addition, the oxidation procedure which was used resulted in a non edge-on geometry of the interface.

The results obtained during the course of the present thesis [6.1.7-6.1.10] provide, on the other hand, a more realistic assessment of the oxidation of a given surface of Si due to the fact that the planar geometry of the oxidation was preserved and therefore the interface could be observed edge-on. In addition a higher resolution [$d_{Sch}$ = 0.26 nm] microscope provided the means for obtaining images in axial illumination at conditions very close to the Scherzer focus. Therefore conditions pertained which made direct interpretation of the

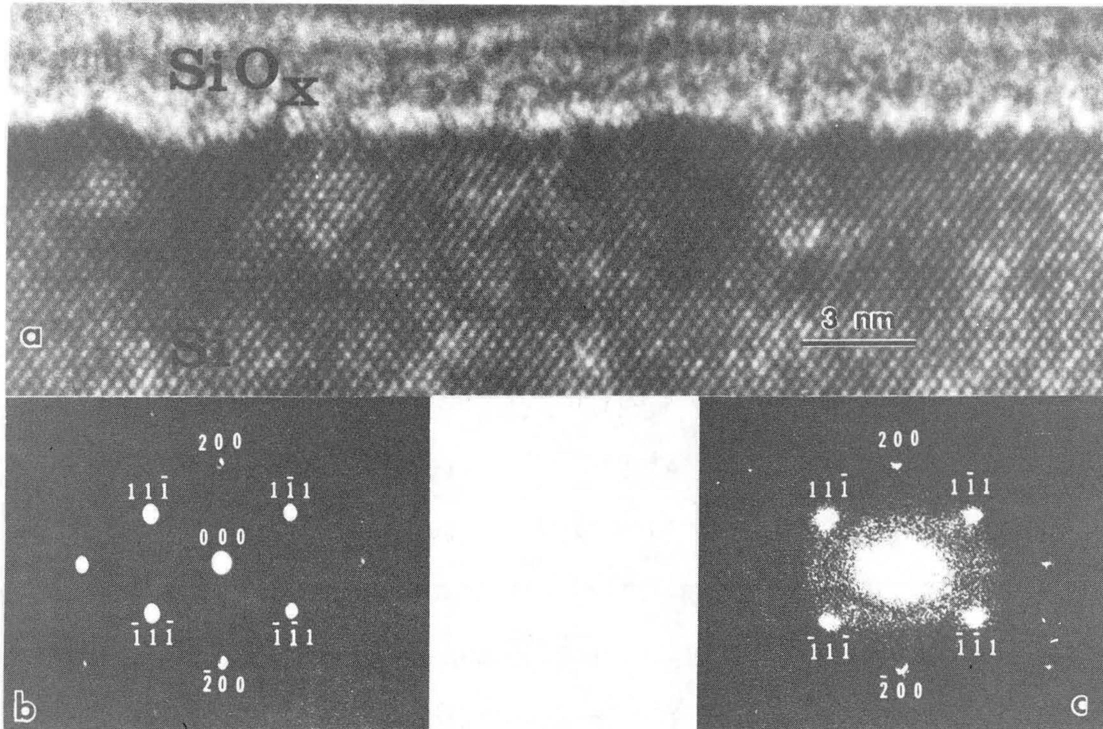


XBB 826-4952

Fig. 6.0.1. a) High resolution image of 3.0 nm thick native oxide on Si (axial illumination, Siemens 102).
b) SAD pattern
c) Optical diffractogram from the micrograph

images possible. The interfaces investigated in these studies encompassed a variety of oxidized Si surfaces.

The unifying goal behind the studies was to advance our understanding of the mechanism of oxidation. This mechanism ultimately determines the interface structure, chemistry and electronic properties. Knowledge of the oxidation mechanism would in turn provide the means for prediction of these interface properties, as a function of oxidation parameters. For this purpose the interfaces investigated included ones obtained by oxidation of the singular (low surface energy) {111} Si and {111} Si vicinal surfaces, as well as exact {100} (possibly singular) and vicinal {100} Si surfaces. The results of these studies are described later in this chapter.

Recently Goodnick et al. [6.1.11] compared the surface roughness parameters determined from TEM cross-sections with those from the mobility measurements. There was no direct agreement between correlation length and asperity determined from both techniques, unless it was assumed that a reduction in the values of these parameters obtained by TEM occurred due to projection along the specimen thickness. This reduced the discrepancy. The lack of agreement could be due, in part, to a slight deviation of [110] zone axis from the electron beam direction and to the relatively large thickness of the TEM specimen used for imaging (as can be seen from Figs. 4, 5 [6.1.11]).

More recently [6.1.12], correlation length and asperity determined by both these techniques (i.e., mobility and TEM measurement) were found to agree to within 30%, when the projection effect was taken

into account in high resolution images. That study, however, did not attempt to discuss the origin of the observed morphology.

The remainder of this chapter presents in detail the results of the current study.

High resolution images were obtained for <110> orientations of the Si substrate. The image of the columns of atoms obtained in a high resolution electron microscope along this direction is shown in Fig. 6.0.2a while the projection of the lattice is shown in Fig. 6.0.2b.

## 6.1 Oxidation of Singular (111) Si Surfaces

Oxidation of singular (111) surfaces of silicon at 1100°C in dry $O_2$ to an $SiO_2$ thickness of 100.0 nm resulted in the interface structures shown in Figs. 6.1.1, 6.1.2 and 6.1.3. The low magnification HREM image Fig. 6.1.1 demonstrates that the interface is flat over the large areas discernible in the TEM. The transition region between the amorphous $SiO_2$ and the Si substrate is very abrupt. Furthermore, careful observation reveals the existence of ledges only one {111} interplanar distance (.314 nm) high. This can be seen more clearly on the higher magnification micrograph shown in Fig. 6.1.3. The model of ledges indicating atomic positions at the interface is demonstrated in Fig. 6.1.4. The width of the terraces between positive and negative ledges varies and is dependent upon defocus as can be seen in Fig. 6.1.5. This suggests that the ledges may not extend through the whole TEM specimen thickness. A possible interpretation of such contrast changes is shown in Fig. 6.1.6. The upper part of the picture shows schematically the cross-sectional view of the

## <110> PROJECTION OF Si LATTICE

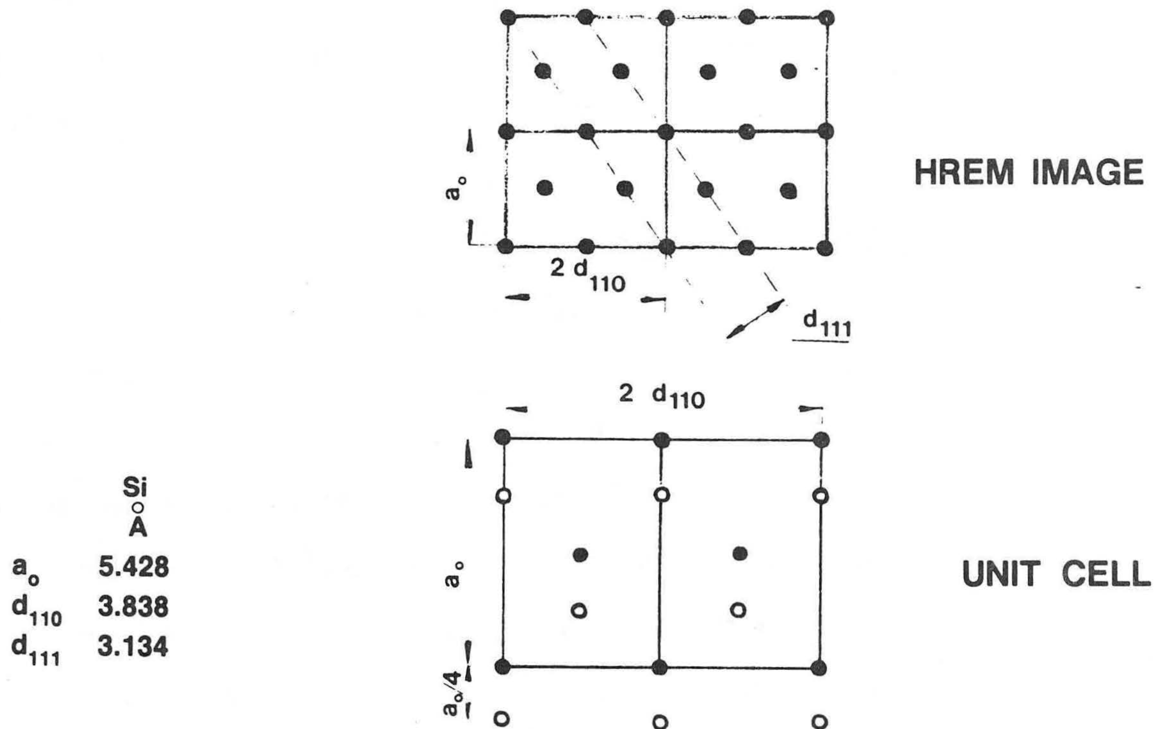


Fig. 6.0.2. a) Schematic representation of the high resolution image of the Si lattice observed along <110> crystallographic direction indicating distances between different lattice planes. Note that for thickness of specimen smaller than 15 nm and for Scherzer defocus the columns of atoms are black (A. Bourret, J. Desseaux, A. Renault, J. Micros. Spect. Elect. 2, 467 (1977)).

b) The <110> projection of the Si lattice.

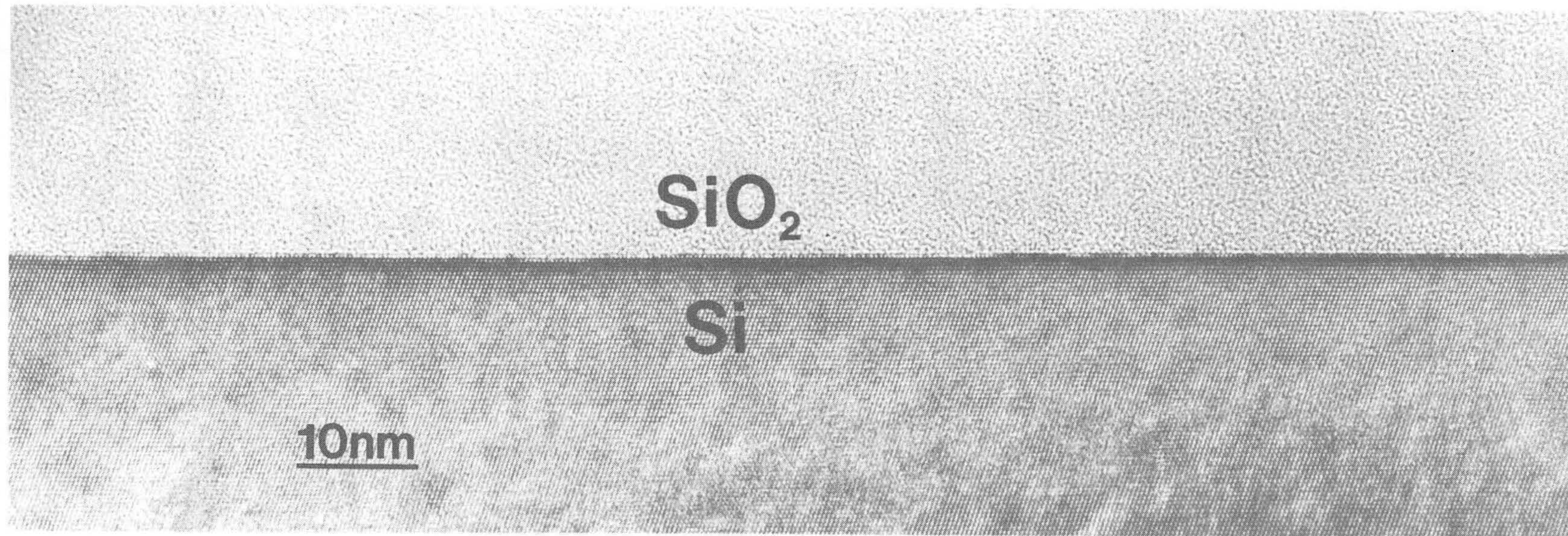




XBB 841-76

Fig. 6.1.1. Low magnification HREM image of the interface resulting from oxidation of a singular (111) Si surface in dry $O_2$ at 1100°C. The interface is planar within the area of 1500 Å observed in the image.

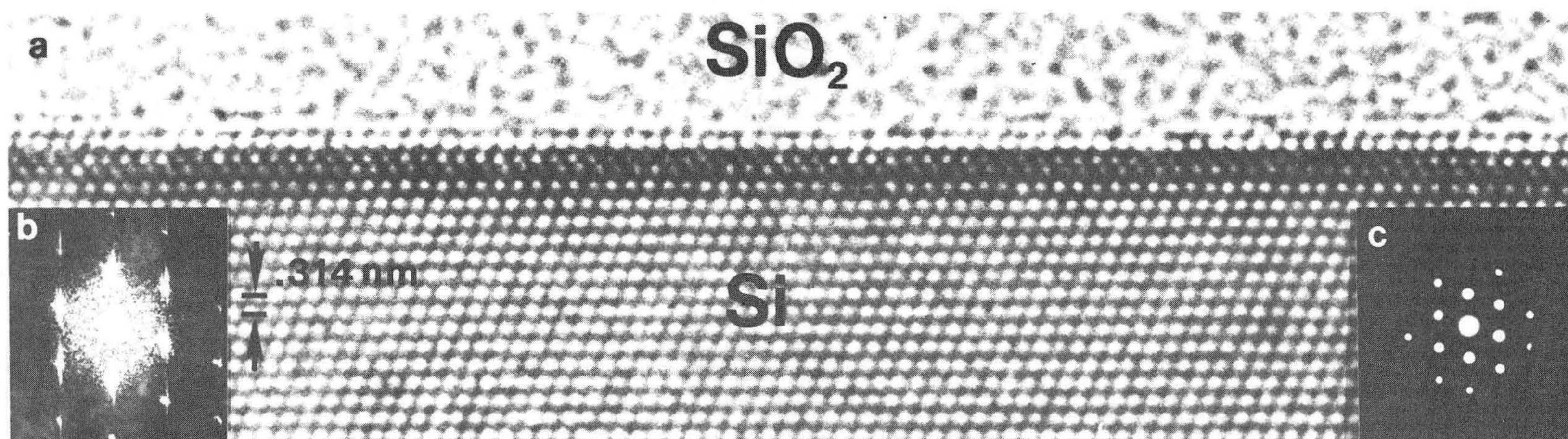


XBB 841-544-A

Fig. 6.1.2. Higher magnification image of the area shown in Fig. 6.1.1 demonstrating the presence of steps at the surface. Inset b is an optical diffractogram demonstrating imaging conditions near Scherzer focus, while inset c shows the SAD diffraction pattern.

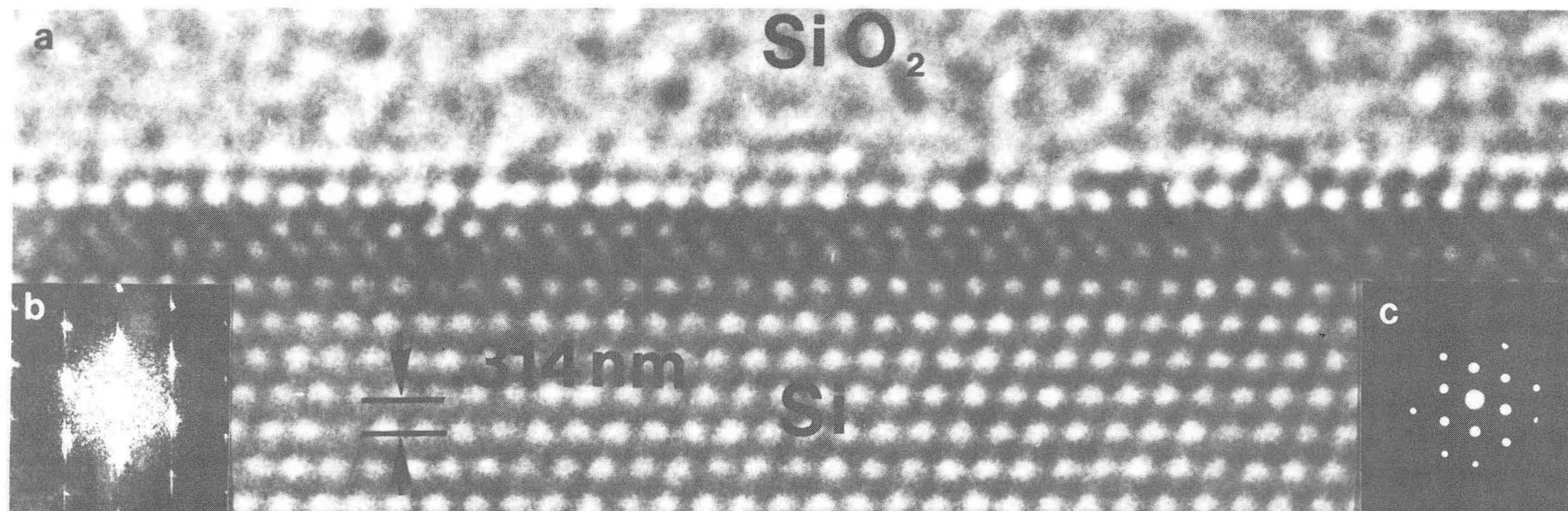


XBB 841-544-B

Fig. 6.1.3. High magnification high resolution image of the Si-$SiO_2$ interface shown in Figs. 6.1.1 and 6.1.2. Insets b,c are optical diffractogram and SAD pattern, respectively.

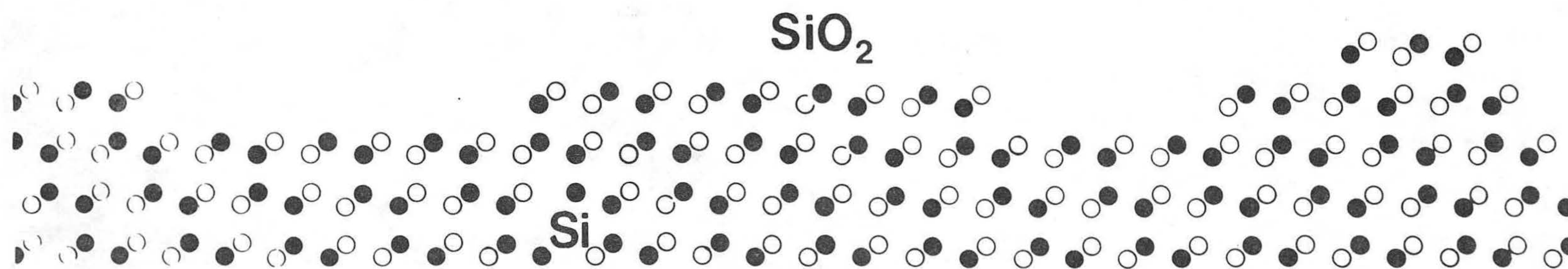


Fig. 6.1.4. A schematic representation of the images from Figs. 6.1.1-6.1.3, showing positions of atoms on the Si side of the interface.

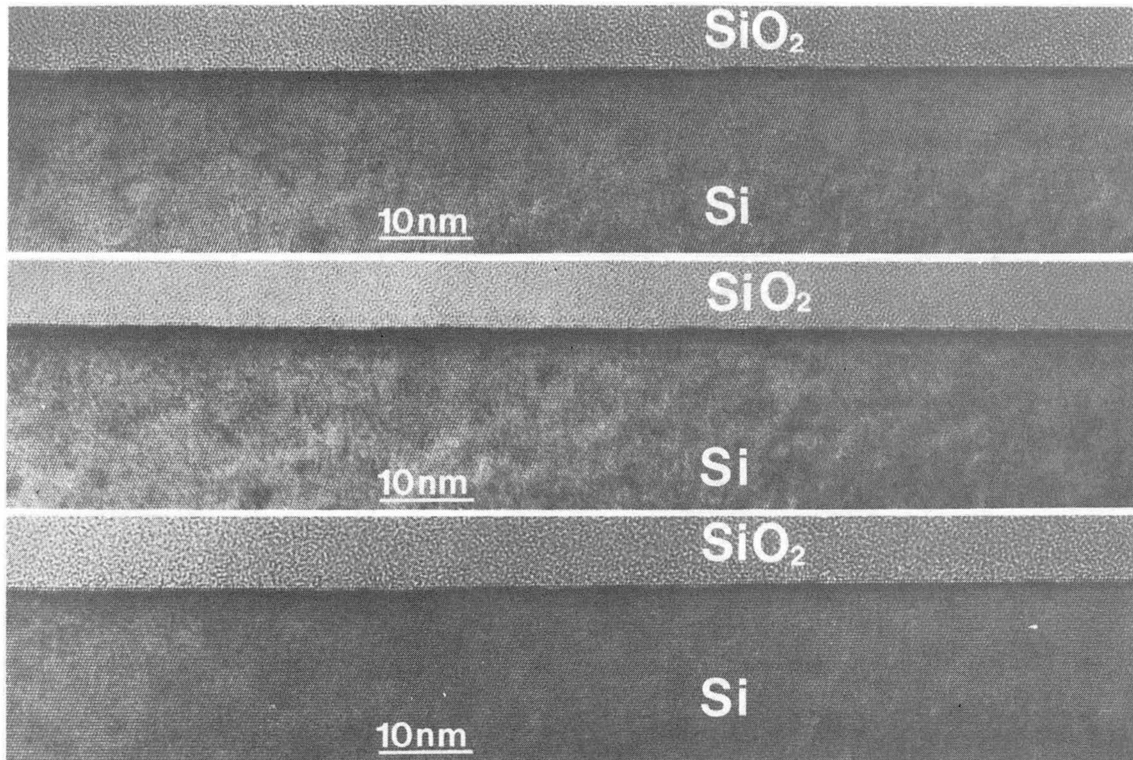


XBB 830-10017

Fig. 6.1.5. Three images from the through focus series of the same area of the Si-$SiO_2$ interface as in Fig. 6.1.1-6.1.3. The steps at the interface depend upon focus, thus indicating that they do not extend across the whole TEM specimen thickness.

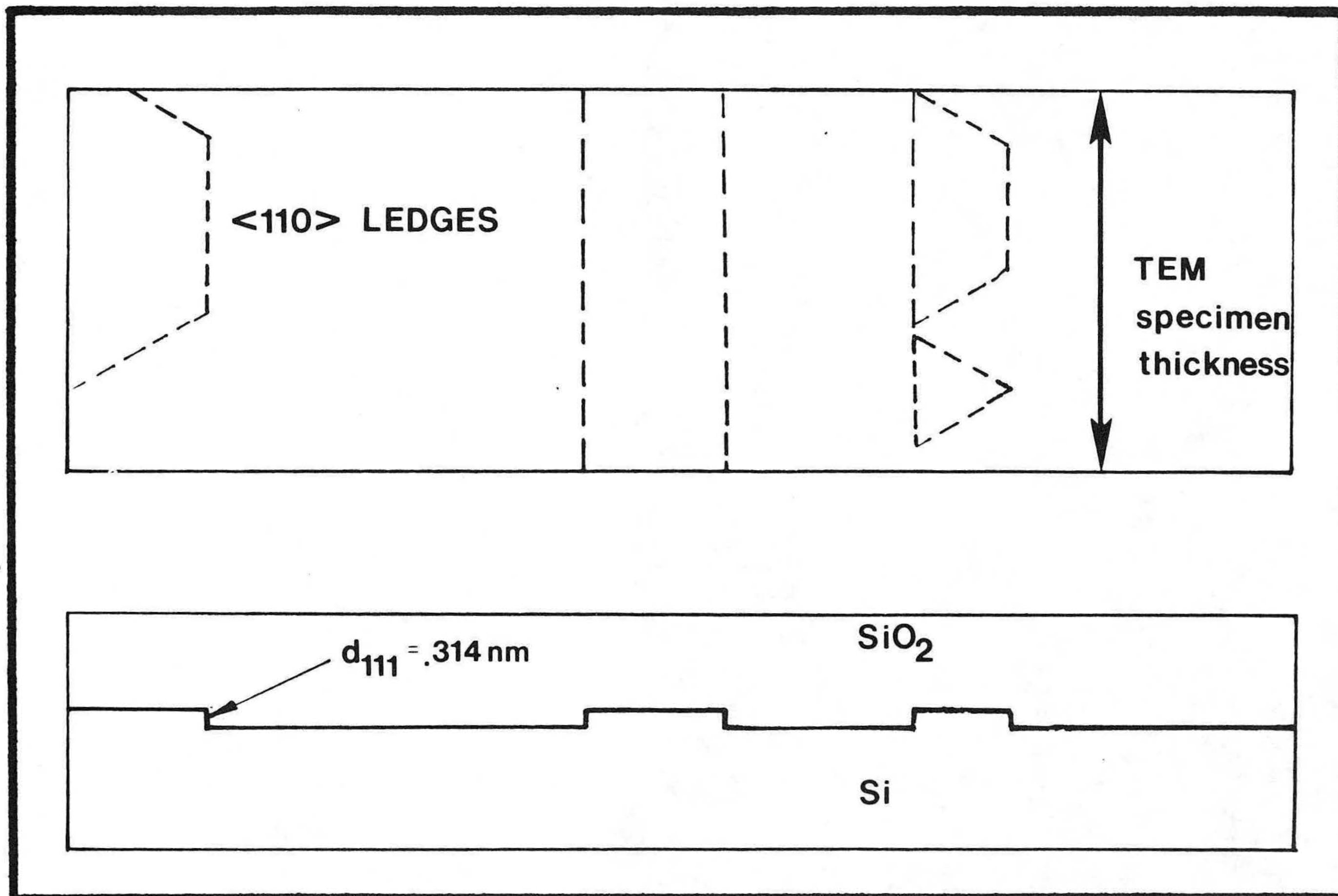


XBL 842-654

Fig. 6.1.6. Illustration of the possible step arrangements in the interface plane (top), and the resulting projection when the interface is observed in cross-section.

interface as observed in micrographs Fig. 6.1.1, 6.1.2, 6.1.3, with indicated projections of both sign ledges. The lower part of the figure shows traces of the intersection of such ledges with the terraces. It is assumed here that these traces correspond to low energy <110> directions in the silicon, similar to the case of free Si surfaces [6.1.13]. In addition, an interesting contrast feature exists at the Si-$SiO_2$ interface as can be seen in Fig. 6.1.3. Similar features were observed in a few specimens of {111} Si substrates oxidized at high temperature, but the features were absent in the native oxide on {111} Si interfaces. Therefore it is assumed that this contrast is not an artifact of imaging but a real structural defect. The symmetry of this defect indicates that it is a microtwin parallel to the surface, probably resulting from deformation twinning due to different expansion coefficients of $SiO_2$ and Si on cooling from oxidation to room temperature. The confirmation of this interpretation will require computer simulation of the image.

## 6.2 Oxidation of Vicinal (111)2°[11$\bar{2}$] Si Surfaces

Oxidation of vicinal (111)2°[11$\bar{2}$] Si surfaces was performed in dry $O_2$ at 1100°C. The oxide layer was 100.0 nm thick. The specimens were observed in cross-section along the [1$\bar{1}$0] zone axis lying in the interface plane where crystallographic directions were defined as in Fig. 5.1. A general view of the interface morphology is shown in Fig. 6.2.1. This low magnification HREM image demonstrates the planarity of the interface and the abruptness of the crystalline to glass transition over the whole of the areas observable in the TEM.

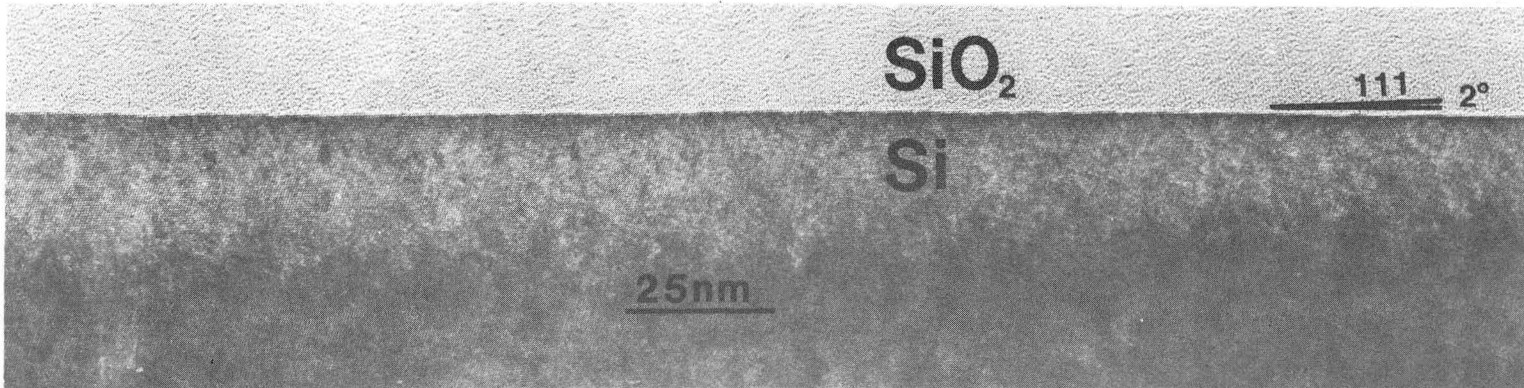


XBB 841-86

Fig. 6.2.1. Low magnification HREM image of a cross-section of oxide film grown on a (111)2°[11$\bar{2}$] Si surface.

Detailed analysis of the interface at higher magnification (Fig. 6.2.2 and Fig. 6.2.3) indicates the existence of predominantly one-sign ledges which are separated by atomically flat terraces. Additionally, both positive and negative sign ledges are observed on some of the structural terraces, that is those terraces which result from the inclination of the surfaces. The width of the terraces between positive and negative ledges varies similarly to those in singular (111) Si surfaces. The width of the structural terraces was observed to be 70-120 nm and the height of the ledges was 0.314 nm. This agrees well with the calculated terrace width of 9.0 nm assuming a ledge height of one {111} interplanar distance and a 2° deviation of the Si surface from the exact [111] orientation.

## 6.3 Oxidation of Vicinal (111)3°[1$\bar{1}$0] Si Surfaces

Oxidation of (111)3°[1$\bar{1}$0] Si surfaces was performed in dry $O_2$ at 1000°C. The thickness of the oxide was 100.0 nm. High resolution TEM observations were made on the specimens along [10$\bar{1}$] orientations of the Si substrate with crystallographic directions defined in Fig. 6.5.1. The structure of the interface is shown in Fig. 6.3.1. The Si substrate terminates abruptly at (111) planes separated by one {111} interplanar distance (0.314 nm) high ledges, where the transition to amorphous $SiO_2$ takes place. The width of the terraces was found to be exactly the same as that calculated for the geometry shown in Fig. 6.3.2 and equal to 6.0 nm. In contrast to the oxidized vicinal (111)2°[11$\bar{2}$] Si surfaces, only structural ledges of one sign are present at the Si-$SiO_2$ interface of oxidized vicinal (111)3°[1$\bar{1}$0] Si

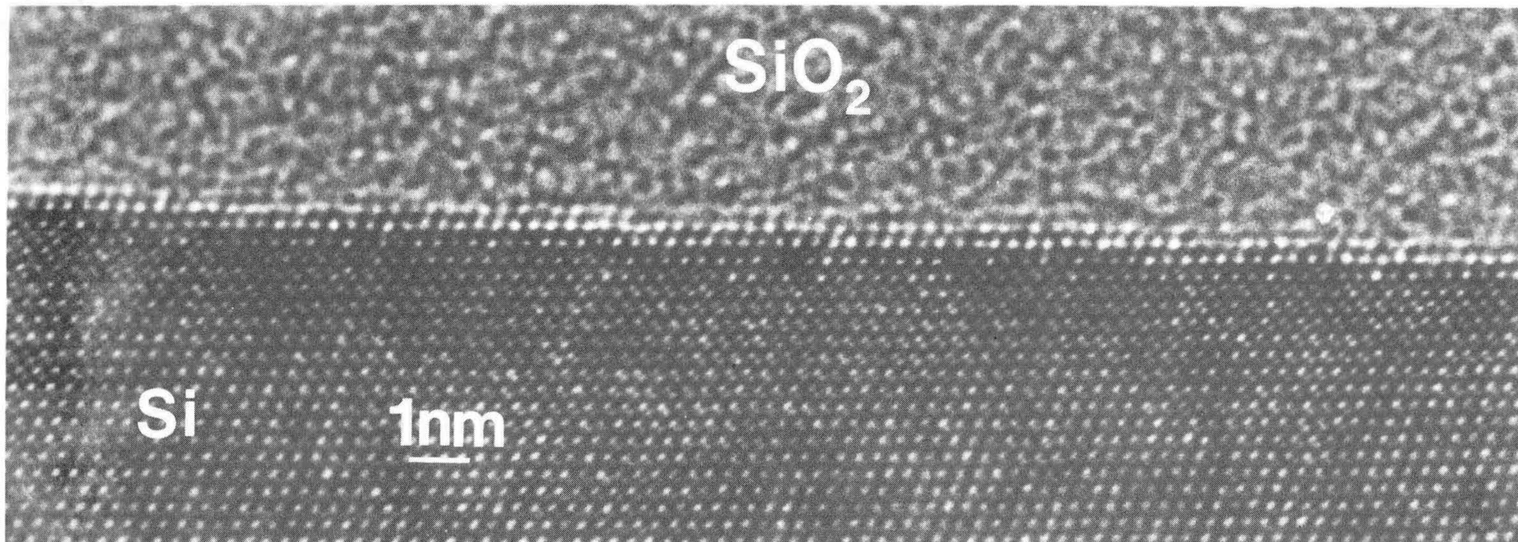


XBB 841-84

Fig. 6.2.2. Higher magnification image of the area in Fig. 6.2.1. Structural ledges and thermodynamical (both positive and negative) ledges on the (111) terraces are clearly resolved.

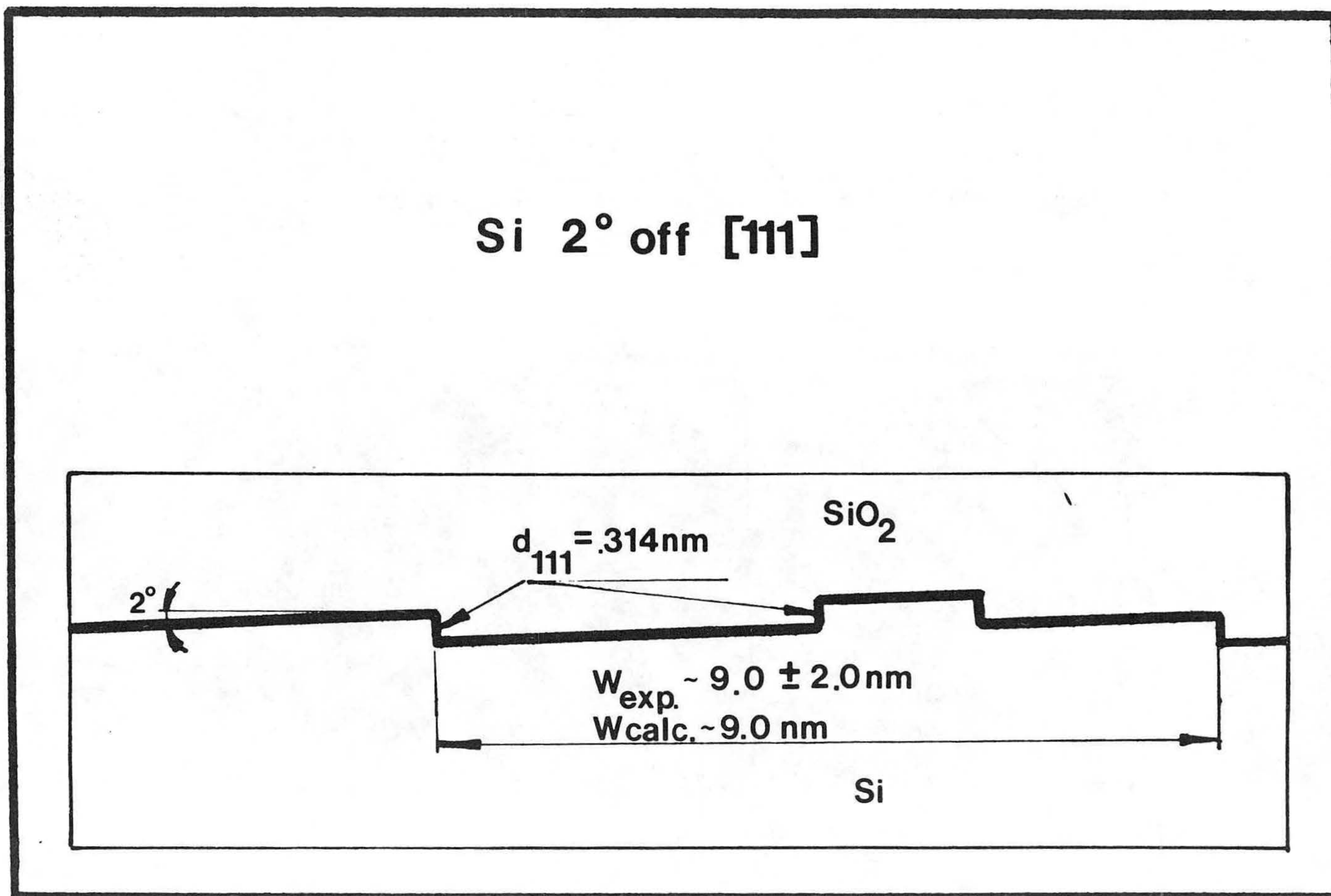


XBL 842-655

Fig. 6.2.3. Schematic representation of the image in Fig. 6.2.2.

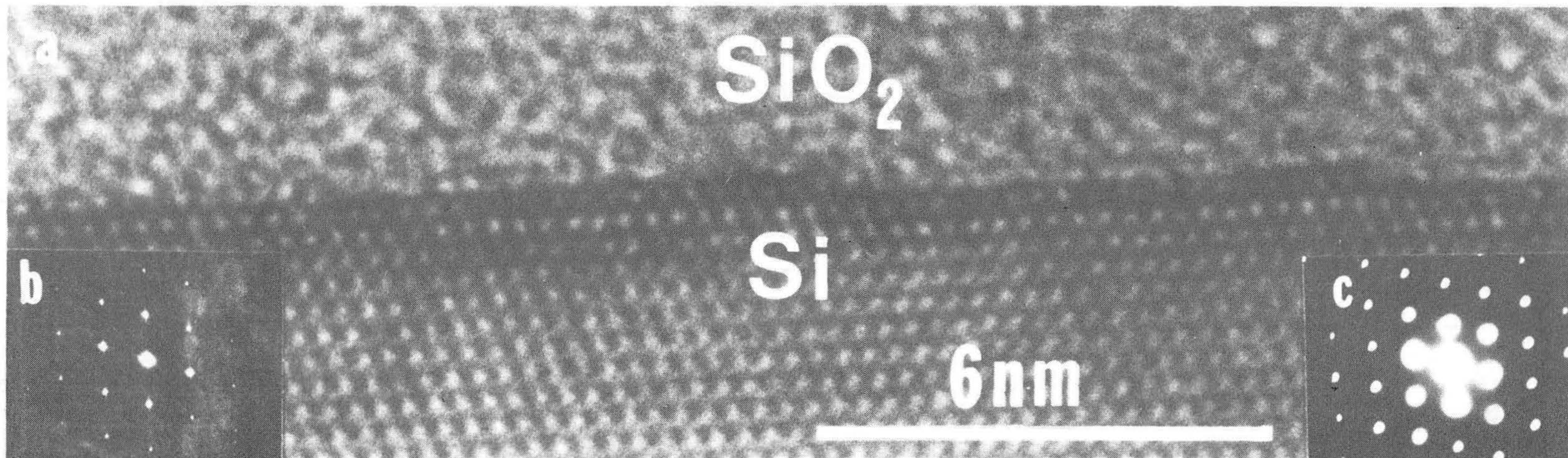


XBB 832-1793C

Fig. 6.3.1. High resolution image of a cross-section of the oxide grown on (111)3°[1$\bar{1}$0] Si in dry $O_2$ at 1000°C. Structural steps are clearly resolved.

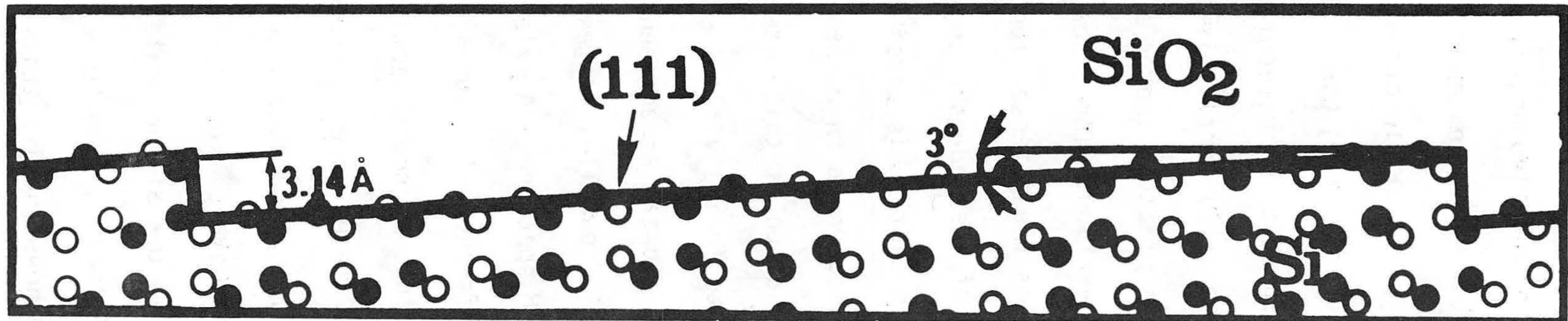


XBB 832-1793B

Fig. 6.3.2. Model of stepped Si surface corresponding to the image in Fig. 6.3.1.

surfaces. Very clearly defined ledges, also observed for other values of defocus, suggest that the ledge extends through the whole TEM specimen thickness along $[10\bar{1}]$ Si direction although, geometrically, ledges should be observed only along the $[11\bar{2}]$ direction for the vicinal $(111)3^{\circ}[1\bar{1}0]$ Si surface. A molecular framework model for greater inclination from a (111) surface is shown in Fig. 6.3.3 and demonstrates the positions of atoms (nodes in the model) forming ledges along the $[11\bar{2}]$ direction. The arrow indicates the $[10\bar{1}]$ direction which is $30^{\circ}$ from the intersection of the (111) terrace with the ledge. A projection of the ledges along the $[10\bar{1}]$ direction shown in Fig. 6.3.4 demonstrates that it is possible to obtain an interface structure similar to that observed in experiments.

The alternative explanation of this interface contrast is that structural ledges needed to form a vicinal surface consist of segments of $\langle 101 \rangle$ ledges forming a zig-zag arrangement on the Si wafer surface. One segment of such a set of parallel ledges could extend through the whole thickness of the TEM specimen. A molecular framework model representing such a case is shown in Fig. 6.3.5.

In addition, observations of cross-sections of native oxides on vicinal $(111)3^{\circ}[1\bar{1}0]$ Si surfaces were performed in order to determine the influence of the initial Si surface structure on the final morphology after high temperature oxidation. The specimen was imaged with the $[10\bar{1}]$ zone axis of the Si substrate parallel to the electron beam. The native oxide formed at room temperature over a period of 29 days was found to be amorphous and its thickness was estimated both by

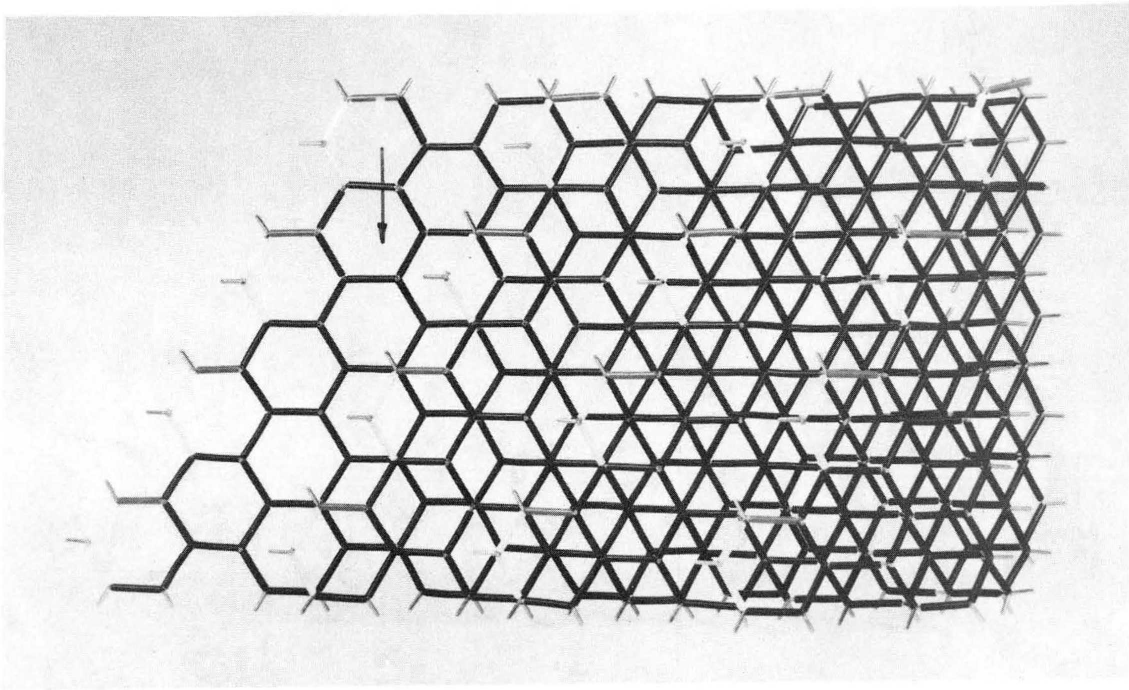

CBB 839-8385

Fig. 6.3.3. Molecular framework model showing ledges along the [11$\bar{2}$] direction. The arrow indicates the [10$\bar{1}$] direction of imaging.

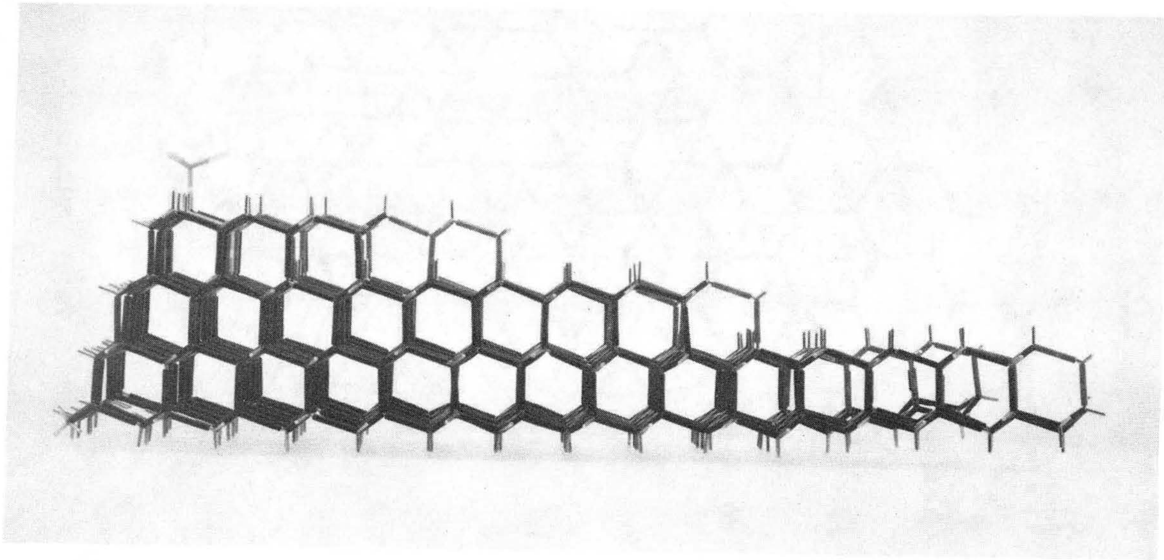

CBB 830-8654

Fig. 6.3.4. The $[10\bar{1}]$ projection of the ledge extending along $[11\bar{2}]$ direction.

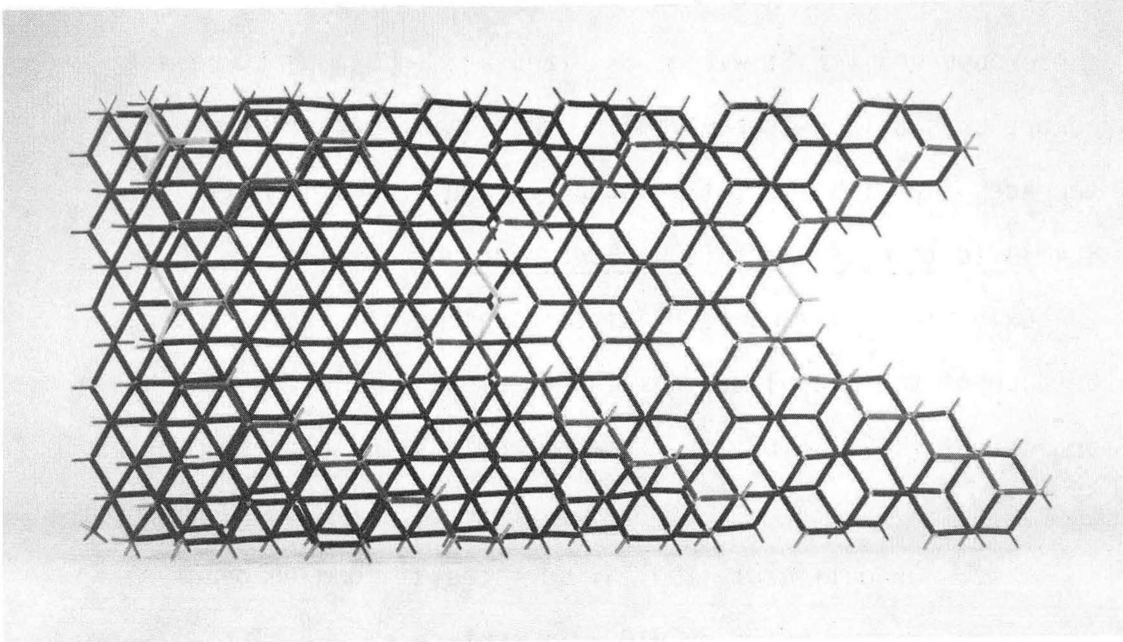

CBB 830-8650

Fig. 6.3.5. Molecular framework model of ledges extending along <101> low energy directions.

ellipsometry and from the HREM image (Fig. 6.3.6) to be equal to 2.0 ± 0.3 nm. The interface morphology was found to be similar to those observed for Si wafers oxidized at high temperature with a very abrupt crystalline-amorphous $SiO_2$ transition occurring at (111) terraces and with one {111} interplanar distance high ledges.

## 6.4 Oxidation of Exact (100) Si Surfaces

Oxidation of exact (100) Si surfaces is of special interest because of their applications in MOS electronic devices in which the quality of the Si-$SiO_2$ interface determines their performance characteristics.

### 6.4.1 Oxidation of (100) Si surfaces at room temperatures: native oxide on (100) Si surfaces.

Prolonged exposure of (100) surfaces to air results in formation of approximately 2.0 nm of oxide as determined by both ellipsometry and direct measurement of the oxide thickness from HREM micrographs (Fig. 6.4.1). The mottled contrast of the oxide corresponds to the amorphous silica. The silicon substrate terminates abruptly at the interface; however, the transition is not as well-defined as in the case of (111) singular and vicinal surfaces. Small undulations are observed along the Si-$SiO_2$ interface with a correlation length of about 1.5-3.5 nm and asperity (amplitude) 0.25 nm. Similar undulations along the imaging direction are expected based on symmetry arguments.

The Si-$SiO_2$ interface resulting from formation of native oxide on the (100)2°[011] Si surface is shown in Fig. 6.4.2. Again the crystalline to amorphous transition region appears to be abrupt on the

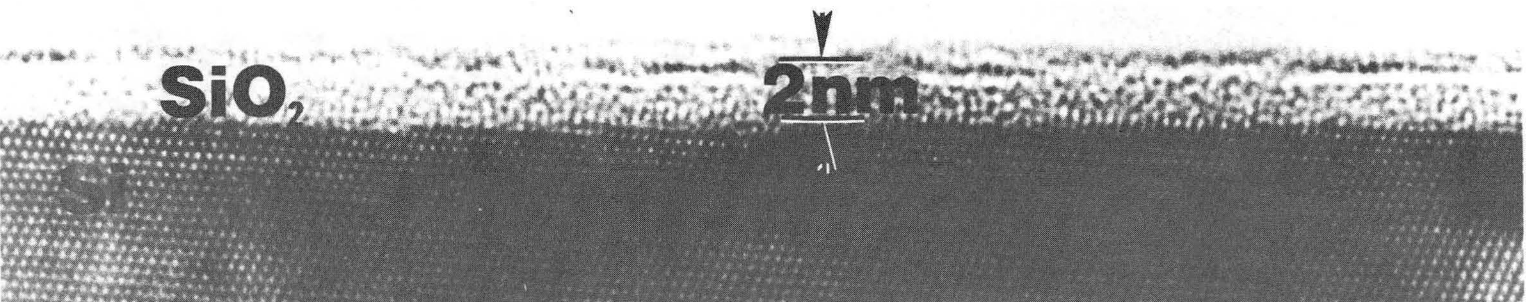


XBB 834-3022

Fig. 6.3.6. Native oxide on (111)3°[$1\bar{1}0$] Si surface.

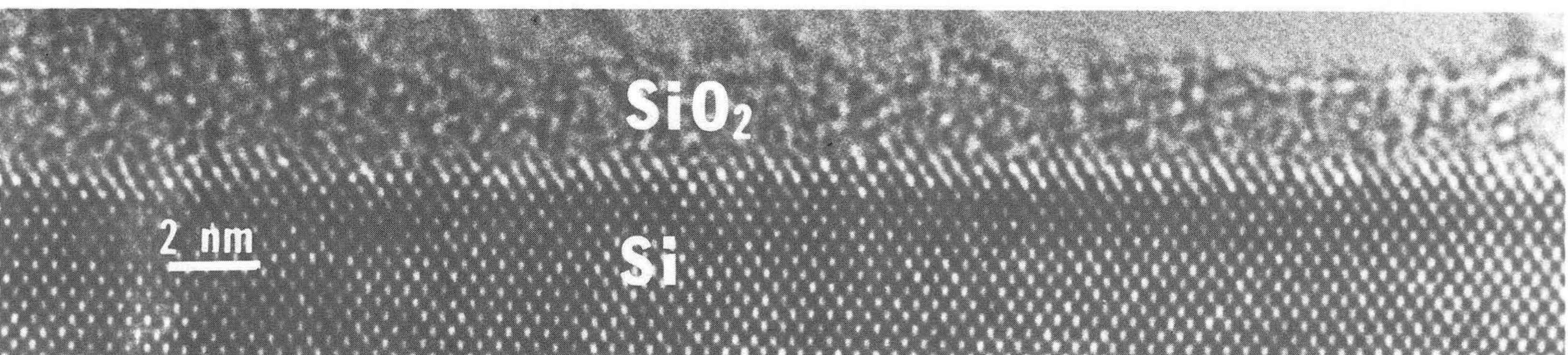


XBB 833-2310

Fig. 6.4.1. Native oxide on {100} Si surface.

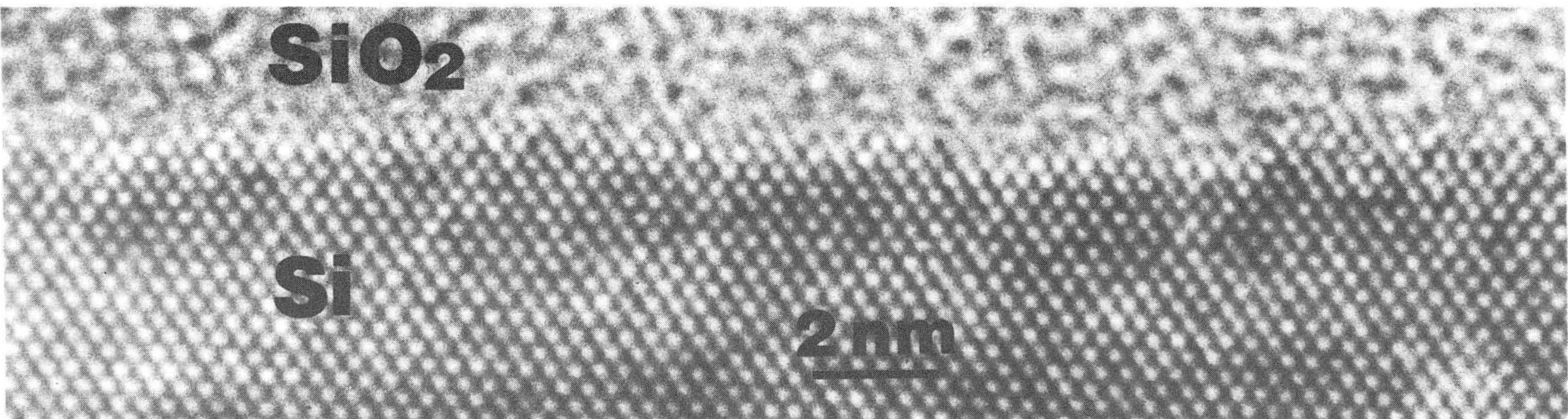


XBB 833-2311

Fig. 6.4.2. Native oxide on (100)2°[011] Si.

atomic scale. The analysis of the uppermost layers at the interface, however, reveals departure from planarity. These departures could be described by (100) terraces separated by steps 1/2 or 1 unit cell ($a_0$ = 0.543 nm) high. However, an alternative interpretation of the contrast exists in both cases, i.e. for exact (100) and (100)2°[011]. The arrangement of fringes might appear also as consisting of small pyramidal protrusions into amorphous $SiO_2$. Figure 6.4.3 illustrates a possible arrangement of atoms on the Si side of the interface which could produce the contrast observed in Fig. 6.4.1 and 6.4.2.

6.4.2 Oxidation of exact (100) Si surfaces.

The structure of the Si-$SiO_2$ interface resulting from oxidation in dry $O_2$ at 1150°C of an exact (100) Si surface is shown in Fig. 6.4.4. The amorphous $SiO_2$ to crystalline Si transition is abrupt and appears from this figure to be accomplished within approximately one 200 lattice spacing (half of the unit cell) and at first sight it could be thought to occur on (200) terraces separated by ledges with {111} facets. Careful analysis of Fig. 6.4.4 indicates, however, that these {111} facets could be traced into the $SiO_2$. Such features would most probably have the shape of a pyramid or of a prism (considering the symmetry of the surface). This is easily seen when one makes observations along {111} fringes and compares this with the apparent interface along the uppermost lattice (200) planes. A computer simulation of the interface structure could make this interpretation more convincing.

The apparent roughness parameters obtained from the analysis of an interface about 1000 nm long are: correlation length L = 2.8 nm and

Fig. 6.4.3. Possible interpretation of the images from Fig. 6.4.1 and Fig. 6.4.2. The Interface morphology might result from the projection of small protrusions along the beam direction.

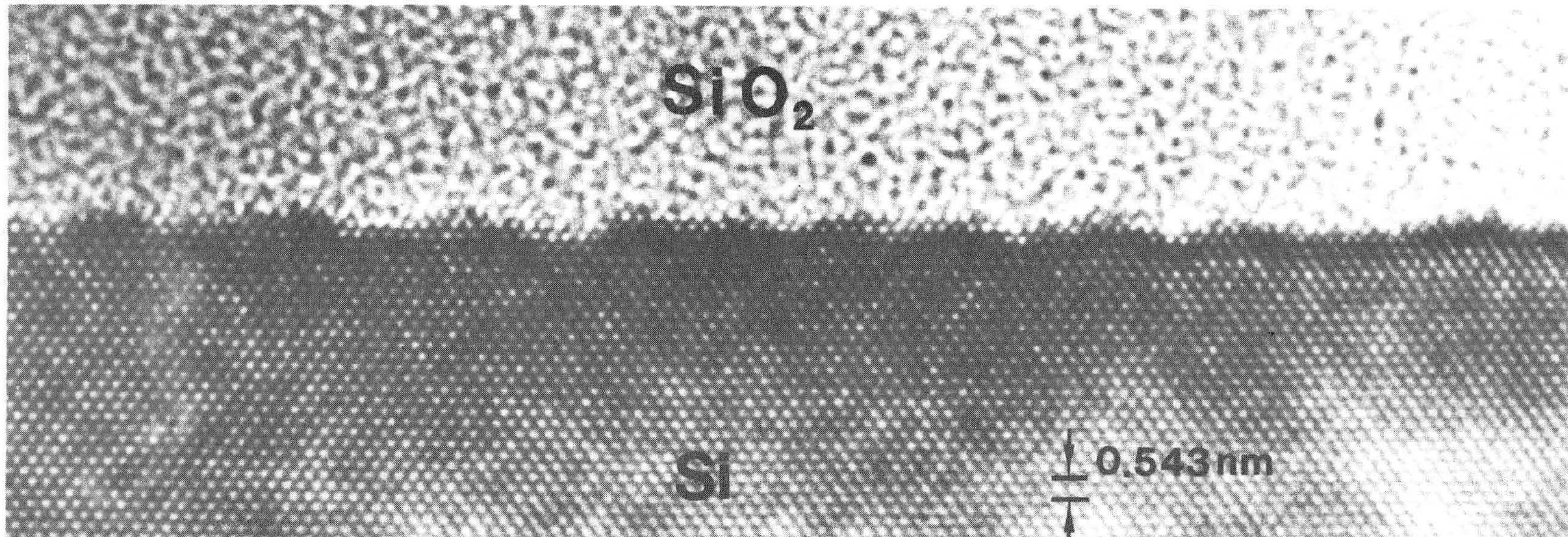


XBB 849-7263

Fig. 6.4.4. High resolution image of a cross-section of silicon oxide film on exact {100} Si surface resulting from oxidation in dry $O_2$ at 1150°C.

asperity $\Delta$ = 0.25 nm, when using the model of the interface consisting of {200} terraces separated by steps up to about one Si unit cell in height. However asperity of the interface should be approximately twice as great for the case of the interface described by the faceted surface.

6.4.3 Oxidation of (100)2°[011] Si surfaces.

The structure of the Si-$SiO_2$ interface obtained as a result of oxidation in dry $O_2$ at 1150°C of the (100)2°[011] surface is shown in Figs. 6.4.5 and 6.4.6. The lower magnification image illustrates that the crystalline Si to amorphous $SiO_2$ transition is abrupt over the entire area of the image. The fragment of the image to the left is from a part of the specimen about 10.0 nm thick and appears to be rougher than the fragment from the thicker part (about 20.0 nm shown at the side of Fig. 6.4.5), and therefore illustrates the effect of projection of the structure along the electron beam direction parallel to the [0$\bar{1}$1] Si direction in the interface plane (see Fig. 5.1). The thinner region is shown in Fig. 6.4.6. The image of the interface could in principle be described by a ledge structure with terrace width about 80 nm and step height equal to half a unit cell. This result accords well with the structure of ledges characteristic of a vicinal surface inclined approximately 2° from exact (100) Si in contact with vacuum, under the assumption that this is a singular surface. Figure 6.4.7 illustrates a possible arrangement of atoms on the Si side of the interface, assuming that the surface is inclined 2° from exact [100] orientation, and steps are 1/4, 1/2, 3/4 and 1 unit

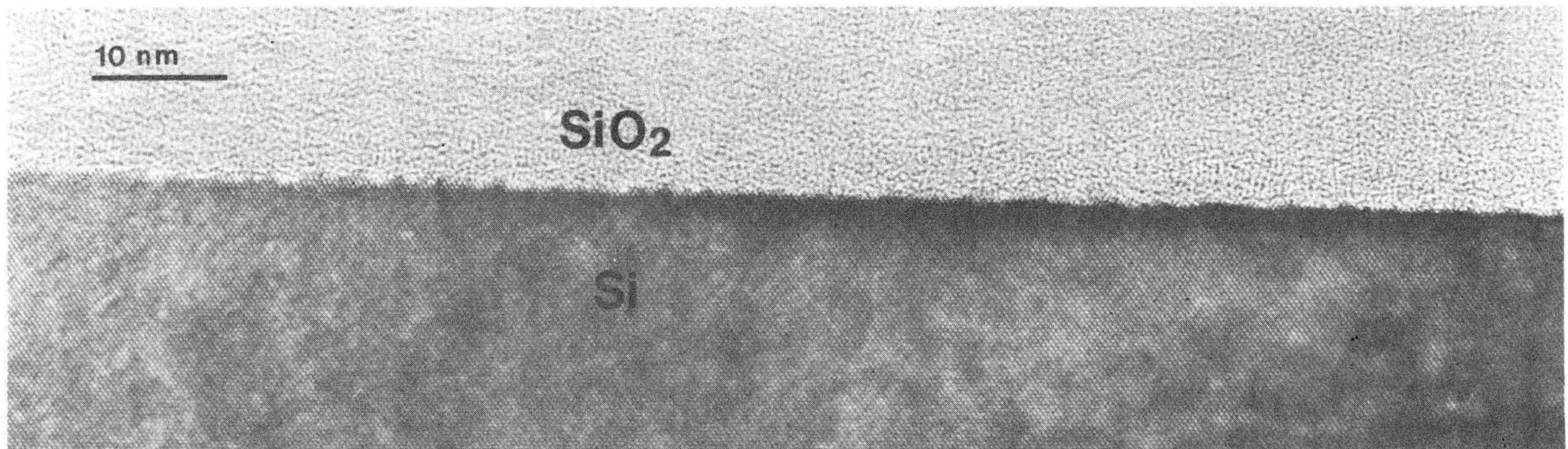


XBB 841-627

Fig. 6.4.5. Low magnification high resolution image of a cross-section of $SiO_2$ film on (100)2°[011] Si substrate (oxidation in dry $O_2$ at 1150°C).

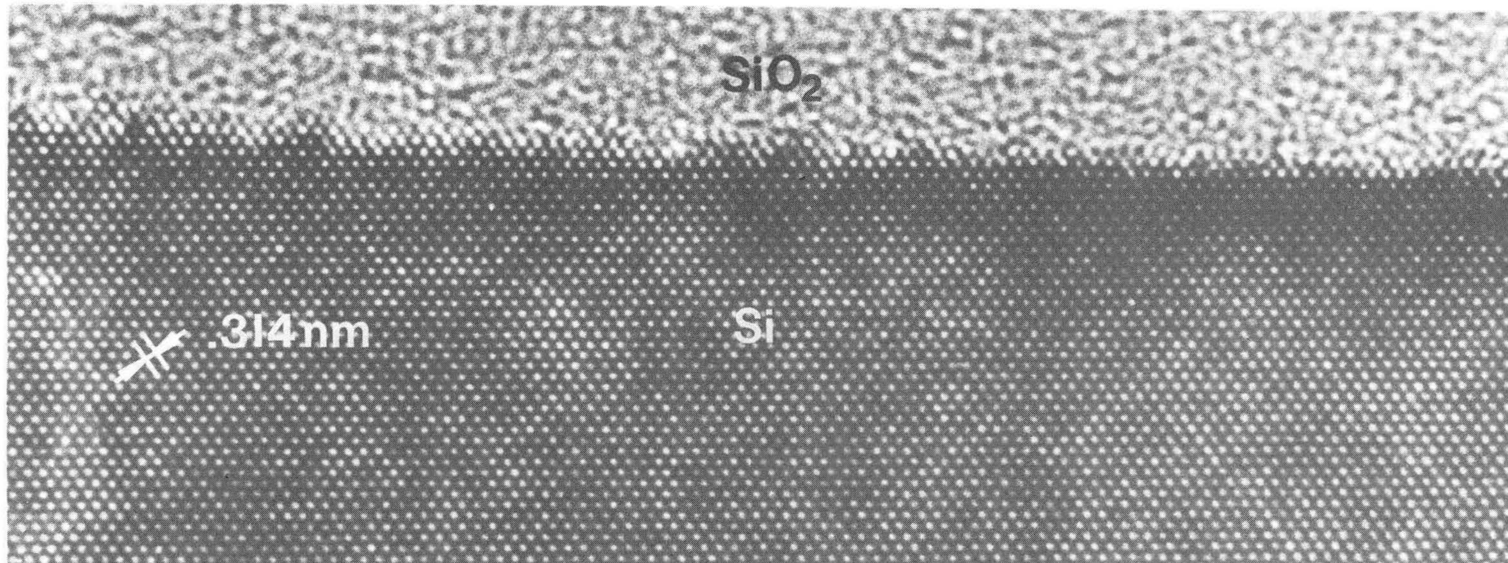


XBB 841-628

Fig. 6.4.6. Higher magnification HREM image of a cross-section of $SiO_2$ film on (100)2°[011] Si substrate.

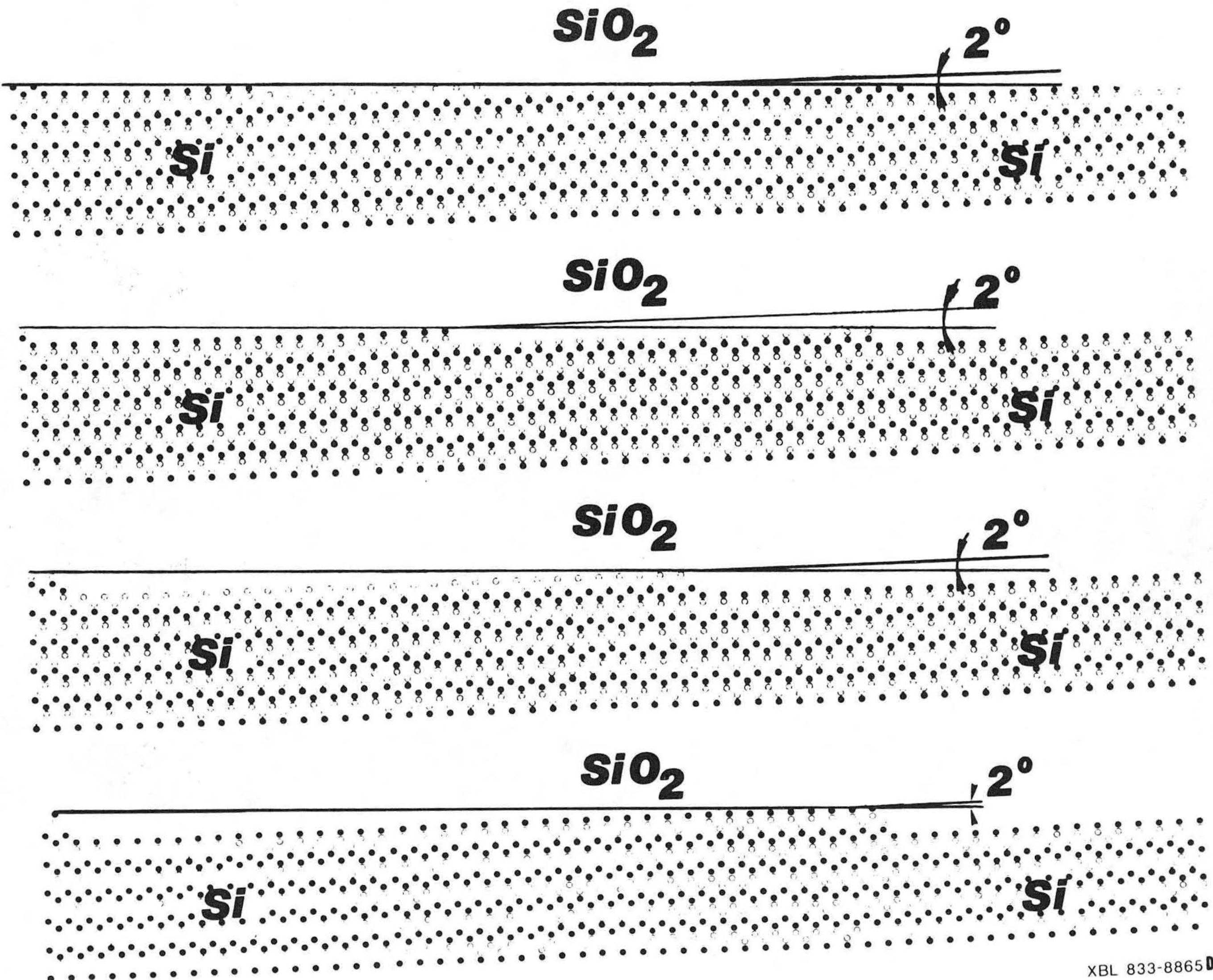


Fig. 6.4.7. Hypothetical (100)2°[011] Si free surface having 1/4, 1/2, 3/4, one unit cell high steps. However such a morphology does not exist with real (100)2°[011] surfaces in contact with the oxide.

cell parameter high. From this figure it is obvious that only steps with integer multiples of 1/2 $a_o = 0.27$ nm can be resolved due to the limitation in the resolution of the microscope ($d_{Sch} = 0.26$ nm). However, the contrast might indicate the existence of small protrusions of crystalline Si into amorphous $SiO_2$ similar to the case of oxides grown on exact {100} Si surfaces.

The resulting surface roughness parameters of the observed interface were similar to those of exact orientation.

6.5 Summary of Experimental Results

The structure of the Si-$SiO_2$ interfaces formed by high temperature (above 960°C) oxidation was studied using high resolution electron microscopy. The information about the interface morphology was inferred from the cross-sectional specimens imaged along the <110> crystallographic direction in the interface plane. This orientation allows imaging of the Si-$SiO_2$ interface and its vicinity at point-to-point resolution about 0.26 nm. At this resolution both {111} and {200} families of crystallographic planes separated by 0.314 nm and 0.272 nm can be easily resolved.

The HREM observations of the structure of the Si-$SiO_2$ interfaces resulting from oxidation (dry $O_2$, p = 1 atm, T > 1000°C) of the lowest surface energy (singular) (111) and vicinal (111)2°[11$\bar{2}$] and (111)3°[1$\bar{1}$0] Si surfaces suggest that:

1) The Si substrate terminates abruptly on atomically flat (111) terraces at the Si-$SiO_2$ interface;
2) Silica is amorphous right up to the interface;

3) Ledges, one interplanar distance high, are observed on both singular and vicinal oxidized surfaces.

The structure of Si-$SiO_2$ interfaces resulting from oxidation (in dry $O_2$ at $p = 1$ atm, $T > 1000^{\circ}C$) of {100} and (100)2°[011] Si surfaces is characterized by greater roughness than in the case of {111} interfaces. This morphology can be interpreted as consisting of small (100) terraces separated by steps up to about one unit cell high, or as an interface consisting of small pyramids protruding into the $SiO_2$. This would indicate that the {100} Si-$SiO_2$ interface is not a low surface-energy (non-singular) interface.

These TEM observations suggest a terrace-ledge-kink model for the interface structure and a ledge mechanism for high temperature oxidation similar to that of evaporation.

## REFERENCES - CHAPTER 6


6.1.1 J. Blanc, C.J. Buiocchi, M.S. Abrahams, W.E. Ham, Appl. Phys. Lett. 30, 120 (1977).

6.1.2 O.L. Krivanek, T.T. Sheng, D.C. Tsui, Phys. Lett. 32, 437 (1978).

6.1.3 O.L. Krivanek, D.C. Tsui, T.T. Sheng, A. Kamgar, in "The Physics of $SiO_2$ and its Interfaces," S.T. Pantelides, Ed., Pergamon Press, New York (1978), p. 356.

6.1.4 J.H. Mazur, O.L. Krivanek. Unpublished results.

6.1.5 O.L. Krivanek, J.H. Mazur, Appl. Phys. Lett. 37, 382 (1980). Some of these results have been presented by one of the authors (O.L.K.) at the Nobel symposium on High Resolution Electron Microscopy, published in Chem. Scripta 14, (1978-1979) and at the Symposium of the Royal Microscopical Society, Cambridge, March 1979, and published in J. Microscopy 119, pt. 1, 88 (1980).

6.1.6 M. Pasemann, O.P. Pchelyakov, J. Cryst. Growth 58, 288 (1982).

6.1.7 J.H. Mazur, in Proceedings of the 41st Annual Meeting of the Electron Microscopy Society of America, G.W. Bailey, Ed., San Francisco Press 1983, p. 107.

6.1.8 J.H. Mazur, R. Gronsky, J. Washburn, in Microscopy of Semiconducting Materials, Inst. Phys. Conf. Series 67, 77 (1983).

6.1.9 J. Mazur, R. Gronsky, J. Washburn, in SPIE Conference Proc. Vol. 463 (1984), p. 88.

6.1.10 J.H. Mazur, J. Washburn, in "The Physics of VLSI," J. Knights, Ed., AIP Conference Proceedings Vol. 122 (1984), p. 52.

6.1.11 S.M. Goodnick, R.G. Gann, J.R. Sites, D.K. Ferry, C.W. Wilmsen, D. Fathy, O.L. Krivanek, J. Vac. Sci. Technol. B.1, 803 (1983).

6.1.12 Z. Liliental, O.L. Krivanek, S.M. Goodnick, C.W. Wilmsen, Mat. Res. Symp. Proc. 37, 193 (1984).

6.1.13 B.Z. Olshanetsky, in "Studies in Surface Science and Catalysis," Vol. 9, M. Laznicka, Ed., Elsevir Scientific Publishing Company, Amsterdam (1982), p. 214.

# 7. THE PROPOSED MODEL OF ATOMIC STRUCTURE OF THE SILICON-SILICON DIOXIDE INTERFACE

## 7.1 Modeling the $SiO_2$ Network Topology Near the Interface

The interpretation of Si-$SiO_2$ interfaces suggested in this study assumes an abrupt transition from crystalline Si to amorphous $SiO_2$. The atoms on the Si side of the interface are on their lattice sites (or only slightly displaced) and are connected directly to [$SiO_4$] tetrahedra. This, together with the assumption of rigid, one-size [$SiO_4$] tetrahedra imposes restrictions on the number of members in the [$SiO_4$] tetrahedra rings of the silica network observable at the interface.

### 7.1.1 Topology of the first monolayer of the $SiO_2$ network near the {111} Si-$SiO_2$ interface.

The attachment of the $SiO_2$ network to a {111} surface is relatively simple irrespective of whether steps are present or not at the interface. Figures 7.1.1 and 7.1.2 show the top and side views of the (111) surface containing ledges one {111} interplanar distance high and extending along <011> directions. The white rods correspond to the Si-O bonds assumed to be the same length as in an [$SiO_4$] tetrahedron i.e. 0.16 nm. Note that the negative and positive sign ledges along this direction are different in nature; the Si atoms at the ledges have one (A type ledge) or two (B type ledge) dangling bonds, corresponding to $Si^{1+}$, $Si^{2+}$ oxidation states respectively. Removal of a single atom at the A type ledge will result in nucleation of a kink pair with the kink atoms in $Si^{2+}$ state. Removal of an Si

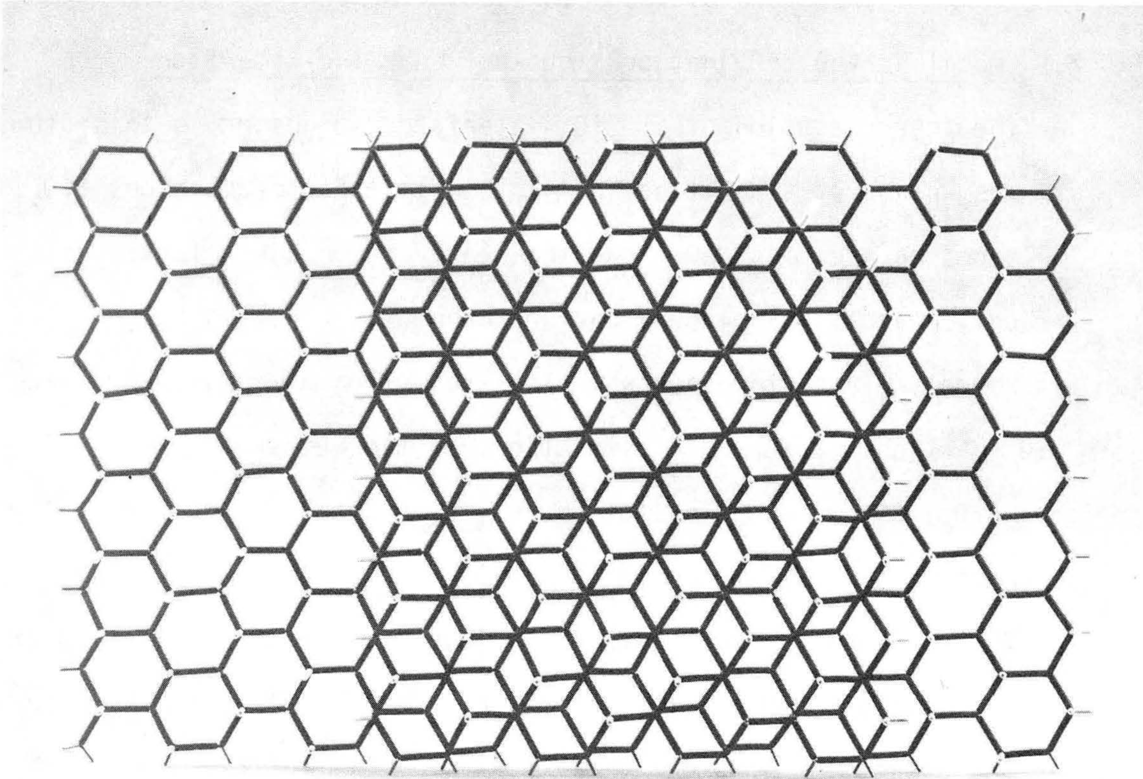

CBB 859-7076

Fig. 7.1.1. Top view of a (111) Si surface with steps along [1$\bar{1}$0] directions. Note the difference between positive and negative ledges.

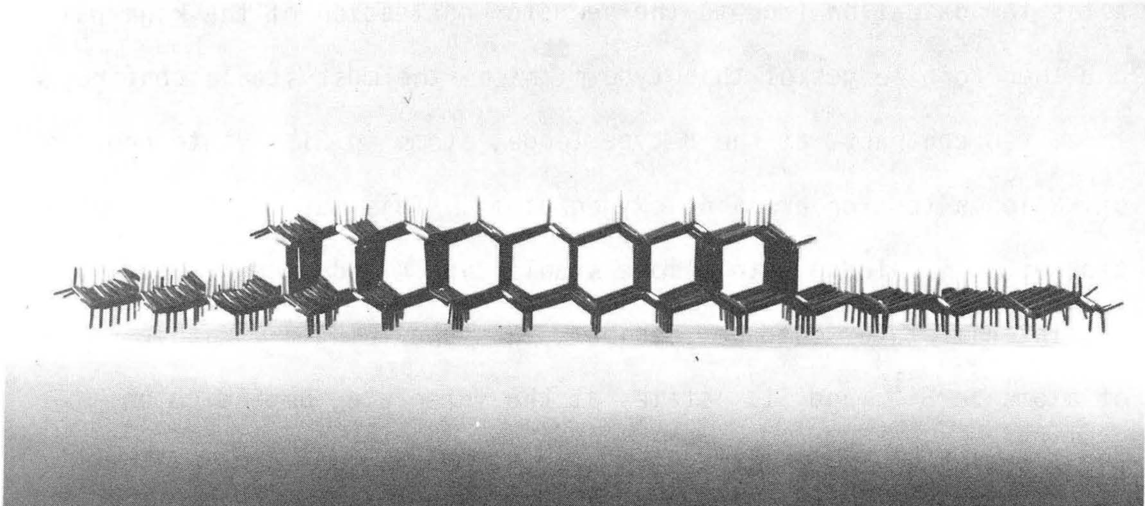

CBB 859-7072

Fig. 7.1.2. Side view of a (111) Si surface with the type A (right) and type B (left) ledges.

atom at a type B ledge would produce a single kink atom in state $Si^{2+}$. On a singular {111} surface, it is expected that type A ledges will be predominant as they would provide a smaller number of sites for oxidation (due to the need for nucleation of the kink pairs) and therefore ledges of this type might be the most stable configuration. In contrast, at the B type ledge, atoms in $Si^{2+}$ state provide oxidation sites for arriving oxygen atoms. This may result in rotation of such a ledge into a more stable type A ledge configuration. Any interim state would be possible, thus providing a variable ratio of atoms in $Si^{1+}$ and $Si^{2+}$ states at the interface, depending on the kinetics of the oxidation process. The topology of the first layer of the $SiO_2$ network is shown from above in Fig. 7.1.3. The model indicates that the first monolayer of $SiO_2$ in intimate contact with the {111} Si surface might contain a large number of 3 membered [$SiO_4$] rings, although 4, 5, 6 and more membered rings could also be present. An interesting observation can be made which relates the number of members in the ring to the steric origin of dangling bonds at the interface. If 3, 4, and 5 membered [$SiO_4$] tetrahedra rings are in intimate contact with the atoms in $Si^{1+}$ oxidation states no dangling bonds are observed. However, 6-membered rings might result in a dangling bond which cannot be connected to the silica network. This is not the case for larger rings than six. In such a situation there is sufficient free volume for only one silica tetrahedron, which could need to be connected to the second monolayer of the $SiO_2$ network. This satisfies the bond. Another interesting observation is

CBB 850-10125

Fig. 7.1.3. Topology of the first monolayer of an $SiO_2$ network in contact with a (111) Si surface containing a step.

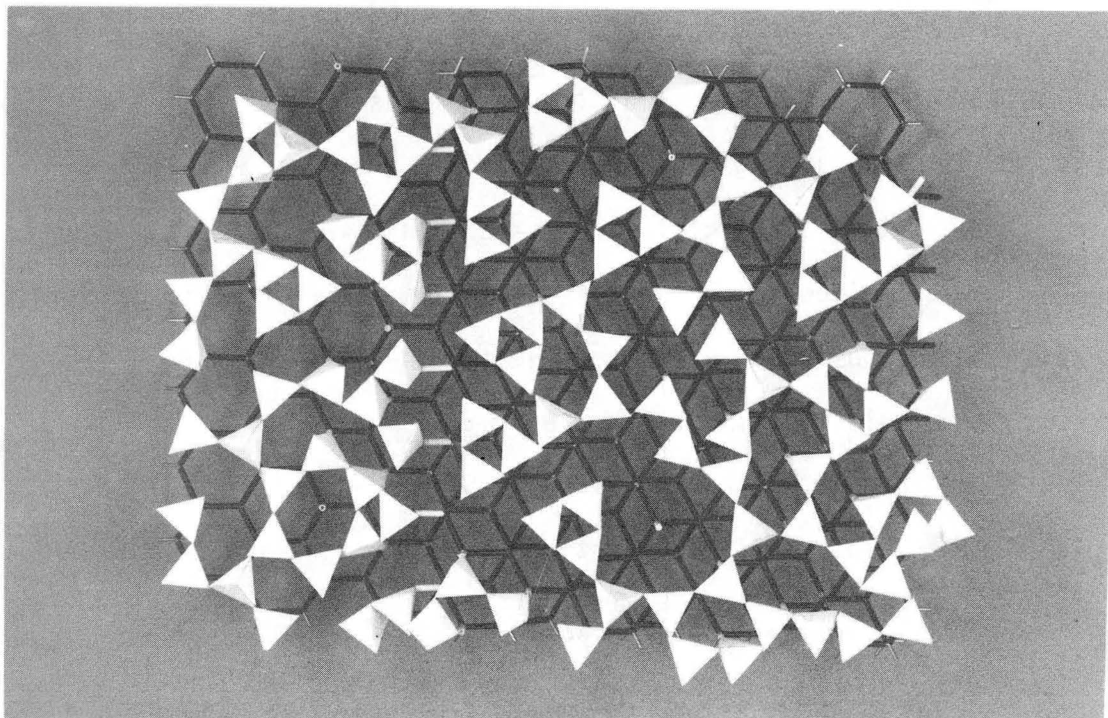

that atoms at the A-type ledge do not have any dangling bonds at the interface. All attempts to form a first monolayer of $SiO_2$ at a B-type ledge created substantial strain and introduced dangling bonds inclined to the interface associated with Si atoms at the B-type ledge. It is assumed here that such ledges are very seldom observable under equilibrium conditions. This is consistent with the EPR conclusions (see Chapter 3.3) reporting observations of $P_b$ centers associated with the dangling bonds at the Si-$SiO_2$ interface. These $P_b$ centers all have axes of symmetry normal to the interface. This is a strong indication that B-type ledges are unlikely.

Figure 7.1.4 shows the side view of the proposed model of the Si-$SiO_2$ interface showing flat (111) terraces connected by the A-type ledge. Such an arrangement of atoms would most probably result in high resolution images of the cross-section like those which have been observed experimentally. Work is currently in progress [7.1.1] which utilizes the positions of atoms as determined from the model for computer simulation of the high resolution image and calculation of the strain energy associated with the Si-$SiO_2$ transition.

### 7.1.2 Topology of the first monolayer of the $SiO_2$ network near the {100} Si-$SiO_2$ interface.

An unreconstructed planar {100} Si surface is terminated by a layer of atoms in the $Si^{2+}$ oxidizing states as shown in Fig. 7.1.5. The estimated value of surface energy for such a planar {100} Si surface was found to be higher than in the case of {111} surfaces [7.1.2]. Therefore non-planar morphologies that could result in lower surface energy should be considered.

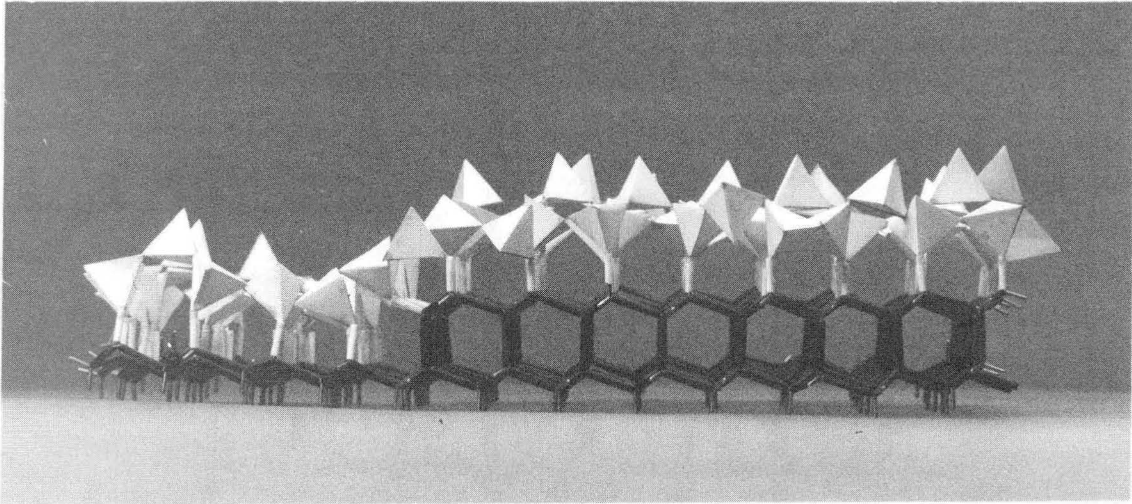

CBB 850-10119

Fig. 7.1.4. Side view of a first layer of an $SiO_2$ network in contact with a (111) Si surface containing a step.

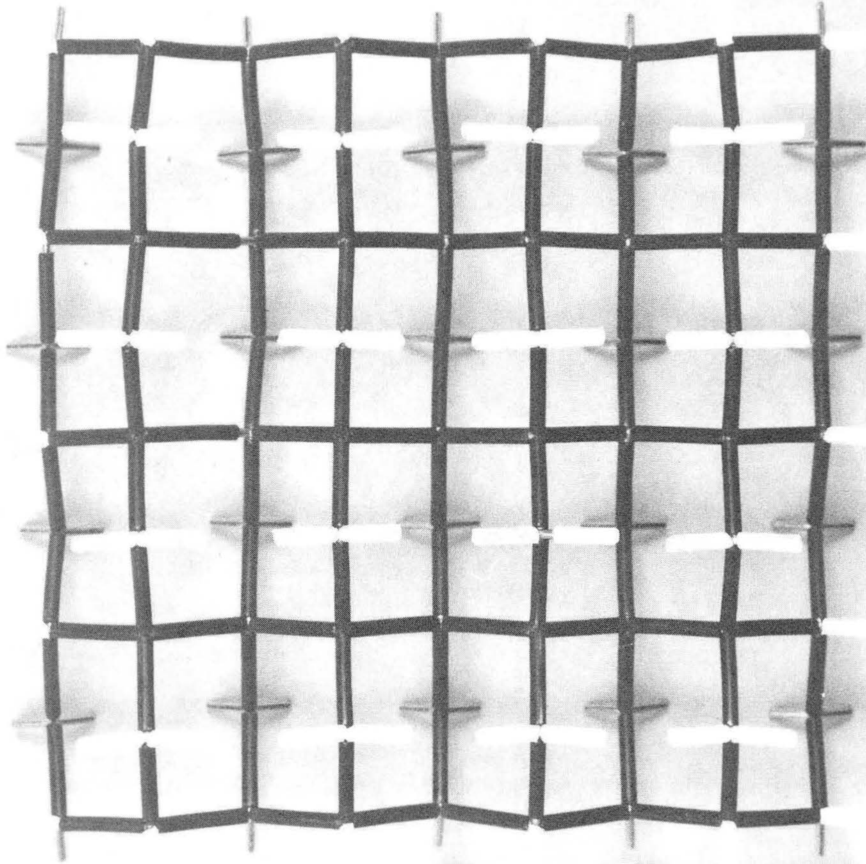

CBB 859-7084

Fig. 7.1.5. a) Model of a flat (100) Si surface. Atoms in the top layer are all in $Si^{2+}$ oxidation states.

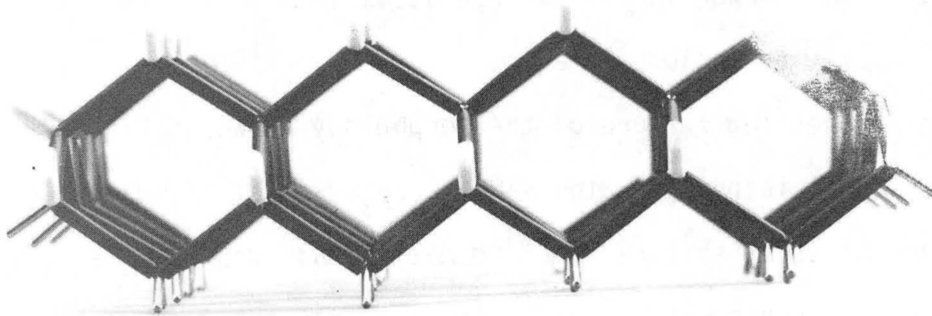

CBB 859-7078

Fig. 7.1.5. b) Side view of the flat (100) Si surface.

Non-planar morphologies have another important property: the total number of broken bonds created in the formation of such a surface is the same as in the planar case. This is demonstrated in Fig. 7.1.6 where the projected area of the surface is the same as that shown in Fig. 7.1.5, and the number of broken bonds is also the same.

In general any change in surface morphology will result in a change in the proportion of surface atoms in $Si^{2+}$ states relative to those in $Si^{1+}$ oxidation states.

An interesting feature of the morphology shown in Figs. 7.1.5, 7.1.6 is that it provides the same arrangement of broken bonds as in the case of (111) surfaces, but normal in this case to the local (111) surface. This property is of particular interest owing to the ease with which one can construct an abrupt interface on a (111) Si surface, as demonstrated earlier.

Figures 7.1.7 and 7.1.8 illustrate a larger model of the (100) Si surface containing small protrusions in the form of pyramids with {111} type facets as observed in Figs. 7.1.5 and 7.1.6. The only atoms which can be in $Si^{2+}$ oxidation states are limited to those which are at the top of the pyramid or those in the valleys between pyramids. The number is much smaller than in the case of a flat (100) plane. This model has been used to investigate the topology of the first monolayer of the $SiO_2$ network in intimate contact with the Si surface. One of the possible arrangements of a first monolayer is shown in Fig. 7.1.9 (top view). This constructed model indicates that it is possible to obtain an interface with the following properties:

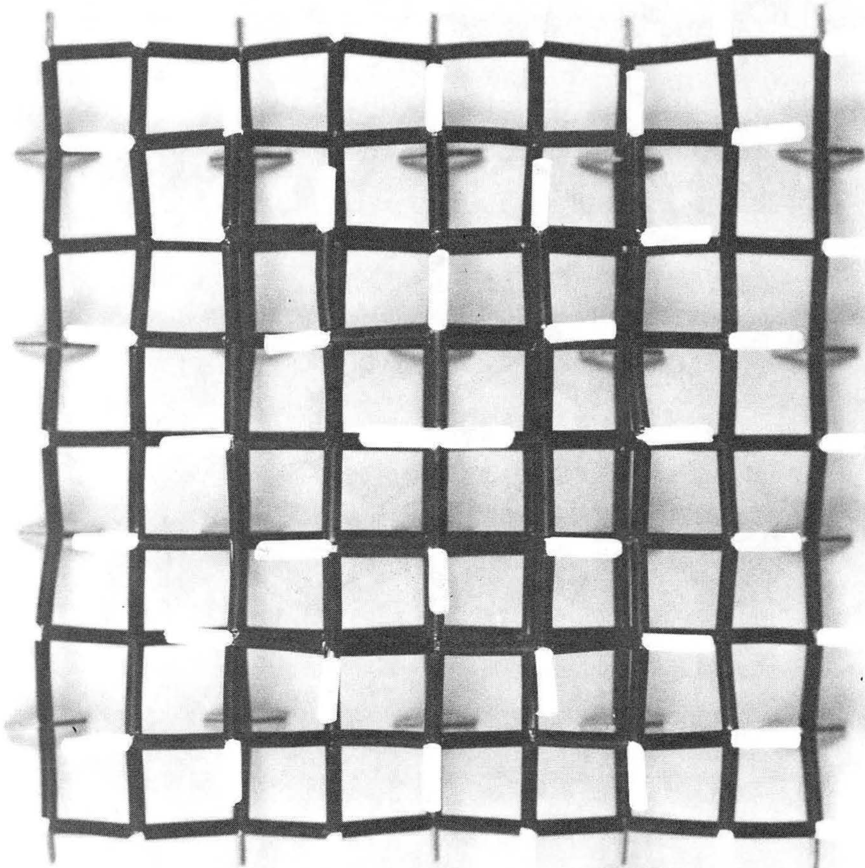

CBB 859-7086

Fig. 7.1.6. a) Model of a fragment of nonplanar (100) Si surface. Note that the number of broken bonds remains the same, however there is only one surface atom in $Si^{2+}$ state. The area of the model is the same as in Fig. 7.1.5a.

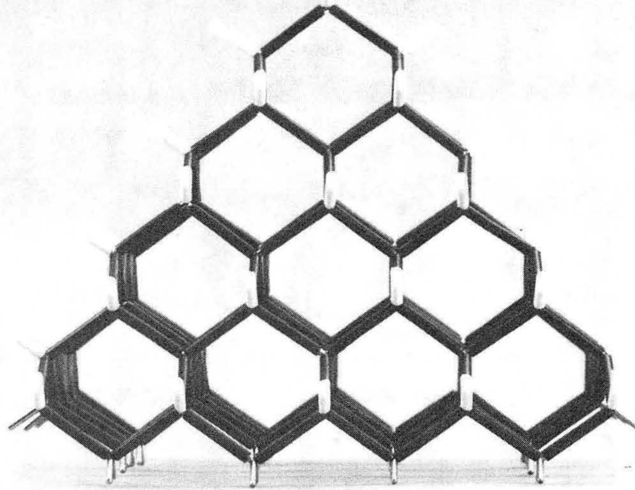

CBB 859-7080

Fig. 7.1.6. b) Side view of the pyramidal protrusion shown in top view in Fig. 7.1.6a. All atoms but one at the top are in $Si^{1+}$ oxidizing states.

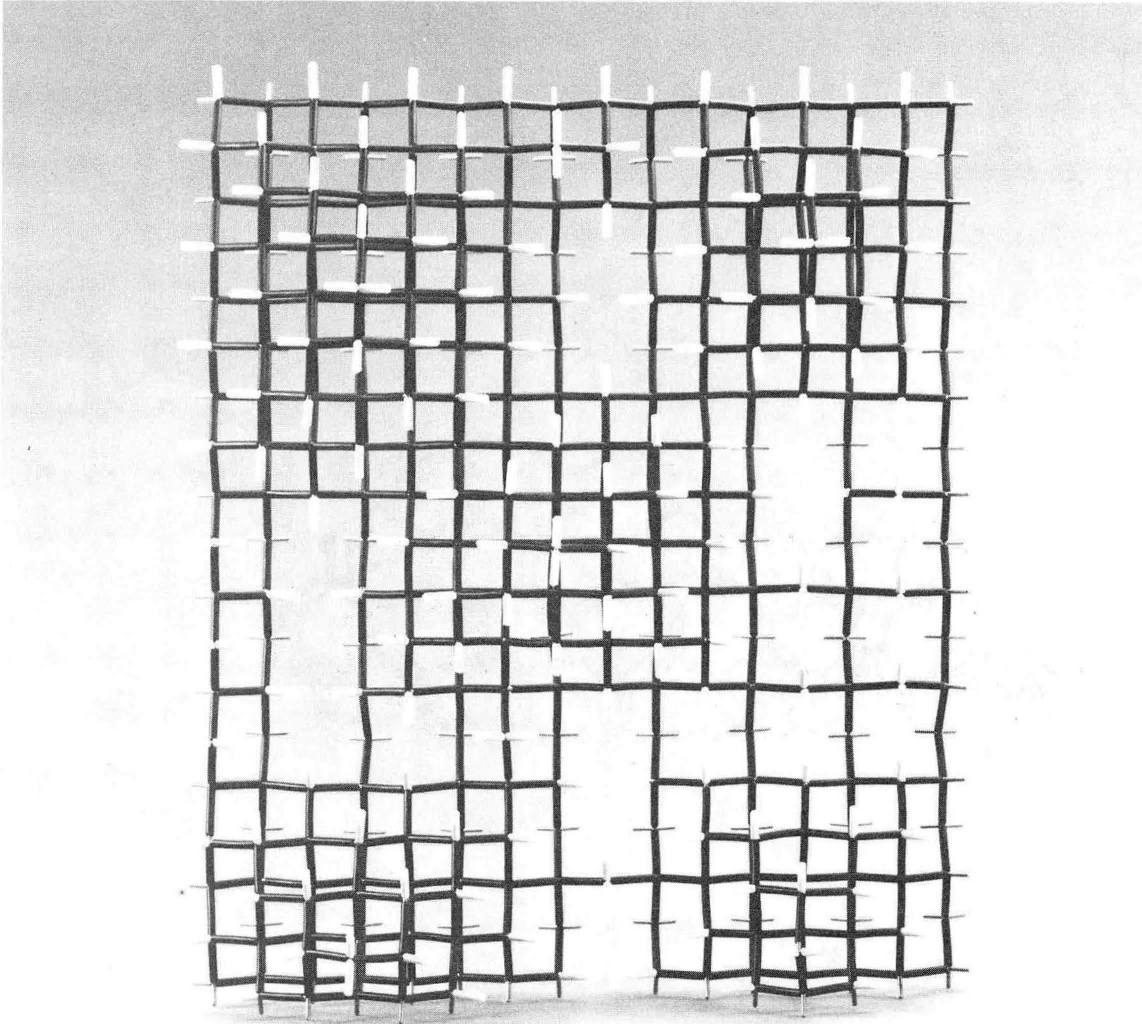

CBB 859-7074

Fig. 7.1.7. Top view of a larger model of the rough (100) Si surface containing small protrusions in the form of pyramids with {111} facets.

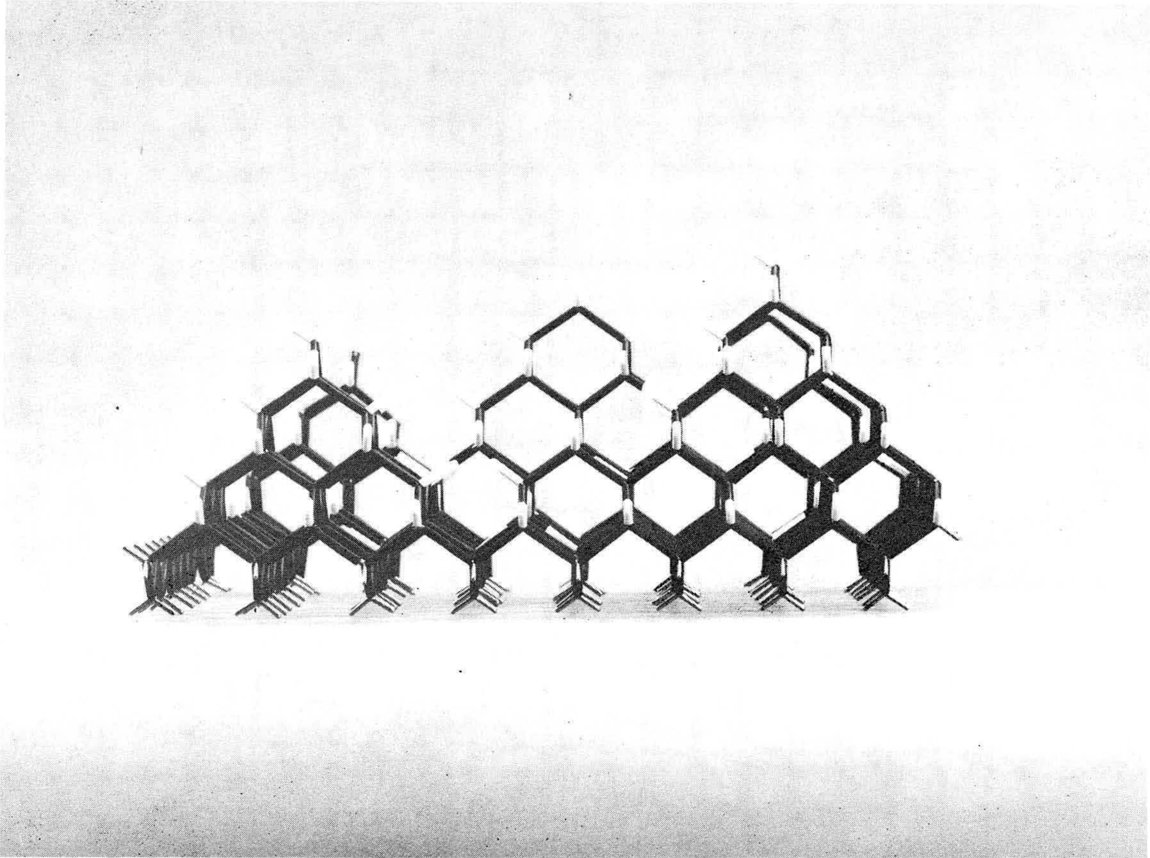

CBB 859-7082

Fig. 7.1.8. Side view of the model shown in Fig. 7.1.7.

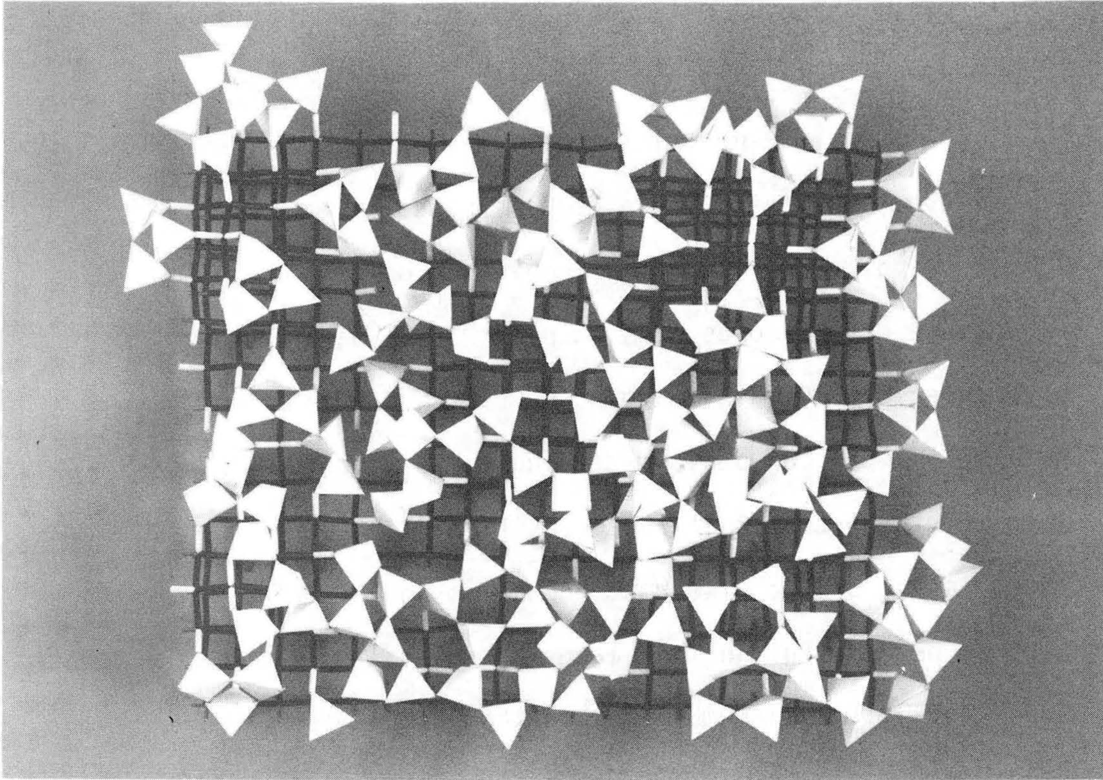

CBB 850-10127

Fig. 7.1.9. First monolayers of $SiO_2$ on a rough (100) Si surface consisting of pyramidal protrusions.

1) The transition from crystalline Si to amorphous $SiO_2$ is abrupt and occurs within one monolayer of $SiO_2$;

2) There is a very small number, if any, of dangling bonds which cannot be satisfied because of steric reasons;

3) These bonds are normal to the local {111} interface, but are, however, inclined to the {100} surface;

4) The topology of the first monolayers of the $SiO_2$ network can be described as consisting of 3, 4, 5, 6 and more membered [$SiO_4$] tetrahedra rings.

5) The network can be formed without considerable strain.

All attempts to construct an abrupt planar interface assuming only a constant length of the Si-O bond, equal to that in [$SiO_4$] tetrahedra, were unsuccessful in that large interfacial strains were created and a substantially high number of dangling bonds was observed, even on a relatively small area. Therefore it is suggested that the morphology of the {100} Si-$SiO_2$ interface is correctly described by the morphology shown in Fig. 7.1.9. A side view of such a model is shown in Fig. 7.1.10. This figure represents a projection of the model along the imaging <110> direction in the Si lattice, thus it resembles the high resolution image. Interestingly enough, this morphology, even with an asperity of 3/2 unit cells in height, produces in projection perfectly flat terraces, separated by ledges half a unit cell high. Such a situation is indeed frequently observed in high resolution images. In addition, some of the lattice planes can still be discerned extending into the [$SiO_4$] tetrahedra layer and they

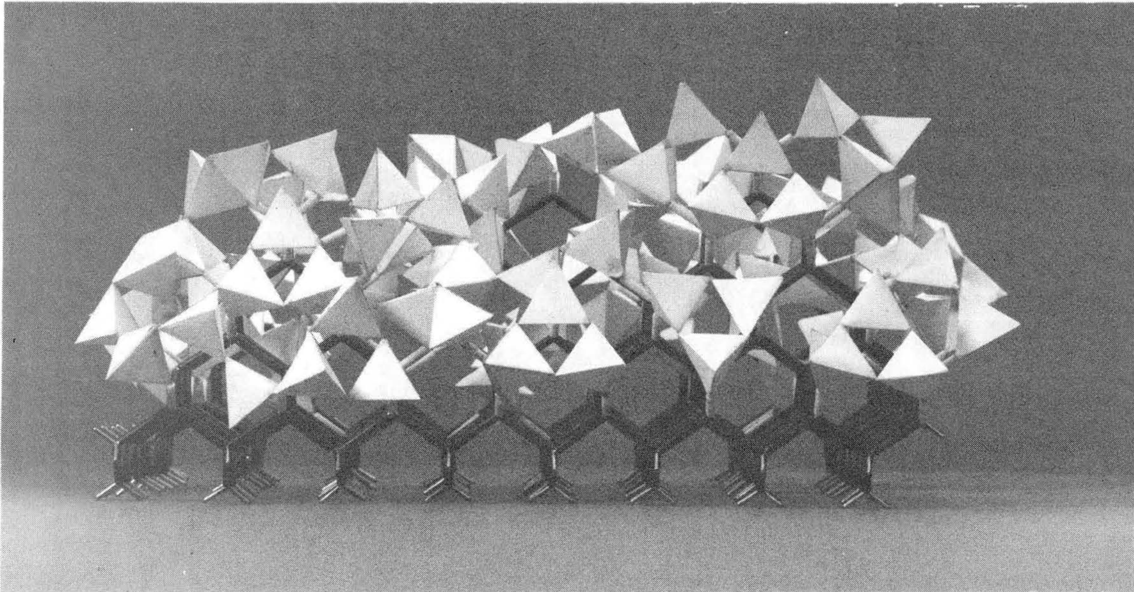

CBB 850-10121

Fig. 7.1.10. a) Side view of the rough (100) Si surface covered with a few monolayers of $SiO_2$. In the projection Si appears to terminate on a flat terrace.

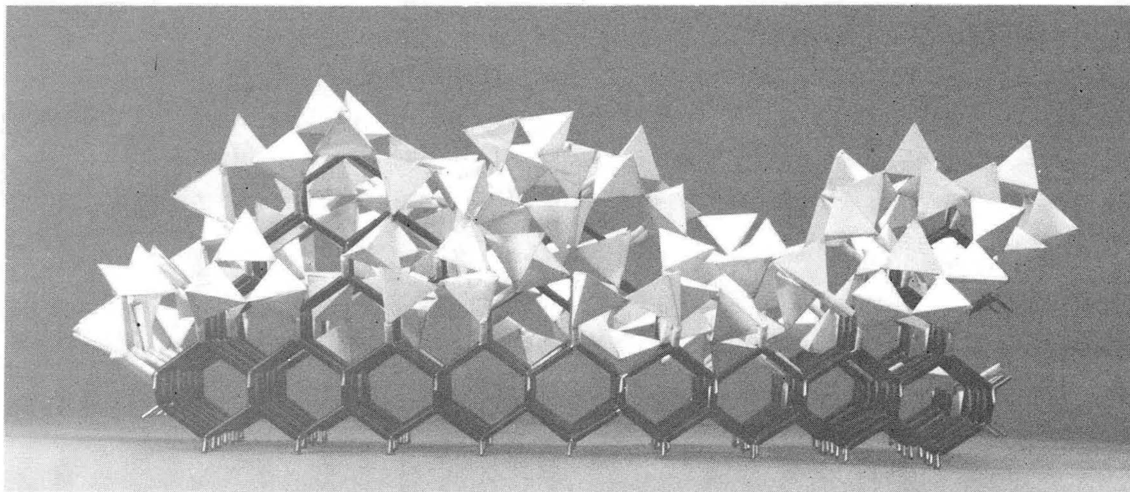

CBB 850-10115

Fig. 7.1.10. b) Different side view of the model shown in Fig. 7.1.9. The projection of an Si lattice extends into the oxide, similar to the situation observed in HREM images.

most probably produce the contrast in the electron micrographs as discussed in Chapter 6.4.

Work is in progress to obtain computer-simulated images in order to strengthen the case for this proposed model.

## 7.2 The Consistency of the Proposed Atomistic Model of the Si-$SiO_2$ Interfaces with Other Experimental Observations

The atomic structure of the Si-$SiO_2$ interface proposed on the basis of relatively straightforward interpretation of high resolution electron microscopy images, combined with three-dimensional models of the Si-$SiO_2$ interface, provides some very interesting insights into its characteristic properties.

The morphology of the interface can be described in terms of the terrace-ledge-kink model. Specifically, the singular (low-energy) and vicinal interfaces could be described in terms of flat (111) terraces separated by structural or thermodynamical ledges, one interplanar distance high. For exact and nearly exact {100} Si-$SiO_2$ interfaces, two models might be plausible. One, the model preferred in this work, can be described by a rough interface consisting of small pyramidal protrusions with (111) facets. The alternative model, with stepped {100} Si-$SiO_2$ interfaces, is considered here less probable owing to the high strain energy associated with flat {100} Si-$SiO_2$ interfaces. In the pyramid model, the pyramids are between 1 and 2 Si unit cells high, while in the ledge model the ledges would be up to one unit cell high. In either case, the transition from the crystalline Si to the amorphous $SiO_2$ network is accomplished locally, within a distance

corresponding to the Si-O bond length (0.16 nm). Macroscopically, the abrupt front might appear to be gradual due to averaging the composition measurements over a region of the interface width with dimensions corresponding to the morphological features [7.1.3]. Thus, the proposed model can be considered to be consistent with other observations, including XPS [7.1.4-7.1.10] and ellipsometry [7.1.3, 7.1.11].

In order to obtain consistency with the interpretation of the interface structure derived from RBS ion-channeling experiments [see Section 3.2] high resolution electron microscopy should provide convergent evidence for very small displacements of atoms, in the order of 0.01 nm. However, evidence for such displacements can only be obtained by matching the experimental images with those obtained using computer simulations. Careful matching of the computer-simulated images with the through-focus-series of electron micrographs is necessary. The model would allow Si atoms on the silicon side of the interface to relax from their bulk position. Alternatively, a new interpretation of the RBS results could be proposed which would incorporate the non-planar models of the $Si-SiO_2$ interface morphology presented here. It is appropriate to mention here that none of the RBS-ion channeling studies so far have incorporated the effects of more complicated interface morphologies in the interpretation of experimental results.

The most exciting implication of the proposed models of the $Si-SiO_2$ interface, is that they require the existence of Si atoms at

the interface in different oxidation states, $Si^{1+}$, $Si^{2+}$, and $Si^{3+}$, for any oxidized surface. The proportions of these different states depend upon the interface morphology. Therefore estimates of the proportions of the $Si^{1+}$, $Si^{2+}$, $Si^{3+}$ states which can be obtained from XPS measurements would provide a means for imposing limitations on the number of possible interface morphologies, provided that the experiments are performed on the same specimens.

The consistency between the results obtained from these two techniques (HREM and XPS) extends even further. The proposed models of the interface suggest the need for 3 membered [$SiO_4$] tetrahedra rings in intimate contact with the terminating Si atoms at the Si-$SiO_2$ interface. The existence of such a topology of the $SiO_2$ network has, in fact, also been inferred from XPS results [7.1.6]. This topology of the network near the interface is different from that of bulk amorphous oxide in which the number N of [$SiO_4$] members in the rings is the same as in different polymorphs of $SiO_2$ (see Table I, Chapter 2), i.e. 4 and more.

Another implication of the proposed models is that some dangling bonds are created at the Si-$SiO_2$ interfaces. The origin of them might be steric or strain related. In the proposed models the dangling bonds are normal to the (111) Si-$SiO_2$ interface. This implication of the model is consistent with the EPR results, which associated $P_{b0}$ EPR centers present at the (111) Si-$SiO_2$ interface with the dangling bonds normal to that interface (see Section 3.3).

REFERENCES - CHAPTER 7

7.1.1 J.H. Mazur, P. Grunthaner, J. Washburn, work in progress.

7.1.2 R.J. Jaccodine, J. Electrochem. Soc. 110, 524 (1963).

7.1.3 J.H. Mazur, R. Gronsky, J. Washburn in "Microscopy of Semiconducting Materials," Inst. Phys. Conf. Series 67, 77 (1983).

7.1.4 F.J. Grunthaner, P.J. Grunthaner, R.P. Vasquez, B.P. Lewis, J. Vac. Science Technol. 16, 1443 (1979).

7.1.5 F.J. Grunthaner, J. Maserjian, in "The Physics of $SiO_2$ and Its Interfaces," S.T. Pantelides, Ed., Pergamon Press, New York, 1978, p. 389.

7.1.6 F.J. Grunthaner, P.J. Grunthaner, R.P. Vasquez, B.F. Lewis, J. Maserjian, A. Madhuker, Phys. Rev. Lett. 43, 1689 (1979).

7.1.7 M.H. Hecht, P.J. Grunthaner, F.J. Grunthaner, to be published in J. Vac. Sci. Technol., paper presented at the International Conference on the Physics of Semiconductors, Aug. 6-10, 1984, San Francisco, CA.

7.1.8 G. Hollinger, F.J. Himpsel, Appl. Phys. Lett. 44, 93 (1984).

7.1.9 T. Hattori, T. Suzuki, Appl. Phys. Lett. 43, 470 (1983).

7.1.10 A. Bianconi, R.S. Bauer, Surface Sci. 8, 318 (1980).

7.1.11 D.E. Aspnes, J.B. Theeten, J. Electrochem. Soc. 127, 1359 (1982).

# 8. CONCLUSIONS AND SUGGESTIONS FOR FUTURE WORK

## 8.1 Conclusions

The purpose of this research was to perform highly detailed analyses of the atomic structure of the silicon-silicon dioxide interface and to establish, from details of the structure, the mechanism of oxidation, which in turn determines the structure, chemistry, and electronic properties of that interface.

The major findings of this study are as follows:

1. The Si-$SiO_2$ interfaces formed as a result of oxidation of singular and vicinal (111) Si surfaces (in dry $O_2$ at temperatures above viscous flow of $SiO_2$) are characterized by:
   a) abrupt termination of the Si substrate on atomically flat (111) terraces at the Si-$SiO_2$ interface;
   b) amorphous $SiO_2$ across the whole thickness of the grown oxide layer; and
   c) ledges one {111} interplanar distance (0.314 nm) high on both singular and vicinal oxidized surfaces.
2. The structure of the Si-$SiO_2$ interface formed as a result of oxidation of exact {100} and vicinal {100} Si surfaces (in dry $O_2$ and at temperatures above 960°C) is characterized by:
   a) an amorphous $SiO_2$ extending up to the Si-$SiO_2$ interface;
   b) a planar Si-$SiO_2$ interface over distances discernable by TEM, although the structure of the interface appears to be rougher than the (111) interfaces, and not as well defined;
   c) a morphology that can be described as a locally abrupt interface consisting of pyramidal protrusions with {111}

facets, or, alternatively, as a surface with {100} terraces separated by ledges, varying in height by multiples of a quarter of an Si unit cell (although only multiples of a half unit cell could be observed in the micrographs).

3. Modeling the (111) and (100) Si-$SiO_2$ interfaces, assuming only i) the abrupt transition for interface morphologies as described earlier, and ii) dimensions of the [$SiO_4$] tetrahedra that are the same as in bulk $SiO_2$, leads to the following conclusions:
   a) The Si substrate-terminating layer contains atoms in different oxidation states ($Si^{1+}$, $Si^{2+}$, and $Si^{3+}$) in proportions that vary with the surface morphology.
   b) The topology of an $SiO_2$ network in intimate contact with a (111) Si substrate consists of 3- and more-membered [$SiO_4$] tetrahedra rings.
   c) The 6-member rings in intimate contact with the Si surface may result in the formation of an Si dangling bond normal to the (111) Si surface.
   d) Two types of <110> ledges have been distinguished in modeling: A-type ledges, with ledge-edge Si atoms in $Si^{1+}$ oxidation states, and B-type ledges, with the ledge-edge Si atoms in $Si^{2+}$ oxidation states. Removal of an atom from an A-type ledge results in the formation of a kink pair containing two atoms in an $Si^{2+}$ oxidation state. Removal of an atom from a B-type ledge, however, does not result in ledge atoms in new oxidation states. Therefore, A-type ledges appear to be a more stable, equilibrium configuration.

e) Attempts to form a first monolayer of the $SiO_2$ network at a B-type ledge without creation of large strains and many dangling bonds inclined to the interface were unsuccessful. However, two (111) terraces connected by an A-type ledge allowed the formation of a first monolayer of $SiO_2$ without large strain and without any dangling bond inclined with respect to terraces or interfaces normal to (111). This observation is consistent with EPR findings of $P_{b0}$ centers (associated with Si dangling bonds) only having symmetry axes normal to the (111) interface.

f) Large strains and many dangling bonds were involved in the formation of a first monolayer of the $SiO_2$ network on a flat (100) Si surface.

g) The model proposed in this thesis, that the (100) Si substrate surface terminates at the interface in pyramidal protrusions about one Si unit cell high with {111} pyramid faces, greatly reduces the strains associated with the Si-crystal-to-amorphous-$SiO_2$ transition. The nature of the transition and the chemical bonding is essentially the same as in the case of singular (111) surfaces. The strain energy of an interface with such a structure might be somewhat smaller than in the case of the (111) interface, owing to the larger steric flexibility in arrangements of [$SiO_4$] tetrahedra at pyramids about one Si unit cell high than at a flat or stepped (111) surface. The model, therefore, implies the

existence of $P_{b0}$-like EPR centers with the symmetry axis along the bond direction normal to local {111} facets of the pyramids. The dangling bonds formed at such a facet might have a different local environment that might result in the formation of $P_{b1}$ EPR centers (as yet not completely understood) with slightly different symmetry than for $P_{b0}$.

h) The model requires the existence of Si atoms in $Si^{1+}$, $Si^{2+}$ and $Si^{3+}$ oxidation states. The proportion of these states depends on the surface morphology. This result supports the interpretation obtained from XPS results. Combining modeling of the interface based on HREM with ratios of Si atoms in different oxidation states determined from XPS should impose further restrictions on the possible choices of atomic structure of the Si-$SiO_2$ interface resulting from oxidation of any Si surface.

j) The model implies that the roughness parameters for the {100} interface would be underestimated when determined from the high-resolution micrograph owing to projection effects. This is in agreement with recent attempts to correlate roughness parameters obtained from HREM and from mobility measurements.

4. Implications for the oxidation mechanism are as follows. The results suggest that oxidation on {111} surfaces occurs layer by layer uniformly over large areas. Oxide growth apparently involves the removal of Si atoms from the surface only at the ledges, probably at kinks. In the case of singular {111} surfaces, formation

of the ledges must require repeated two-dimensional nucleation corresponding to the formation of an oxide island in the next {111} layer of silicon. For vicinal surfaces, structural ledges are already present at the interface, providing sites for oxidation. However, for too low a density of such ledges, two-dimensional nucleation was still observed to take place, resulting in terraces with additional positive and negative ledges. The oxidation on {100} surfaces could be described in exactly the same manner if the Si surface consisted of terraces and ledges. However, in the case of an interface morphology described by pyramids (i.e., no terraces), the oxidation sites will be the atoms in $Si^{2+}$ states at the pyramid vertices and in the valleys between the pyramids. In this case the {100} surface could be considered as a nonsingular (rough) surface, with oxidation sites (at which removal of the Si atoms from the Si surface takes place) always present. A similar process is observed for evaporation or dissolution of atoms from a surface into vapor or solution. Although the Si surface in this case is in contact with solid silica, the interface structure appears to behave as it would in contact with a liquid. This is, perhaps, not surprising, because viscous flow of silica occurs above 960°C, and oxidations in this work were performed above 1000°C. The observed interface structure is consistent with high-temperature oxidation proceeding via a ledge mechanism.

## 8.2 Suggestions for Future Work

Several areas of study have to be continued in order to further our understanding of the atomic structure of the Si-$SiO_2$ interface and utilize that information to predict oxidation kinetics and electronic properties. Some of these areas were already indicated in Chapters 6 and 7.

The most important areas include further detailed analysis of the Si-$SiO_2$ interface structure using higher-resolution microscopes than in the present study. These analyses should be performed on a series of oxidized Si {100}, {110}, and {111} surfaces and their vicinal surfaces. Such a study should include an analysis of the high-resolution contrast at the Si-$SiO_2$ interface by means of computer simulation of the images with different morphologies at the Si-$SiO_2$ boundary. The computer simulation requires the position of the atoms as an input data. The simplest way to obtain positions of the atoms is to determine them from constructed models similar to those demonstrated in Chapter 7. This approach is very promising, as it allows easy determination of the atom position on the amorphous oxide side of the interface. However, in order to more narrowly restrict the number of possible models, additional information about the proportion of $Si^{1+}$:$Si^{2+}$$Si^{3+}$ oxidation states at the Si-$SiO_2$ interface is necessary. (This proportion is a function of the atomic structure of the Si-$SiO_2$ interface, as was shown in Chapter 7.) Such additional information might, at present, be obtained from XPS studies. The XPS studies performed on the same specimens used for high-resolution imaging could

also provide additional information about the sizes of N-membered [$SiO_4$] tetrahedra rings at the Si-$SiO_2$ interface, as compared to the sizes of these rings in the bulk $SiO_2$.

Further information about the local atomic arrangement should be obtained from EPR studies of the Si-$SiO_2$ interface on the same specimens used for HREM and XPS studies, leading to the development of a self-consistent model of the Si-$SiO_2$ interface structure and chemistry.

These models should be used to calculate the oxidation kinetics from first principles.

## ACKNOWLEDGMENTS

I would like to acknowledge a number of people without whose help and support my studies could not have been completed and this thesis could not have been written.

First I would like to thank Professor J. Washburn for his encouragement and for being available at any time of the day and at any time of the week, whenever it was needed. I will cherish the memory of working in his group, his inspiring example, his kind attitude towards people. Like him, I will always expect my students to ask themselves the question: What could be wrong with our experiments and those of others, or with their interpretation Like him, I will encourage them to give their utmost. Thank you again.

I also thank Professor R. Gronsky and Professor D. Hess for their critical review of this thesis and their helpful comments.

Thanks go to Drs. K. Brower, R. Gronsky, P. J. Grunthaner, F. J. Grunthaner, M. Hecht, D. Hess, O. L. Krivanek, Z. Liliental-Weber, A. Madhukar and J. Washburn for stimulating discussions on the different aspects of Si-$SiO_2$ interface structure, chemistry and oxidation mechanism.

This research would not have been possible without the technical assistance of Don Jurica, David Ackland and Adrian Gronsky.

Many thanks go to my friends Carol Varey and Nick Roberts who spent many hours making editorial improvements to the thesis instead of enjoying a well-earned vacation. I think we will remember this Christmas experience for a very long time.

I am indebted to my friend Elke Ender for her invaluable assistance in the construction of the Si-$SiO_2$ interface models.

Thanks are also owed to the Technical Information Division (TID) personnel, in particular Marilyn, Joan, Chuck, Doug, Steve and all the other members of the Photo-Lab, Alice and Belinda from the illustration section of TID, and the team of masters of the processed-word Connie, Jean and Karla, all of whom are acknowledged for beating many impossible deadlines. Thanks to them for their kindness and superb work.

Connie Silva of TID and Joasia Liliental are thanked for their excellent job in the word processing of the thesis.

I thank my parents and my sister for their love, continuous encouragement, inspiration and understanding.

Finally I would like to thank all my friends whose companionship, support and intellectual stimulation made my stay in Berkeley so exciting. I will always remember the good times we have had here. Thanks to all of you, including Allan, Amelia, Anna, Antoni, Anthony, Beth, Bill, Bob, Carl, Carol, Cheng-Fong, Channing, Danielle, David, Don, Duke, Ed, Edwardo, Eicke, Eleonore, Elke, Fred, Graciela, Ginny, George, Maruko, Isydore, Jack, Jan, Jenny, Jesus, Jim, Joanna, Joasie, Jose, Judy, Kannan, Kazu, Lew, Linda, Liz, Lori, Mehmet, Meresi, Mike, Miki, Nancy, Nicole, Ondrej, Peiching, Richard, Roar, Shigeo, Steve, Sule, Uli, Ulla, Yih-Cheng, Tad, Tien-Tien, Tim, Tom, Trudy, Walter, Zuzanna.

This work was supported by the Director, Office of Energy Research, Office of Basic Energy Science, Materials Science Division of the U.S. Department of Energy under Contract No. DE-AC03-76SF00098.

This report was done with support from the Department of Energy. Any conclusions or opinions expressed in this report represent solely those of the author(s) and not necessarily those of The Regents of the University of California, the Lawrence Berkeley Laboratory or the Department of Energy.

Reference to a company or product name does not imply approval or recommendation of the product by the University of California or the U.S. Department of Energy to the exclusion of others that may be suitable.

*LAWRENCE BERKELEY LABORATORY*
*TECHNICAL INFORMATION DEPARTMENT*
*UNIVERSITY OF CALIFORNIA*
*BERKELEY, CALIFORNIA 94720*